Experimental investigation into the evaporating behaviour of pure and nanofluid droplets.

By

John Ross Moffat

Doctor of Philosophy
The University of Edinburgh, 2010

Declaration

The work undertaken in this thesis is the original work of the author, except where specific reference is given to external sources. This work has not been submitted, in part or in whole, for any other degree at any other university.

John Ross Moffat

Acknowledgements

I would like to thank my supervisor Khellil for his time, patience, understanding, and guidance. He has been a constant source of support throughout my studies and I am indebted to him for providing me with this opportunity.

I would like to thank Prof. Omar Matar from Imperial College London who helped with the theoretical treatment of my results. I would also like to thank Prof. Martin Shanahan from Université Bordeaux who was a great source of inspiration and knowledge. I would also like to thank Prof. Annie Steinchen from Marseille Université who provided much of the insight into the theoretical interpretation which is presented in chapter five of this thesis.

Throughout my time at the university there have been many colleagues who have taken time out of their busy schedule to offer their advice, opinions, ideas, and assistance, I would like to thank them all. In particular I'd like to thank bobby Hogg and his technical staff for their time and assistance in constructing my experiments.

I'd like to thank Sam, Dario, Chris, Jovanna, Jacqueline, and Yuan for all their support.

I'd also like to thank my friends and family, all of whom have helped me through my studies. In particular I'd like to thank my mother Margo, and my father Bruce for their encouragement and support all through my studies.

Abstract

In this experimental investigation the evaporative behaviour of liquid droplets of both pure fluids and fluids containing nanoparticles was studied. Initial tests were conducted on drops of pure volatile liquids using IR thermography, and the effect of substrate material, drop composition, and substrate temperature was investigated. The effect of the addition of nanoparticles to the liquid drops was then investigated using a contact angle analyser which could record the drop profile in time. The effects of liquid composition, nano-particle composition, nanoparticles concentration, substrate hydrophobicity, and substrate temperature were all studied.

Results obtained from IR thermography showed that there exists interfacial temperature instabilities in evaporating volatile drops, the appearance of these fluctuations was found to be dependent on the liquid and substrate in question and are self generated temperature gradients resulting from non-uniform evaporation. A stability analysis was conducted and the results give a good agreement with experimental results.

The addition of nanoparticles to a liquid drop was found to alter the evaporative behaviour by enhancing pinning of the drop contact line and preventing the drop radius from shrinking. By manipulating the concentration of the particles suspended in a drop, a stick-slip evaporative process was achieved, leading to rings of particulate material formed upon total evaporation. By varying parameters such as substrate hydrophobicity, nanoparticle concentration, liquid composition, and substrate temperature, many distinct nanoparticle deposit patterns were observed upon total evaporation. It was shown that by varying these parameters, many different patterns could be achieved, and that inside these deposit patterns regular formations such as particulate rings, radial lines, and cellular structures were present.

Contents

List of Publications

Journals

K. Sefiane, A. Steinchen, J.R. Moffat; *"On hydrothermal waves observed during evaporation of sessile droplets"*, Colloids and Surfaces A: Physicochemical and Engineering Aspects, **365**, 1-3, 95-108, 2010

J.R. Moffat, K. Sefiane, Shanahan MER; *"Effect of TiO2 nano-particles on contact line stick-slip behaviour of volatile drops"*, The Journal of Physical Chemistry B, **113**, 8860–8866, 2009

J.R. Moffat, K. Sefiane, Shanahan MER; *"Nanofluid Droplet Evaporation Kinetics and Wetting Dynamics on Flat Substrates"*, Journal of Nano Research, **7**, 75-80, 2009

K. Sefiane, J.R. Moffat, O.K. Matar, R. Craster; *"Self-Excited Hydrothermal Waves IN Evaporating Sessile Drops"*, Applied Physics Letters, **93**, 7, 074103, 2008

Conference

J.R. Moffat, K. Sefiane, Shanahan MER; *"Pinning/De-Pinning of Contact Lines of Nanofluids, Effect of Substrate Hydrophobicity, Particulate Material, and Concentration"*, 11th UK Heat Transfer Conference, 6-8 Sep., Queen Marry University, London, UK, 2009

J.R. Moffat, K. Sefiane, M.E.R Shanahan; *"Dynamics of Nanoparticle Laden Drops and Pattern Formation"*, International Workshop on Bubble and Drop Interfaces, 23-25 September 2009

J.R. Moffat, K. Sefiane, A. Steinchen; *"On Thermal-Capillary Waves Observed At Sessile Evaporating Droplets"*, International Workshop on Bubble and Drop Interfaces, 23-25th September, 2009

J.R. Moffat, K. Sefiane; *"Self-excited hydrothermal waves in evaporating sessile droplets"*, 21st Annual Scottish Fluid Mechanics Meeting, 2008/05/22

J.R. Moffat, K. Sefiane, M.E.R Shanahan; *"Spreading and Evaporation Behaviour of Nanofluids"*, Nano South West European Conference, 2008/11/03-05

J.R. Moffat, K. Sefiane, M.E.R. Shanahan; *"Nanofluid Droplet Evaporation Kinetics and Wetting Dynamics on Flat Substrates"*, 4th International Conference on Diffusion in Solids and Liquids , 2008/07/9-11

K. Sefiane, J.R. Moffat; *"On interfacial Instabilities During The Evaporation Of Sessile Drops"*, 2008

K. Sefiane, J.R. Moffat; *"Evaporatively Driven Thermal Patterns In Volatile Drops"*, Euromech 490 Workshop 'Dynamics And Stability Of Thin Liquid Films and Slender Jets, 2007/09/19-21

K. Sefiane, J.R. Moffat; *"On The Role Of Thermal Instabilities In The Evaporation Of Volatile Sessile Drops"*, 10th UK National Heat Transfer Conference , 2007/09/11

J.R. Moffat, K. Sefiane, O.K. Matar; *"Intefacial Instabilities In Evaporating Drops"*, APS - 60th Annual Meeting of the Divison of Fluid Dynamics , 2007/11/18-20

Books

J.R. Moffat, K. Sefiane, R. Bennacer, Y, Guo; *"Recent Progress on Nanofluids and their Potential Applications, Nanno-Science:Colloidal and Interfacial Aspects, VM Starov (Ed.), CRC Press, Taylor&Francis Group, ISBN: 978-1-4200-6500-8"*, Nanoscience: Colloidal and Interfacial Aspects, VM Starov (Ed.), 2010

List of Figures

Nomenclature

A	droplet surface area, m^2
a	experimental constant
b	experimental constant
C	constant of proportionality
$\overline{C}$	nanoparticle motion velocity, ms^{-1}
CHF	critical heat flux, Wm^{-2}
C_p	specific heat, J kg^{-1} K^{-1}
c	vapour conventration
D	diffusion coefficient
d	particle diameter, nm
G	mass flux, kg m^{-2} s^{-1}
g	acceleration due to gravity, m s^{-2}
h	heat transfer coefficient, W m^{-2} K^{-1}
h(r)	drop height. M
I	rate of diffusion
J	mass flux
k	thermal conductivity, W m^{-1} K^{-1}
l	particle length, nm
m	number of particles per unit volume, m^{-3}
n	shape factor
Nu	Nusselt number, Nu = h d / k
P	Pressure, N m^{-2}
Pe	Peclet number, Pe = G d C_p / k
Pr	Prandtl number, Pr = C_p μ / k
r	particle radius, nm
r_m	mean radius of curvature
Ra	radius of spherical cap drop
Re	Reynolds number, Re = G d / μ
T	temperature, K
t	time, s
u	velocity, m s^{-1}
v	volume concentration
V	volume, m^3

Greek Symbols

α	volume fraction
β	ratio of nanolayer thickness to original particle thickness
γ	surface tension, Nm^{-1}
δ	thickness of ordered liquid nanolayer, nm
θ	contact angle
θ_e	equilibrium contact angle
κ	ratio of observed conductivity to that predicted by theory
λ	nanofluid friction factor
μ	viscosity, kg m^{-1} s^{-1}
ν	volume fraction
Ω	Laminar flow heat transfer correlation.
Π	disjoining pressure, N m^{-2}
ρ	density, Kg m^{-3}
Φ	particle packing volume concentration
σ	shear rate, s^{-1}
Ψ	sphericity

Subscripts

c	particle-nanolayer composition
e	effective
f	nanofluid
HC	Hamilton Crosser model
Jang	Jang *et al.* model
l	base liquid
Max	Maxwell model
p	particle
r	radius
w	moving wall
Yu	Yu *et al.* model

1 Introduction

Droplet evaporation occurs in many wide ranging and diverse situations. Typical areas where understanding the behaviour of drops are important include heat transfer, crystallography, surface science, cosmetics, food processing, agriculture and in electronics. Drops are used in spray cooling systems to help dissipate heat in industrial systems. In crystallography the manipulating drop evaporation can lead to the growth of interesting crystalline materials. The evaporative behaviour of cosmetics, paints, and inks is of great interest where highly uniform films of material are required and optimising the evaporation process to produce uniform films of material is desirable. In agriculture, spreading of pesticides and chemical fertilisers is an important factor affecting the overall success of the crop, knowledge of how droplets behave is needed to accurately design crop spraying systems. Despite the ubiquitous nature of the phenomenon, there are still many unanswered questions and there is still much knowledge to be gained from conducting fundamental research into evaporating drops. As well as investigating the behaviour of evaporating pure liquids, this thesis will investigate the effect of adding nano sized particles pure liquids, with particular interest given to the evaporative behaviour of the colloidal suspensions. The behaviour of nano particulate suspensions, which are often termed nanofluids in scientific literature, has been gaining interest in recent years. It is now possible to develop particles of many materials on the nano-scale. When these particles are suspended in a liquid the effective thermal conductivity has been shown to dramatically increase in comparison to the pure liquid [1]. The anomalous increase in conductivity, along with other interesting features such as apparently delaying the onset of the critical heat flux in boiling [2], and the ability to create and manipulate patterns of materials via evaporation has resulted in an increased focus on nanofluid research.

In this thesis the evaporative behaviour of droplets of various volatile liquids are investigated. The addition of nano-particles to the bulk liquids is tested and the results obtained are analysed. The results obtained are useful to both academic and industrial researchers working in the area of droplet evaporation where the evaporative behaviour of colloidal suspensions is important.

Droplet evaporation has been studied extensively few a decades [3-8]. Despite the seemingly elementary nature of the problem, a drop evaporating on a flat surface is a difficult phenomenon to investigate, and there is much that we have still to learn. The process is complicated by there being three phases in contact which are varying temporally and spatially, with cooling and marangoni (surface tension induced) effects present. There have been many experimental investigations which have been conducted in an attempt to obtain a better physical understanding of the topic [9-18]. Recently, there have been many theoretical models developed in an attempt to explain the observed phenomena [19-24]. There still exists a variety of interesting areas of research, including understanding the internal flow phenomenon, the influence of marangoni effects, the influence of liquid, substrate, and vapour phase and the introduction of colloidal particles to the drop, an area which is of interest in this thesis.

The evaporative effect of colloidal suspensions of particles in small drops was investigated by Deegan et al. [10], who studied the interesting rings of materials left upon total evaporation. It was shown that an interesting phenomenon occurs as a result of the evaporative process which leads to accumulation of particles around the edge of a drop. Other investigations have focussed on the evaporative behaviour of colloidal suspensions with particular attention to the interesting patterns formed [25-32]. Manipulation of this pattern forming property is a desirable quality which has potential in many industrial applications.

The work presented in this thesis focuses on small evaporating drops of both pure liquids and liquids laden with nano-particles. There are two distinct investigative undertakings, the first comprises results obtained from the evaporation of volatile pure droplets and is concerned primarily with the thermal behaviour observed during evaporation. A theoretical interpretation of the observed results is also developed to help explain the interesting results obtained in this section. The second set of experiments investigates droplet liquid-particle suspensions (nanofluids), with a particular focus on studying how the addition of particles affects the evaporative behaviour, as well as investigating the resulting deposit patterns which are formed

upon complete evaporation of the drops. Theoretical interpretations are given for the evaporative behaviour which has been observed.

Chapter one provides an introduction to the thesis, detailing the main focus of the research and discussing the scientific merit of the work which has been undertaken. A brief summary of the various areas where the research may be usefully incorporated is given, and an outline of the format of the thesis is presented.

The second chapter outlines the fundamental theoretical concepts which are most relevant to the experimental work. The concepts of surface tension, evaporation, wetting, and spreading are outlined, together with the most important significant findings which have been published. This chapter provides an introduction into the nature of the problems associated with droplet evaporation, and gives a good general outline which leads on to a more complete review of the current body of scientific knowledge available in this area.

An overview of the current level of knowledge in evaporating drops is given in chapter three. The chapter begins with a review of wetting of drops of primarily pure liquids, with both experimental and theoretical work presented, and then the case of evaporating drops is presented. Next, the topic of nano-particulate suspensions is covered with a review of the current level of experimental and theoretical information which is available. The specific case of particulate droplet suspensions is then covered, and finally a small review of interfacial thermal phenomena in liquids is given which is useful in understanding the results obtained in one specific body of work in this thesis which focuses on pure liquids.

Chapter four details an infra red thermal investigation into evaporating pure drops of methanol, ethanol, and the refrigerant FC-72. The chapter reports on the interesting thermal fluctuations which are present during the evaporative process, with the main findings presented and the main conclusions explained.

The work conducted in chapter five was prepared in conjunction with Prof. Steinchen from Marseille Universite, and consists of a theoretical modelling of the observed

behaviour in chapter four. A stability analysis is provided which gives a good agreement with experimental observations.

Chapter six investigates the behaviour of evaporating nanofluid drops, focussing on various parameters which may affect the evaporative process. Fluid composition, nanoparticle material, concentration, substrate material, substrate temperature and vapour compositions are all manipulated and the observed changes in evaporative process are studied. It is shown that the presence of particles in the drops does significantly alter the evaporative process, with pinning of the contact line observed in many cases; the hydrophobicity of the substrate was also shown to affect the evaporative process. An attempt has been made to account for the observed phenomena mathematically.

In chapter seven the final deposit patterns which result from the evaporation of nanofluid drops are investigated. The various interesting patterns are shown to vary depending on the concentration, composition, and substrate temperature. Manipulation of these parameters can lead to various different patterns upon complete evaporation. Depending on the nature of the drop various patterns and features such as concentric rings, cellular cracking patterns, and spoke like particle concentrations can be seen. The results here are primarily qualitative in nature and provide a basis for further study.

The various chapters and the main conclusions are then outlined in chapter eight, with an overall account of the work and the most important concepts which have been learned presented.

2 Theory

In this section the most important physical aspects relating to the topic of droplet spreading and evaporation are outlined. The concept of wetting and spreading is explained, and a mathematical representation of the drop profile is outlined. The underlying concepts regarding evaporation are then discussed.

2.1 Wettability

2.1.1 Fundamentals of wetting and spreading

Wetting refers to the behaviour of a liquid which is in contact with a solid surface. The fundamental interactions between fluids and solid surfaces are of great interest to the industrial and scientific community, and have been widely investigated. Wetting of solid surfaces is present in numerous areas, such as the chemical industry (paints, inks, crop sprays, etc), food processing (coffee powder, freeze dried foods), cosmetics (make up, hair spray, nail varnish), and many other areas such as in construction and textiles.

2.1.2 Surface tension

Surface tension arises from the cohesive nature of liquid matter. A liquid is a state of matter that exists when the attractive forces of the liquid molecules is larger than the thermal agitation. Molecules at the liquid/vapour interface experience an energy imbalance caused by the much larger attraction of the neighbouring liquid molecules, compared to the gas. This imbalance tends to cause a net inward force which minimises the surface area of the liquid surface. The attraction results from the presence of various intermolecular forces (Van der Waals, hydrogen bonds, electrostatic forces, etc).

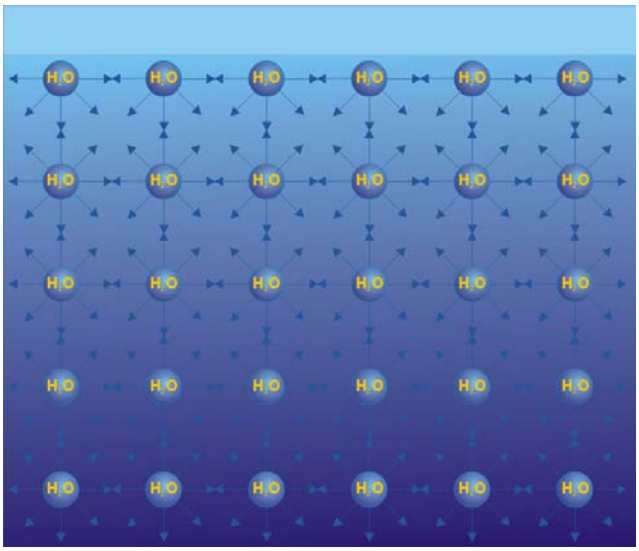

Figure 2. 1. Surface tension arises from attractive forces which act to pull molecules together. At the drop surface the forces pulling on the molecule are unbalanced, leading to a reduction in the surface area of the liquid.

If the underlying cohesion energy per molecule is U inside the liquid, then a molecule at the liquid surface finds itself with an energy deficit of roughly U/2. Surface tension is a direct measurement of this energy shortfall per unit surface area. In mechanical terms the surface tension can de defined as the energy that must be supplied to increase the surface area by one unit:

$$\gamma = \frac{dW}{dA} \tag{2.1}$$

In the above equation the surface tension is expressed in units of J/m^2. As well as the previous description, surface tension can also be expressed as a force per unit length. Surface tension is temperature dependent, and for a narrow temperature range, is seen to decrease linearly with temperature.

$$\gamma_T = \gamma_0 (1 - k_0 T) \tag{2.2}$$

The term k_0 in equation 2.2 is specific to the liquid in question. An important consequence resulting from equation 2.2 is the presence of convective behaviour resulting from local variations in temperature (and thus, surface tension).

2.1.3 Young-Laplace Equation

The pressure difference sustained across two distinct fluid phases and surface tension can be used to obtain the curvature of the surface in question. This relationship is known as the Young-Laplace equation and is given in equation 2.3

$$\Delta P = \frac{2\gamma}{r_m} \tag{2.3}$$

In the above equation ΔP represents the pressure difference between the two fluid phases and r_m represents the mean radius of curvature, this is defined in equation 2.4

$$\frac{1}{r_m} = \frac{1}{2}\left(\frac{1}{r_1} + \frac{1}{r_2}\right) \tag{2.4}$$

In the above equation r_1 and r_2 are the two principle radii of curvature.

2.1.4 Static wetting

Liquids behave differently on different substrates, for instance water resting on a flat sheet of wax paper will form a small droplet, whilst the same droplet placed on smooth glass will spread completely. There are thus different spreading regimes which can be characterised; the extreme cases are total wetting and non wetting. The spreading parameter, which measures the surface energy difference between dry and wet surfaces, can be used to characterise wetting behaviour, this is given in equation 2.5.

$$S = \gamma_{SG} - (\gamma_{SL} + \gamma_{LG}) \quad \textbf{(2.5)}$$

The terms in the equation above represent the surface tensions, γ, at the solid/vapour, solid/liquid, and vapour/liquid interfaces, respectively. The spreading parameter can then be used to give an indication of how much a drop of a particular material will spread on a given surface.

2.1.5 Total Wetting

This occurs when the surface energy per unit area of the dry substrate is greater than that of the wetted substrate. Therefore the liquid will spread as the combination of solid-liquid and liquid vapour surface tension is not enough to overcome the solid-vapour surface tension. Liquids with typically low surface tensions such as acetone and ethanol tend to spread in this way, resulting in a thin film of liquid, this is depicted on the far left of the diagram in Figure 2.2.

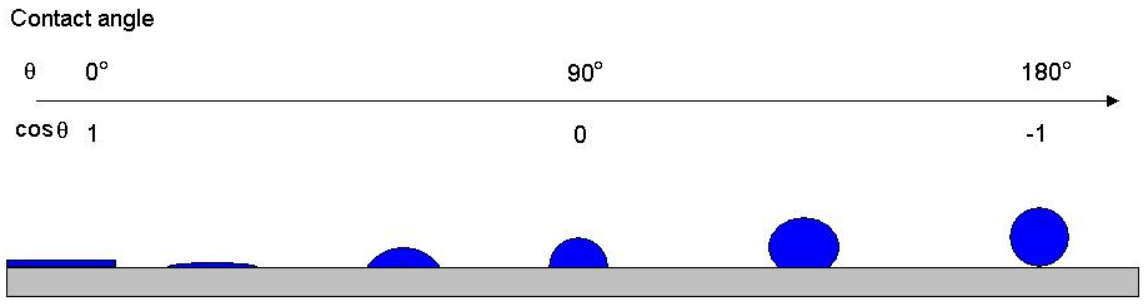

Figure 2. 2. Depending on the drop, surface, and surrounding vapour phase, various spreading regimes can be observed.

2.1.6 Non-wetting

The other extreme occurs when the fluid interactions are more dominant than the fluid-solid interactions. In this instance the liquid molecules pack together, with as little liquid in contact with the solid surface as possible. The resultant drop forms a bead shape as shown on the far right of Figure 2.2. Mercury is a liquid material that

typically behaves in this manner and it can also be observed in water drops resting on hydrophobic surfaces such the lotus leaf, as is shown in Figure 2.3. Surfaces which reduce the wetting of a liquid on a surface are useful in many applications, such as in non stick cooking utensils, or in the construction of materials to help reduce drag, etc.

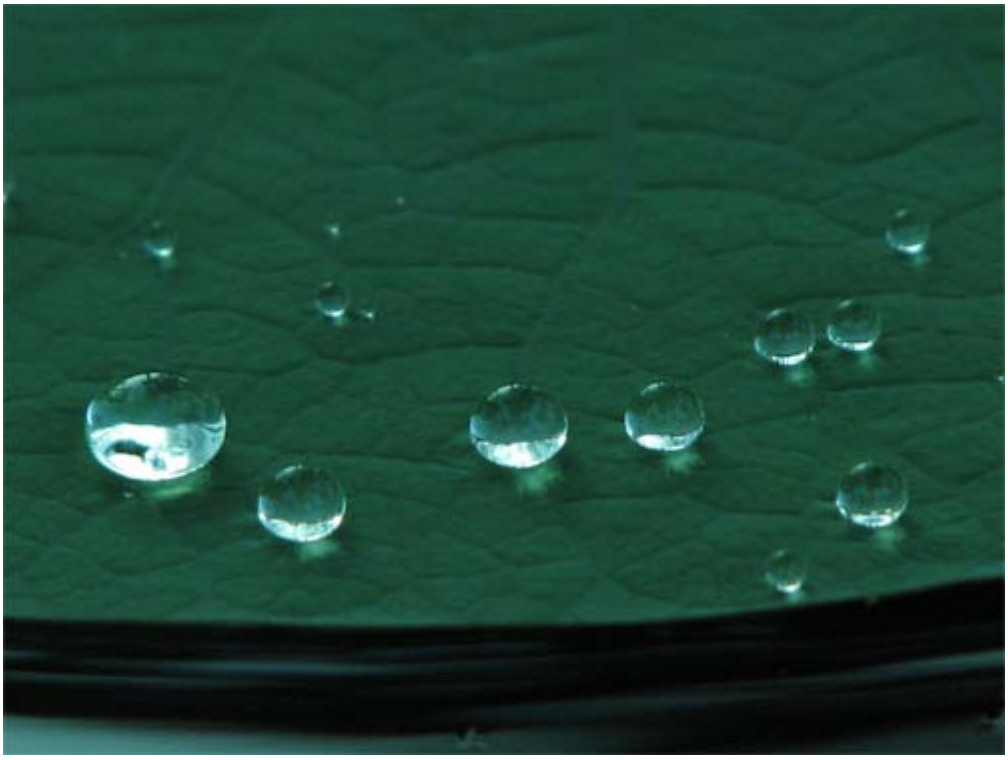

Figure 2. 3. Droplets beading on a lotus leaf, which exhibits hydrophobic properties.

2.1.7 Partial Wetting

When the surface energy per unit area of the dry substrate is less than that of the wetted substrate the liquid will not completely spread. The liquid will form an intermediate drop shape which will have a characteristic non-zero contact angle at the drop periphery (the contact line), this is represented by the intermediate cases shown in Figure 2.2. In the case of partial wetting, the wetted portion of the surface meets the dry surface at what is known as the contact line, and a non-zero contact angle exists at the periphery of the liquid.

2.1.8 Equilibrium Contact Angle

For a partially wetting droplet, when all parameters are held in equilibrium, there exists a contact angle between the liquid and solid surface that is characteristic of the liquid, substrate, and surrounding atmosphere. When this contact angle θ, is < π/2 then the drop is said to be mostly 'wetting', for θ > π /2 the drop is termed mostly 'non-wetting'. If the droplet is small enough, distortion due to gravity can be neglected, and the drop shape can be assumed to be that of a spherical cap. The corresponding equilibrium contact angle, θ_e is described by the Young equation [33], which is presented in equation 2.6..

$$\gamma_{SG} = \gamma_{SL} + \gamma_{LG} \cos\theta_e \qquad \textbf{(2.6)}$$

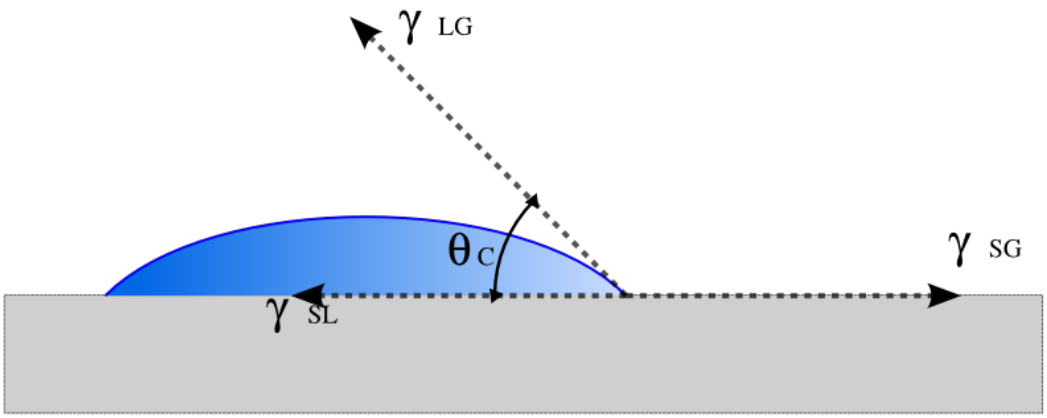

Figure 2. 4. Pictorial representation of the young equation. The shape of a drop resting on a flat surface can be determined from the three distinct surface tension parameters, and the equilibrium contact angle.

This equation, which is visualised pictorially in figure 2.4, assumes the system is in thermodynamic equilibrium, the solid surface is ideally smooth and the system is free from contaminations. Effectively, the Young equation is a force balance where the surface tensions, γ (solid-liquid, solid-vapour, and liquid-vapour) sum to zero at the 3-phase contact line. The young equation can also be derived from a thermodynamic perspective.

$$\Delta G = \Delta A(\gamma_{SL} + \gamma_{SG}) + \Delta A \gamma_{LV} \cos(\theta - \Delta\theta) \quad \textbf{(2.7)}$$

The surface free energy, ΔG, is seen to vary with a small displacement of the wetted area, ΔA. At equilibrium:

$$\lim_{\Delta A \to 0} \frac{\Delta G}{\Delta A} = 0 \quad \textbf{(2.8)}$$

Treating Δθ/ΔA as a second order differential, we can obtain the young equation.

2.1.9 The Contact Line

The contact line exists at the boundary between the solid, the liquid and the surrounding vapour. It is therefore essentially a 3-phase system, with complex dynamical behaviour. The contact line is affected by the interfacial energies of the three phases, dissipation and hydrodynamic liquid interior flows, and geometrical and chemical surface irregularities [3]. Understanding what is happening at the contact line is of paramount importance in heat transfer and wettability investigations; this is because evaporation is enhanced at the contact line [10]. Picknett and Bexon [7] investigated the evaporation of small sessile organic drops and found that there were different modes of drop evaporation, in the first mode the contact angle at the contact line would decrease and the drop base diameter would remain pinned as evaporation proceeded, in the second mode the contact angle would remain the constant, whilst the drop base would recede.

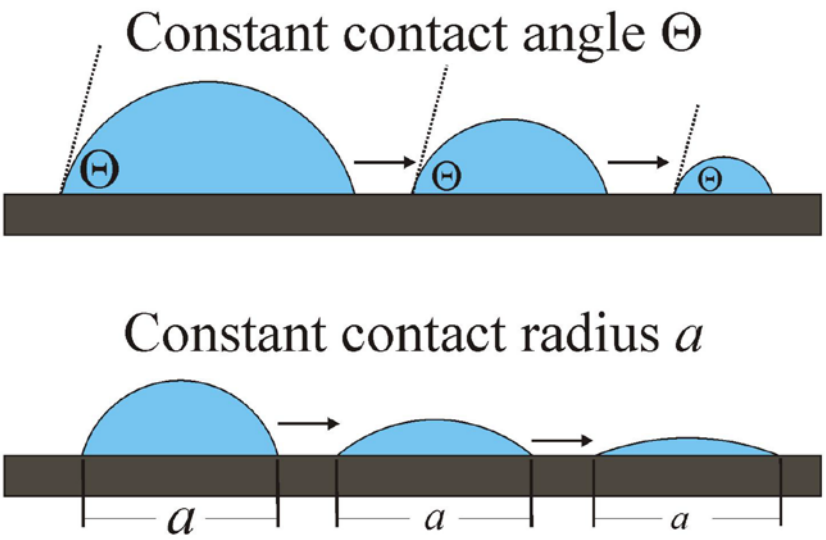

Figure 2. 5. Modes of droplet evaporation. (Top) The drop evaporates with a constant contact angle, the base radius decreases in time. (Bottom) The base radius remains constant, whilst the drop contact angle decreases in time.

The evaporative behaviour was found to depend on various factors, including surface roughness and chemical composition.

2.1.10 Hysterisis

The equilibrium contact angle given by Youngs equation holds only for ideal situations. In reality, surface heterogeneity, roughness and substrate contaminants all affect the contact angle [34]. On non-ideal surfaces there exists a difference in the contact angle for which a drop will begin to advance or recede over the solid surface. The contact angles for when the drop is advancing and receding are called dynamic contact angles and the difference between the advancing and receding value is termed the contact angle hysterisis [35]. The advancing and receding contact angles represent the upper and lower limits above and below which the contact line will begin to move. There are two fundamental sources which have been shown to instigate hysterisis in droplet evaporation. The first source is chemical in nature, and includes heterogenity of the solid surface and dissolution and/or swelling of the solid by the liquid [36]. The second source is physical in nature, and includes surface roughness, surface impurities and surface contaminants. In this case, the existence of pores and asperities is influential. On real surfaces there exists a succession of metastable states that exist

between the advancing and receding contact angle and are separated by energy barriers. Because a range of contact angles exist, rather than a unique contact angle as defined by the young equation, there exists a need to try to define an apparent contact angle, $\theta_{AP,}$ which can be used to characterise the wettability on rough surfaces. If the surface roughness is small in comparison to the drop size, the relation can be given by:

$$\cos\theta_{AP} = r \cos\theta_{eq} \quad \textbf{(2.9)}$$

Where the roughness, r, represents the ratio between the true and apparent surface area (r>1), that is to say the increased surface area has an effect on the overall contact angle which is observed. This is known as the Wenzel equation [8]. Another equation commonly used to define the apparent contact angle is the Cassie-Baxtor equation [37], which is typically employed to describe heterogenous surfaces:

$$\cos\theta_{AP} = f_1 \cos\theta_{eq1+} f_2 \cos\theta_{eq2} \quad \textbf{(2.10)}$$

in the above equation, f_1 and f_2 refer to the ratio of surface areas of the components present on the surface. Equally θ_{eq1} and θ_{eq2} represent the equilibrium contact angle of each component.

2.2 Drop Profile.

2.2.1 Bond number.

Defining a drop profile is important for any investigative purposes, one dimensionless parameter which is helpful in defining the drop profile is the bond number.

$$Bo = \frac{\rho g l}{\gamma} \tag{2.11}$$

This number relates the ratio of gravitational forces to those of surface tension. When Bo is large (>>1), gravitational forces dominate, and there is significant deformation of the drop shape. When Bo is small (<1), surface tension dominates, and gravitational forces may be neglected. When gravity is neglected the mean drop curvature is constant and the drop assumes a spherical cap shape.

2.2.2 Capillary length

Another parameter which is used in drop measurements is the capillary length, which also indicates the predominance of gravitation forces to those of surface tension:

$$\kappa^{-1} = \sqrt{\frac{\gamma}{\rho g}} \tag{2.12}$$

When the characteristic length is greater than k^{-1}, gravitational forces become important. The capillary length is useful in any study involving drops as it can help determine the maximum permissible drop radius which can be studied without the drop experiencing deformation due to gravitation forces.

2.2.3 Drop Volume

The drop volume may be expressed as:

$$V = \frac{\pi R_a^3 (1-\cos\theta_e)^2 (2+\cos\theta_e)}{3\sin^3\theta_e} \quad \textbf{(2.13)}$$

And the corresponding drop surface area is given by:

$$A = \frac{2\pi R_a^2}{1+\cos\theta_e} \quad \textbf{(2.14)}$$

The corresponding drop height is a function of the radial distance, and can be expressed by the equation:

$$h(r) = \sqrt{\frac{R_a^2}{\sin^2\theta_e} - r^2} - \frac{R_a}{\tan\theta_e} \quad \textbf{(2.15)}$$

2.3 Evaporation

Evaporation is a unique process which involves the transfer of liquid molecules from the liquid phase to the gas phase. It is therefore a phenomenon which acts at the liquid vapour boundary. It can also be described in terms of traditional kinetic theory. At the liquid vapour interface, liquid molecules are continuously entering the gas phase and re-entering the liquid phase. If the gas is already saturated with the given liquid there will be almost as many molecules re-entering the liquid as leaving, and thus there is very little net mass transfer (little evaporation) taking place. An atmosphere which is not saturated however, leads to an imbalance of liquid molecules and consequently a net driving force towards the gas phase, resulting in droplet evaporation.

When a liquid molecule is transferred to the gas phase energy is consumed. This energy loss is described by what is commonly known as the latent heat of evaporation. On the molecular level heat is a measure of the kinetic energy. In an evaporating drop the molecules which possess high kinetic energy (higher temperature) are more likely to be able to overcome the intermolecular energy barriers and enter the gas phase, thus the less kinetically energetic (lower temperature) molecules remain. This process is known as evaporative cooling and is the basis of many industrial commercial and biological thermodynamic processes. Perspiration is a method of evaporative cooling in which the body secrets liquid which then evaporates cooling the skin. In humid conditions the air is saturated with liquid and thus the cooling effect of perspiration is hindered as there is less evaporation taking place.

A liquid droplet which is evaporating on a flat surface evaporates as essentially a gas diffusion process [4]. The vapour concentration at the interface of the liquid drop is assumed to be equal to the equilibrium concentration. The rate of diffusion, I, across the liquid vapour interface can then be computed.

$$I = -4\pi r^2 \left(\frac{dc}{dr} \right) D \qquad \textbf{(2.16)}$$

Where the diffusion coefficient is represented by, D. and c is the vapour concentration. Setting the boundary conditions as:

$$c = c_\infty \text{ when } r = \infty \qquad \text{and} \qquad c = c_0 \text{ when } r = r_d \qquad \textbf{(2.17)}$$

An expression can be obtained for the rate of diffusion:

$$I = -4\pi r_d D(c_0 - c_\infty) \qquad \textbf{(2.18)}$$

From this equation the rate of evaporation can be determined by the diffusion of the vapour. Also, the rate of evaporation can be seen to be directly proportional to the radius of the drop.

3 Literature review

In this section a review of current research knowledge is given. Firstly, investigations that have elucidated the understanding of sessile droplet wetting are presented. This is then extended to the case of droplet evaporation. The more recent topic of nanofluid behaviour is then presented. An outline is given of the growing interest in nanofluids and the main research findings are discussed. The less investigated area of pattern formation is then presented, an area which is of importance to the work undertaken later in the thesis. Finally, results are presented which discuss the behaviour of interfacial phenomena, and in particular hydrothermal waves. These results are important in understanding the work undertaken in chapter 4 in this thesis.

3.1 Droplet Behaviour

3.1.1 Droplet Wetting

Knowledge of the way a liquid behaves on a solid surface is important for numerous practical applications, such as lubrication, painting, writing, waterproofing, and heat transfer, amongst many others. In spite of the importance, many processes involved in wetting are still not fully understood [3]. When a drop makes contact with flat horizontal surface, it may spread, covering the surface in a thin layer of liquid. Alternatively, it may spread partially, forming a defined, non-zero contact angle at the edge of the liquid, $\theta=\theta_e$. The extent to which a drop wets a surface is given by the Young equation, which states that the equilibrium contact angle is a function of the three interfacial surface tensions [38].

Wetting of the solid surface can be predicted using the concepts of adhesion and cohesion. Adhesive forces between the solid surface and the liquid encourage the liquid to spread. In contrast intermolecular cohesive forces within the liquid act to keep the molecules as close together as possible. The spreading coefficient is used to quantify the readiness of a particular liquid to spread on a given surface.

3.1.2 Droplet Evaporation

Understanding the processes involved in the evaporation of liquid droplets is challenging due to the multitude of simultaneous phenomena that are occurring. Heat and mass transfer, convective behaviour of both fluids, evaporative cooling, surface tension induced effects, amongst others, all combine to complicate any attempt at understanding the observed behaviour. An early work by Morse [39] studied the evaporation of a small iodine sphere resting on a flat plate and noted that the evaporation rate was directly proportional to the radius of the sphere. Similar results were obtained by Peiss [40].

Another experimental investigation [4], determined that the evaporation rate remained constant for the majority of the drop lifetime. Picknett and Bexon [7], conducted a theoretical and experimental investigation into the evaporation of small drops. In their work, the drops were small enough that gravitational effects could be neglected and a spherical cap approximation for the drop shape could be applied. In their experiments, organic drops (methyl acetoacetate) were placed on a microbalance and the evaporation rate recorded, along with the drop shape. The results indicate the presence of two distinct modes of drop evaporation, constant contact angle mode and constant contact area mode. In the paper the authors make reference to intermediate evaporative modes during which both contact angle and contact area are shown to decrease simultaneously, however it was not until the work of Bourges-Monnier and Shanahan [5], that these intermediate modes of evaporation were fully investigated. The authors investigated the evaporation of water and n-decane on three distinct polymer surfaces and also on glass slides. They concluded that there were four distinct evaporative regimes. The first was observed when the surrounding vapour phase was saturated with the evaporating liquid. It was observed that the drop was found to evaporate with a constant contact angle.

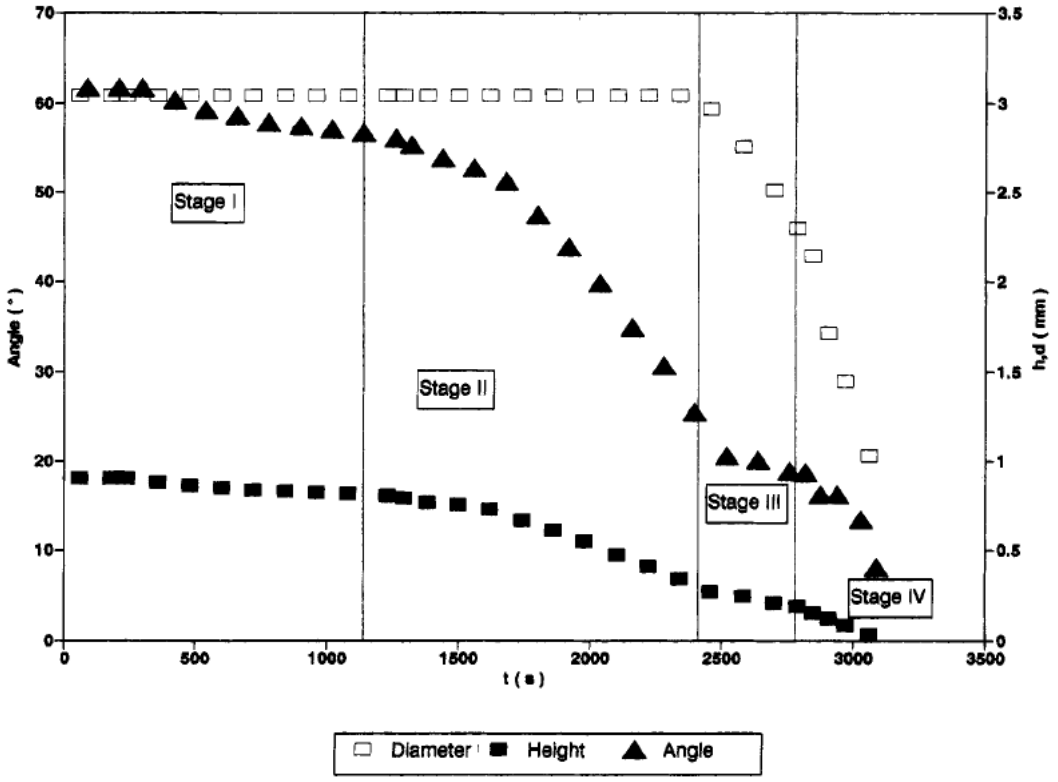

Figure 3. 1. Evolution of drop height, h, contact diameter, d, and contact angle, θ, for a water drop (initial volume 4μl) on a polished epoxy surface [5].

The second stage involves reducing the atmospheric vapour content, resulting in the contact angle and drop height decreasing during evaporation. In the third stage, which occurs on smooth surfaces, drop height and contact angle remain almost constant, with a corresponding decrease in base radius. The fourth stage corresponds to the drop disappearance, Figure 3.1. On rough surfaces drops tend to evaporate with decreasing contact angle and constant contact area.

Birdi [4] , investigated the evaporation of water on glass, and Teflon, noting that the evaporation rate is constant whilst the drop remains pinned to the surface (constant contact area mode). They also show a linear increase in evaporation rate with drop radius (see figure 3.3), which is consistent with diffusion driven evaporation,

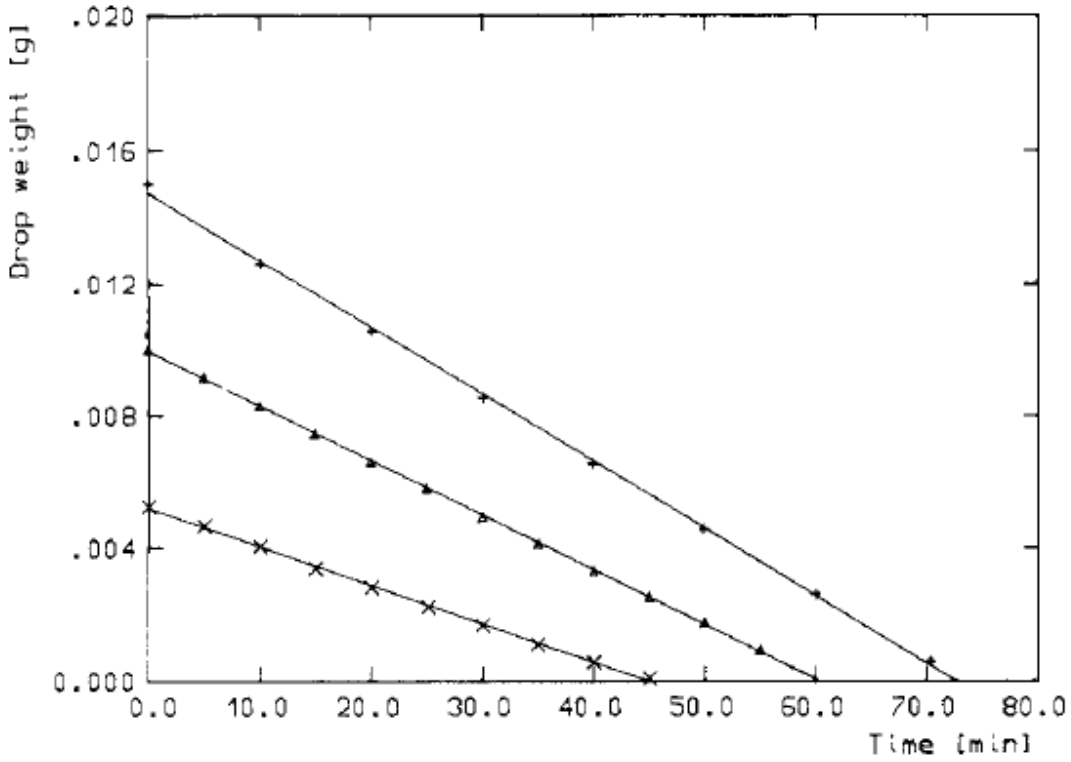

Figure 3. 2. Drop mass vs. time for sessile drops on glass surface. Initial mass of each drop: 5mg (x), 10mg (Δ), 15mg(+) [4]

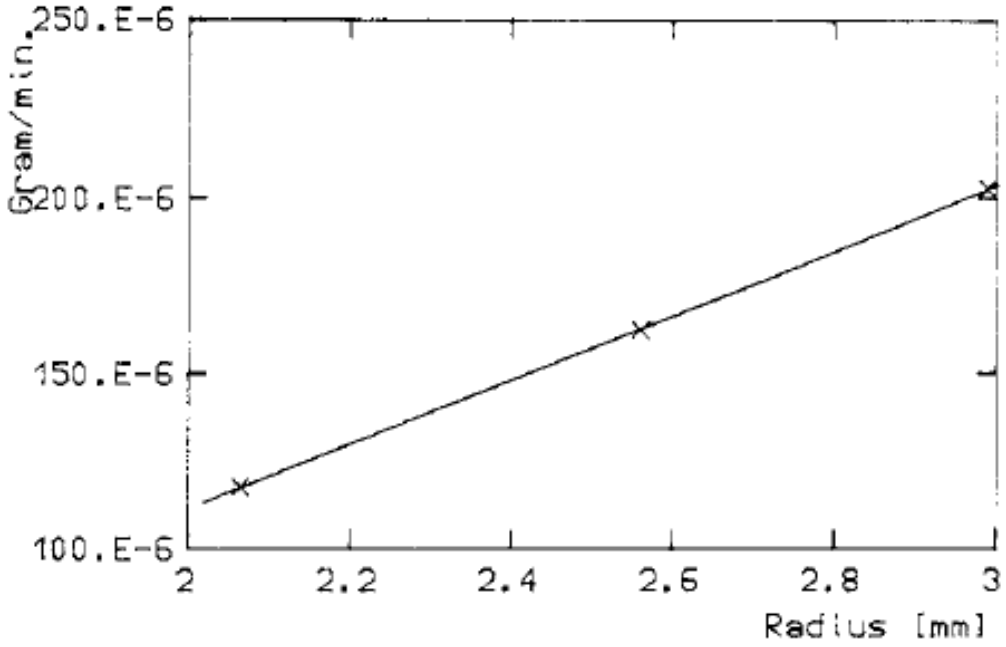

Figure 3. 3. Plot of evaporation rate as a function of initial drop radius [4].

A later investigation by the same authors [41] investigated the influence of initial contact angle on the evaporative process. The rate of evaporation of drops of liquids with partial wetting characteristics, contact angle < 90 (water on glass), was found to differ from those which exhibit non-wetting characteristics, contact angle >90 (water on Teflon), figure 3.4. Evaporation rate was linear and the drop follows the constant contact area mode of evaporation on wetting surfaces, whilst on non wetting surfaces the evaporation proceeds with a constant contact angle and evaporation rate is not linear.

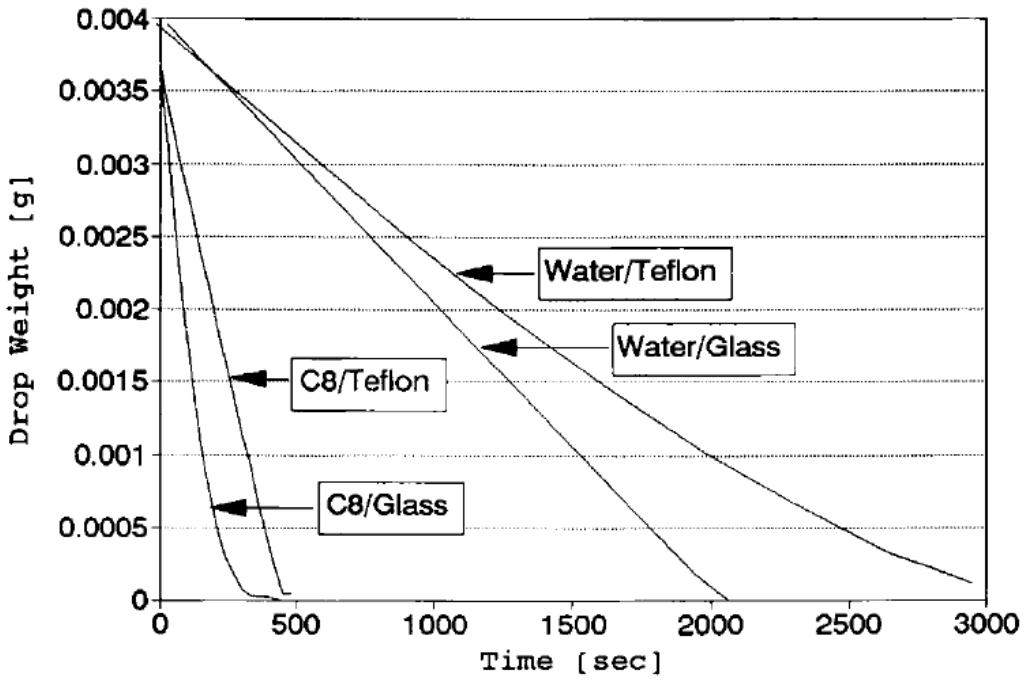

Figure 3. 4. Evaporation rates of water and n-octane drops on water and Teflon surfaces [41].

Another study [15], investigated the evaporation of droplets on a rough polymer surface. Drops were left to evaporate in open air, whilst a microbalance and optical measuring equipment recorded the evaporation rate and drop profile in time. A linear decrease in drop mass was found, along with a corresponding decrease in contact angle and constant base radius. Conversely, Rowan et al. [42], studied the change in mass and geometry due to evaporation of small droplets of water on a polymer surface (PMMA). Their results indicate that the evaporation rate is proportional to the height of the drop, not the spherical radius. The same authors later published similar results for the evaporation of three alcohols on Teflon [43].

Erbil et al. [11], conducted a study of the constant contact angle mode of evaporation. The liquids selected for the experiment comprised n-butanol, toluene, n-nonane, and n-octane. All experiments were conducted on a PTFE surface. Results were obtained using video microscopy and the results indicated a linear decrease when the square of the radius was plotted vs. time for most cases, figures 3.5 and 3.6.

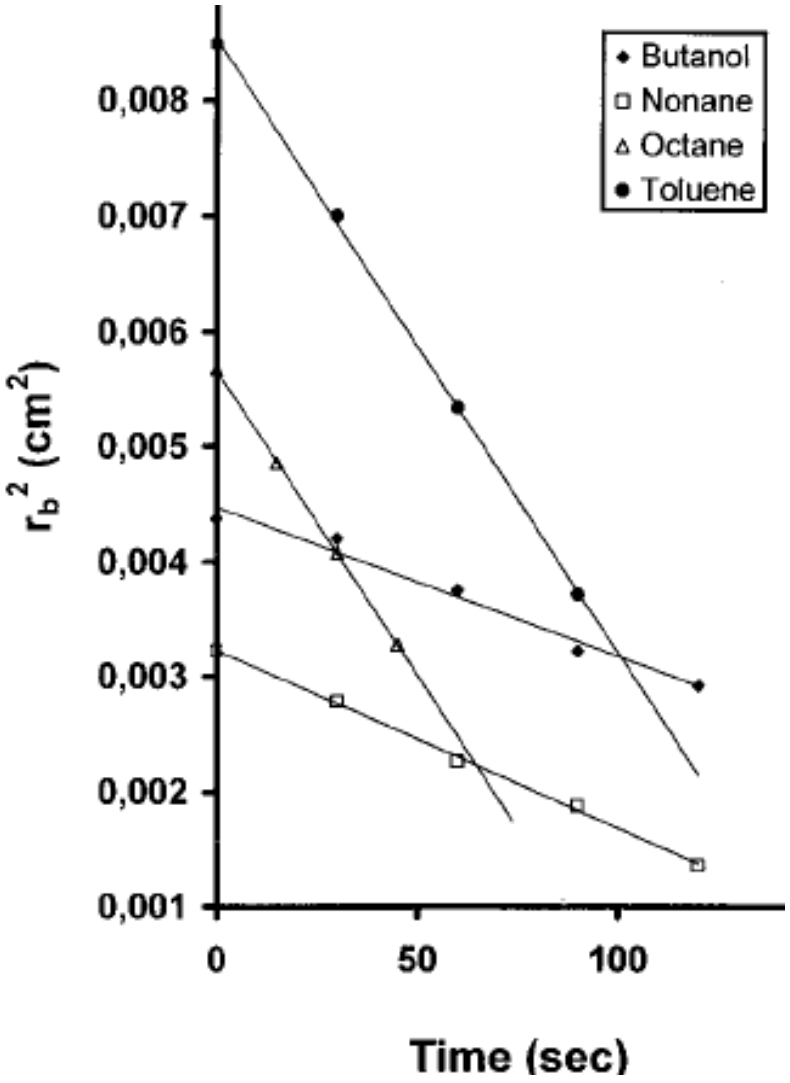

Figure 3. 5. Time dependence of the square of the drop radius for the four liquids tested [11].

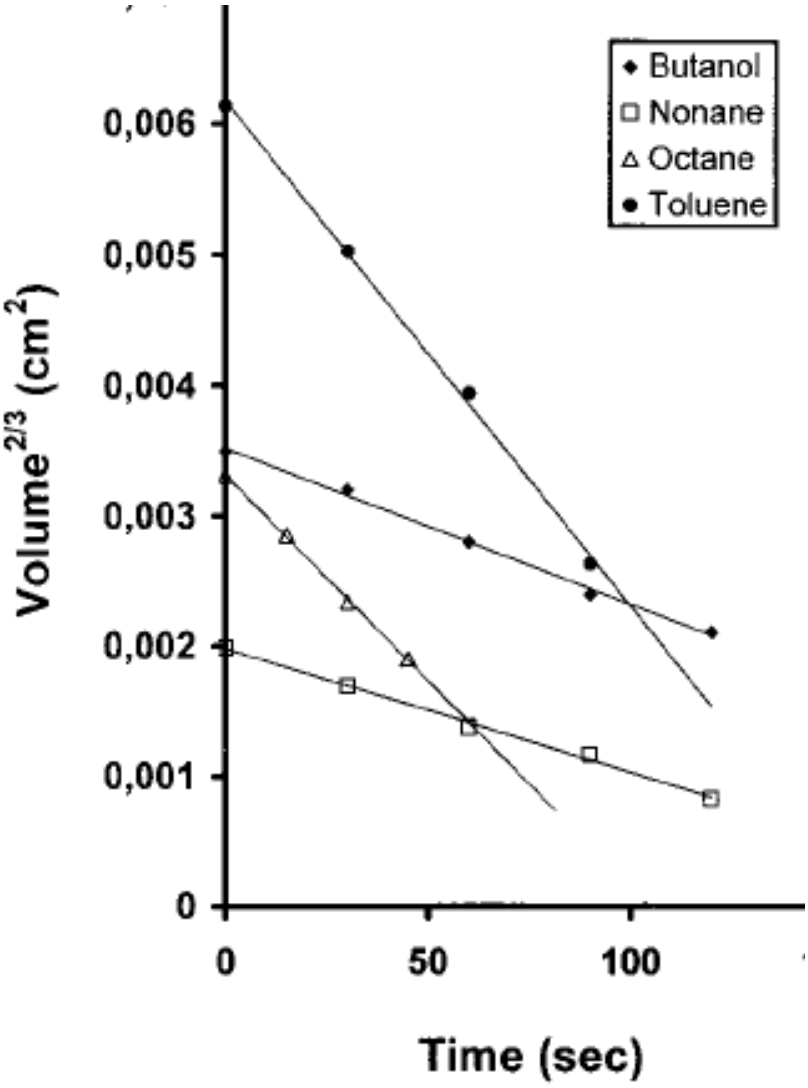

Figure 3. 6. Time dependence of two-thirds the power of the drop volume for the four liquids tested [11].

An investigation by Chandra et al. [44] studied the effect of drop contact angle on drop evaporation. They used surfactants to alter the initial contact angle observed in water drops evaporating on a stainless steel plate, and recorded the corresponding evaporation using video recordings. They found a high evaporation rate for drops with a low initial contact angle. This increase arises as a result of the larger liquid/solid interfacial area present, and also as a result of increased heat conduction due to a decrease in initial drop thickness.

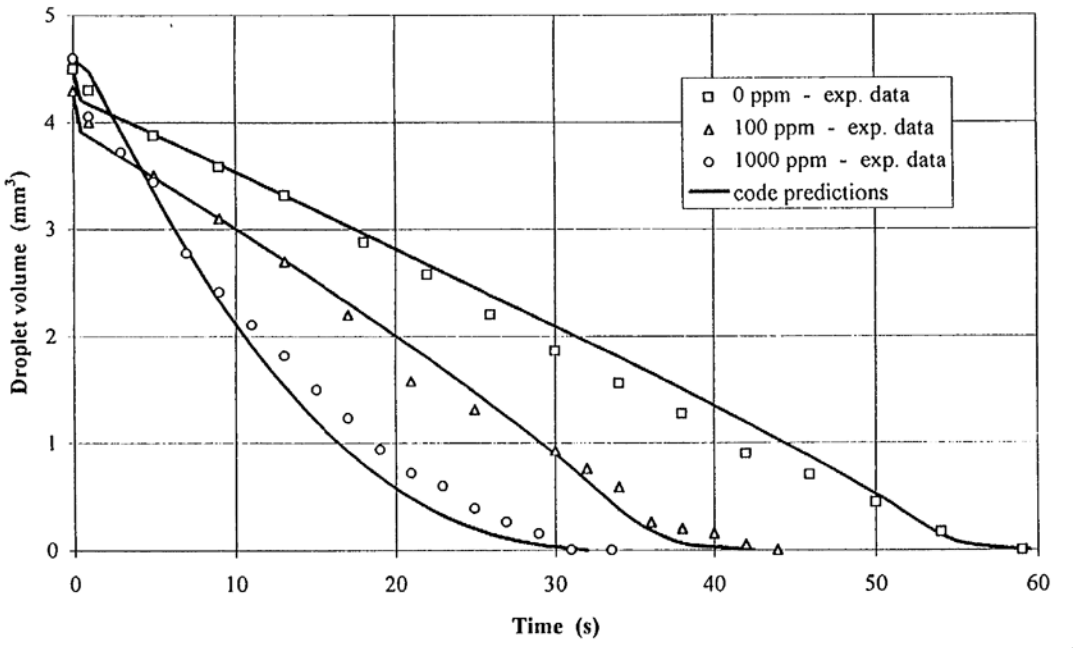

Figure 3. 7. Evaporation rate of water drops with increasing concentration of surfactant addition on a stainless steel surface [44].

Crafton et al. [45] studied the evaporation rate of small drops of both water and n-heptane on heated aluminium and copper substrates, noting a predominantly constant contact angle mode of evaporation for the n-heptane drops and a predominantly constant contact radius for water.

Deegan et al. [10], observed the evaporation of pinned drops and noted that there exists an outward flow within the drop that is driven by the loss of solvent at the contact line. This flow tends to carry any contaminants which may be present in the drop to the contact line creating rings of deposits upon evaporation. It was shown that the evaporation of liquid from the drop was greatest at the contact line of the evaporating drop, this is illustrated in figure 3.8.

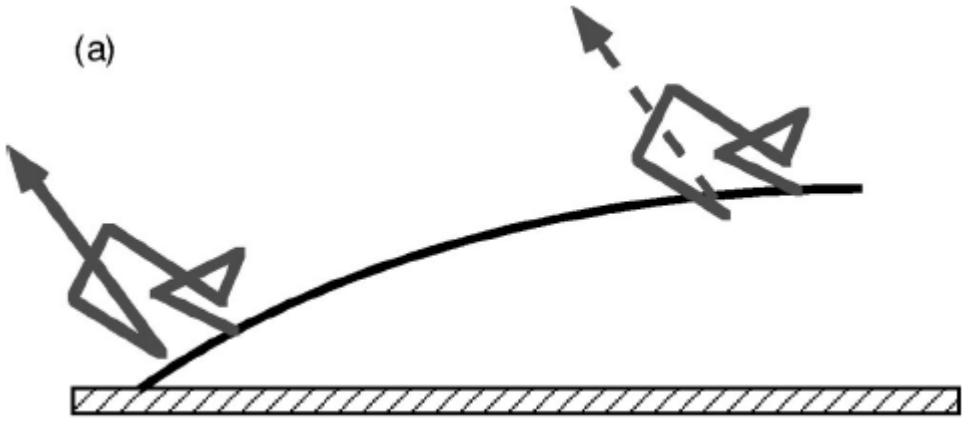

Figure 3. 8. The probability of escape of an evaporating molecule is affected by its point of departure. At the drop centre there is a higher probability of the molecule being reabsorbed, resulting in a higher evaporation rate at the drop periphery [10].

From a theoretical perspective, there have been several important investigations into droplet evaporation. Picknett et al. [7] developed a model based on the Maxwell equation which describes the evaporation of a sphere in an infinite medium

$$\frac{dW}{dt} = -4\pi Dr(c_0 - c_i) \qquad \textbf{(3.1)}$$

Where dw/dt is the rate of change of mass of a sphere with radius r, D is the molecular diffusion constant of the vapour in air, and c_0 and c_i represent vapour concentrations near the sphere and far from the sphere. Using the analogy between diffusive flux and electrostatic potential, an attempt was made to determine the evaporation rate. To do this the capacitance of an equiconvex lens of similar dimensions to the drop in question is required.

$$\frac{dW}{dt} = 4\pi DC_x(c_0 - c_i) \qquad \textbf{(3.2)}$$

where C_x is the electrostatic capacitance. By using the known solution for electrical potential of a lens shaped conductor, the authors were able to obtain an approximate solution for the mass flux from the free surface of the drop Two polynomial fits were obtained one for small contact angles ad one for large contact angles. Figure 3.9 presents the theoretical data for both constant contact angle and constant base radius evaporation.

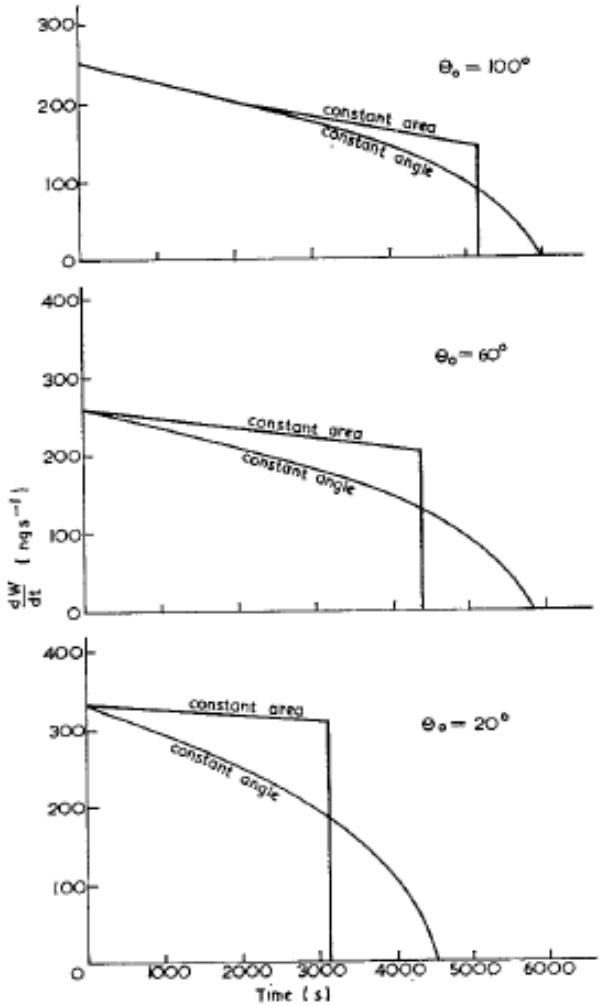

Figure 3. 9. Theoretical evaporation rates for 1mg drops of methyl acetoacetate on a surface at 22-23°C [7].

Birdi et al. [4] developed a vapour phase diffusion model to test the experimental results they had obtained, this was later incorporated by Rowan et al. [42], who derived an approximate analytic equation for the evaporation rate. They distinguished between the radii of curvature at the contact line, noting that they are, in general,

different. They found a good agreement with experimental results for drops with a large initial contact angle.

Deegan [10], studied the evaporative process using electrostatic analogy. They describe the radial fluid flow inherent in an evaporating drop with a pinned contact line,figure 3.10.

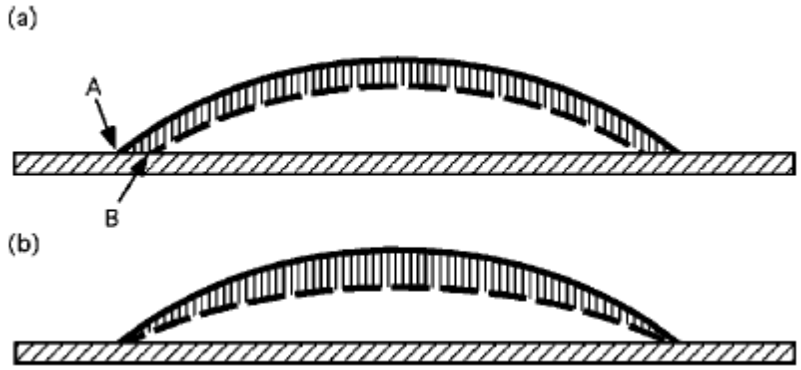

Figure 3. 10. Illustration of the origin of fluid flow in an evaporating drop. (a) When a drop is not pinned the hashed area evaporates freely and contact line will move from A to B. (b) When the drop is pinned the motion from A to B is inhibited by liquid replenishing that removed from the drop edge [10].

Mathematically, an equation can be written describing the vertically averaged radial flow of the fluid.

$$v(r,t) = -\frac{1}{\rho r h}\int_0^r dr.r\left(J_s(r,t)\sqrt{1+\left(\frac{\delta h}{\delta r}\right)^2} + \rho\frac{\delta h}{\delta t}\right) \qquad \textbf{(3.3)}$$

In this equation h represents the position of the air-liquid interface, J_s represents the rate of mass loss per unit area per unit time, t is time and ρ represents the fluid density. It can be seen that v has a non-zero value when there is a difference between the local evaporation rate and the rate of change of the interface. Theoretically the current diverges near the contact line.

$$J(r,t)(R-r)^{-\lambda} \quad \textbf{(3.4)}$$

Where

$$\lambda=(\pi-2\theta_c)/(2\pi-2\theta_c) \quad \textbf{(3.5)}$$

Thus evaporation is greater in the vicinity of the contact line. The drop volume must be equivalent to the rate of mass loss due to evaporation, and therefore the following equation can be written for evaporation rate.

$$\frac{dM}{dt}=\int_0^R dr'2\pi r' J_s(r',t)\sqrt{1+\left(\frac{\delta}{\delta r'}h(r',t)\right)^2} \quad \textbf{(3.6)}$$

Hu et al. [6] used a finite element method to investigate the evaporation of pinned sessile drops and to compare the theoretical results with those obtained by experimental work. A good agreement was obtained between their analysis and that of Deegan.

3.2 Nanofluid Behaviour

3.2.1 Experimental investigations into Nanofluid behaviour

The idea of increasing the thermal conductivity of a liquid by suspending particles in the bulk fluid is not a new one; Maxwell formulated a theoretical basis to calculate the thermal conductivity of a particle-fluid suspension over a hundred years ago[46]. Whilst Maxwell's theory predicted large thermal conductivity enhancements, achieving stable suspensions proved to be very difficult. Technological limitations meant that particle sizes in the suspensions were limited to, at best, micro-sized particles. The relatively large sizes of the particles led to large scale sedimentation, pipe fouling, erosion, and large increases in fluid pressure drop. Consequently the use of particulate slurries as a means of heat transfer was effectively discarded. However, with the advances that have been made in nano-scale engineering, it is now feasible to readily produce nano-sized particles. This has led to a return to the idea of using particulate suspensions in heat transfer applications. Nanofluid suspensions do not experience large scale sedimentation like their micro-sized counterparts, and fouling and pipe erosion is greatly reduced. In effect the nano-sized particles can, under the correct conditions, form a stable suspension in which the effective thermal conductivity of the fluid is greatly enhanced, whilst particulate settling and fouling are negligible [1]. Several authors have published work on different nanofluids such as Al_2O_3 and CuO nanoparticles in water, ethylene glycol, and engine oil (Pennzoil 10W-30) [1, 47-50]. In each case there was a clear enhancement of conductivity compared to that of the base fluid. Further work on metallic nanofluids has yielded similar results, with one report noting a 40% conductivity enhancement using copper particles in ethylene glycol with a particulate concentration of just 0.3% [1]. Similar results were also noted with various other reports[51-57].

It is clear from the data that has been collated that there is a marked increase in thermal conductivity with increasing nanoparticles concentration; however the degree of enhancement which has been reported varies from nanofluid to nanofluid. It is clear that the mechanisms that underpin the observed enhancement rely on many factors such as particle size, particle shape, aggregation of particles, concentration, and

temperature [58]. Cleary, obtaining a theory that can encompass the work that has been done so far is an area where continual effort is required.

3.2.2. Theoretical modelling of Nanofluid behaviour

The Edinburgh born physicist James Clerk Maxwell [46], first investigated using spherical solids suspended into liquids to increase the overall thermal properties of the suspension. He proposed a model which calculated the observed thermal conductivity enhancement. In this model the suspension was assumed to consist of a dilute solution of spherical particles, with particle interactions neglected.

$$k_{\max well} = \frac{k_p + 2k_l + 2(k_p - k_l)\phi}{k_p + 2k_l - (k_p - k_l)\phi} k_l \qquad \textbf{(3.7)}$$

This model was later adapted by Hamilton & Crosser [59] to include the effect of particle shape, allowing for the inclusion of non-spherical particles in suspension.

$$k_{HC} = \frac{k_p + (n-1)k_l - (n-1)\phi(k_l - k_p)}{k_p + (n-1)k_l + \phi(k_l - k_p)} k_l \qquad \textbf{(3.8)}$$

In the above equation the empirical shape factor is given by:

$$n = \frac{3}{\Psi} \qquad \textbf{(3.9)}$$

Where Ψ is the sphericity, defined as the ratio of the surface area of a sphere with a volume equal to that of the particle to the surface area of the particle. Early studies on nanofluids showed that whilst the Hamilton & Crosser model worked well for micro-sized solid slurries, it under predicted the enhancement observed in nanofluids (Figure 3.11). In this model the effects of the solid/liquid interface and the dynamics of the particles are not taken into account, both of which are influential at the nanoscale. In the Hamilton-Crosser model, which is based on diffusive heat transport, particle size is not taken into account. However, experimental results have shown that the observed conductivity enhancement is increased with a reduction in particle size.

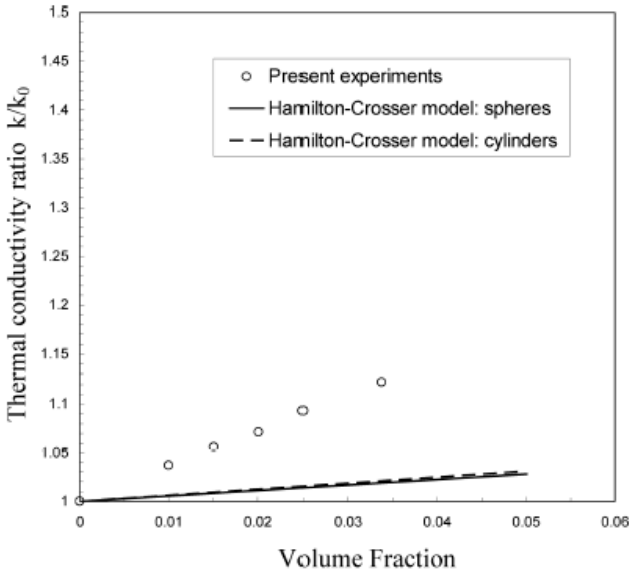

Figure 3. 11. Experimental observations show a much higher increase in thermal conductivity than predicted by theoretical models such as that of Hamilton & Crosser .

Various other extensions to the Maxwell equation have been described. These have been constructed to account for factors such as, particle distribution, concentration, contact resistance & particle shell structure. These models have provided the basis for comparison for most of the theoretical models published for nanofluids. However, experimental results have consistently shown much higher effective conductivities than predicted by theory. Keblinski et al [58]. made an attempt to explore possible explanations for this enhancement, outlining four possible mechanisms, Brownian motion, liquid layering at particle interface, heat transport in the particles, and clustering effects.

3.2.3. Nanofluid Viscosity

Central to the application of nanofluids in cooling technologies is the performance of the fluid in convective environments. As a consequence, fluid mechanical behaviour is very important. The viscous behaviour of particle-liquid mixtures is a topic that has been widely studied. Einstein set down an equation to predict the effective viscosity of a particle-liquid mixture in 1906 [60].

$$\mu_e = (1 + 2.5\nu_p)\mu_m \qquad \textbf{(3.10)}$$

This equation has been refined and adapted to account for higher concentrations [61-63], non-spherical particles [64], and to include particle-particle interactions [65]. Whilst there has been much work done on the viscous behaviour of particulate suspensions, there remains a lack of data for the specific case of nanofluid suspensions. Pak and Cho [38], conducted a study into the behaviour of Al_2O_3 & TiO_2 particles in water, concluding that there was a significantly larger effective viscosity measured than predicted by theory. Das et al [66], then measured the viscosity against shear rate for nanofluids at various temperatures and confirmed that they were independent of each other (Figure 3.12), indicating Newtonian behaviour.

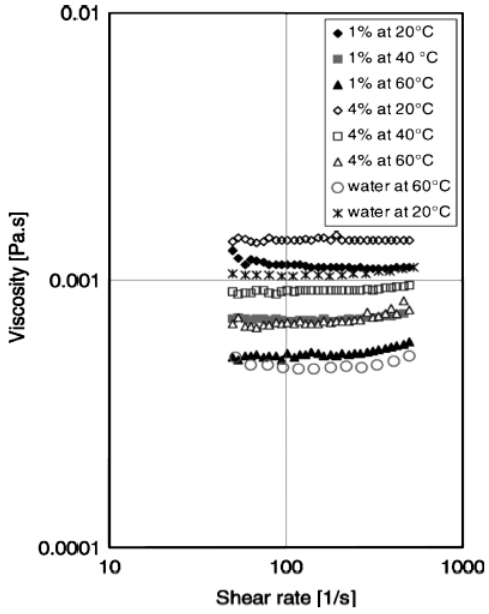

Figure 3.12 Viscosity against Shear Rate for various concentrations and temperatures of nanofluid solution.

Putra et al [67] and Mare et al [68] also published results which details temperature dependent conductivity data for Al_20_3-water nanofluids (Figure 3.13). Very recently Nguyen et al [69], measured the effects due to temperature and particle size on viscosity for volume fractions varying from 1% to 9.4%. Their results indicated that viscosities were found to be strongly dependent on temperature and volume fraction. Their results also revealed the existence of a critical temperature beyond which the particle suspension properties appear to be drastically altered, leading to a hysterisis effect. This phenomenon has raised concerns regarding the reliability of certain nanofluids for use in heat transfer applications.

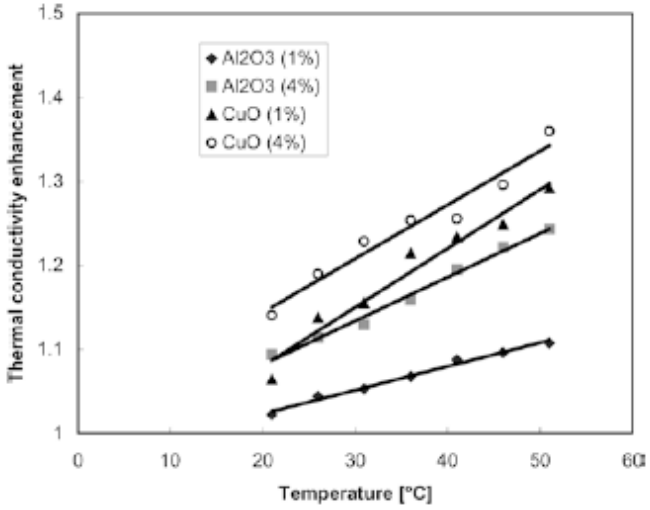

Figure 3. 13. Thermal conductivity enhancement as a function of temperature. Putra et al [67].

3.2.4. Nanofluid flow phenomena

One of the first major works in which particles were used in liquid suspensions to observe fluid flow was the seminal work of Deegan [10]. In his study he studied the age old observation of coffee-ring formation, solid ring like spots found as a result of coffee evaporation. This phenomenon was found to be influenced by evaporation at the contact line. As liquid molecules are removed from the contact line, they are then replenished by a flow of liquid molecules to fill the newly created gap. This continuous replenishment effectively constitutes a flow of liquid from the drop centre to the drop periphery. In particle-liquid suspensions, particles were found to be carried

by the flow to the drop periphery, creating a ring like concentration of particles. In Deegan's work, he found that the particles at the contact line increased the pinning effect, in effect strengthening the contact line. An immediate conclusion which could be drawn form Deegan's work was the pattern forming ability of the phenomenon.

3.2.4.1 Contact Line

The way nanoparticles behave in solution is a very recent area of study, and little work has been conducted in this area. Wasan and Nikolov [70], provided one of the earliest observations of nanoparticle behaviour in suspension. They studied the behaviour of nano-sized polystyrene spheres in water; using video microscopy to demonstrate that at the three phase contact line a solid like ordering of the particles exists. The solid like particle layers were found to enhance the spreading dynamics of the fluid, which is very useful in detergency. In a similar study [71], they were able to characterize nanoparticles behaviour in a confined geometry. A thin liquid film was drawn from a colloidal suspension of highly charge latex particles (d=156nm). The film was found to consist of distinct layers of nanoparticles, increasing until around five nanoparticles diameters, where a random particle structure begins (Fig 3.14).

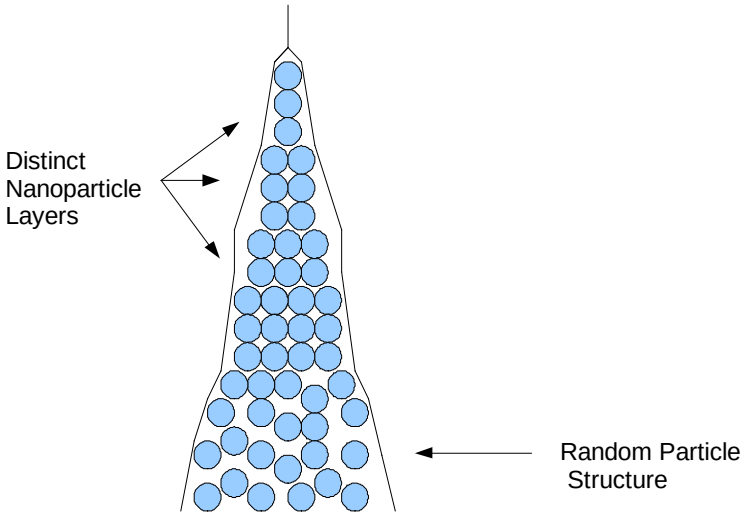

Figure 3. 14. Ordering of nanoparticles in the wedge of a thin liquid film. As the thickness of the film increases, the structured behaviour is replaced by random particle motion.

This step-wise thickness profile indicates that in confined geometry, a self-structuring property exists; furthermore, the structure also changes with an increase in film thickness. For a film thickness of 1- 2 nanoparticles a (2-D) hexagonal packing structure was observed, this was not observed for 3 particle diameters or greater. The main implication was that the packing structure provided a barrier to bubble and droplet coalescence.

In another study [72], the same authors examined the spreading of nanofluid suspensions on solids. The aim of the study was to examine the effects of particle structure formation at the contact line region and also the structural disjoining pressure, to see what effect they have on the spreading of the fluid. Previous investigations have shown that increased pressure arising from particle ordering at the contact line enhances the spreading capabilities of the fluid [73]. The spreading coefficient was found to increase with decreasing film thickness, indicating the wetting enhancement is due to layered particle structuring. (Fig 3.15),

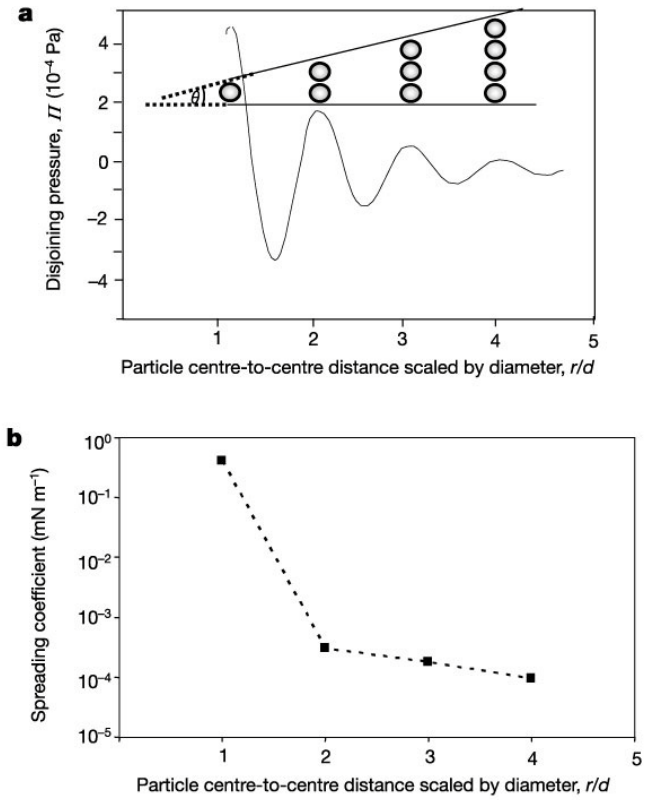

Figure 3. 15. a) Relationship between oscillatory disjoining pressure and the particle distance.
b) Spreading coefficient plotted against particle distance [73]

this corresponds to where the in-layer structure becomes ordered. From a detergency perspective, the investigation examined oil removal using a surfactant micellar solution. Micellar layering in the wedge region of the solution was found to increase the disjoining pressure, causing the oil-solution interface to advance and replace the oil from the solid surface until it was completely detached. Chengara et al. [74], expanded this work by simulations examining the effects of nanoparticle size, concentration and poly-dispersity on the displacement of an oil-aqueous interface with the aqueous bulk containing nanoparticles. They found that displacement of the contact line was greater with a high nanoparticle volume fraction. Also for the same volume fraction displacement increased with smaller particle sizes. By ensuring that these particles are as monodisperse as possible, and are present in a sufficient volume fraction, more effective detergency can be achieved.

3.2.4.2. Contact Angle

It is known that droplet contact angles have an effect on the overall evaporation rate of a droplet. Chandra et al. [44], showed that by modifying the initial contact angle of water, the evaporation rate could be increased. This was done by adding surfactants to the liquid to reduce the initial contact angle. They found that by decreasing the initial droplet contact angle from 90^o to 20^o the evaporation time was reduced by approximately 50%. It is therefore interesting to investigate the influence of nanofluids on contact angle, and thus their influence on the evaporation rate. Vafaei et al. [75] investigated the change in contact angle of nanofluids functionalized with thioglycolic acid molecules as a function of concentration, size of particle, and composition of substrate. Bismuth telluride nanoparticles (2.5 & 10.4 nm in diameter) were dispersed in water and functionalized with thioglycolic acid groups to prevent agglomeration. Contact angle was found to increase with increasing concentration, reach a maximum, and then decrease. This phenomenon was found for both particle sizes, and on both silicon and glass substrates (Fig 3.16).

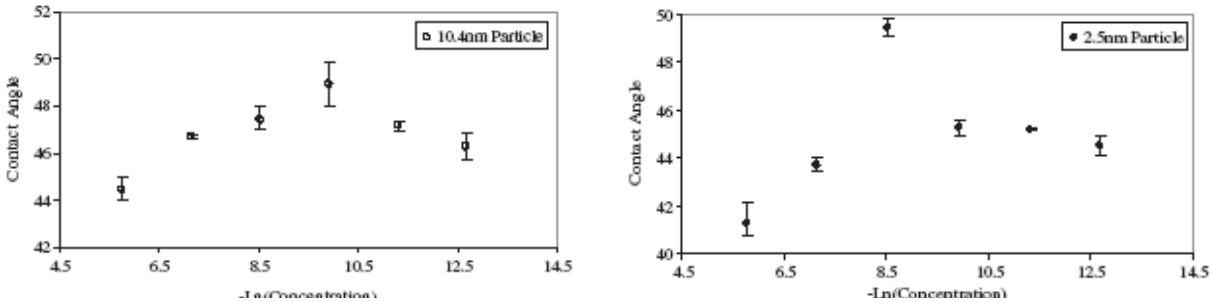

Figure 3. 16. Equilibrium contact angle as a function of Nanofluid concentration. Vafaei et al[45].

These results indicate the ability of nanofluids to alter the wettability characteristics of the bulk fluid, and possibly enhance the evaporation. A recent study conducted by MacGillivray & Sefiane[76] at Edinburgh University has also investigated the effect of nanoparticles on the contact angle. In this study nanofluids (Aluminium particles in Ethanol) of varying concentrations (0.01-5.00 % wt/wt) were examined in droplet form as the drops were advancing and receding over a substrate. The affect of the nanofluid concentration on the observed advancing and receding contact angles were observed (Fig 3.17).

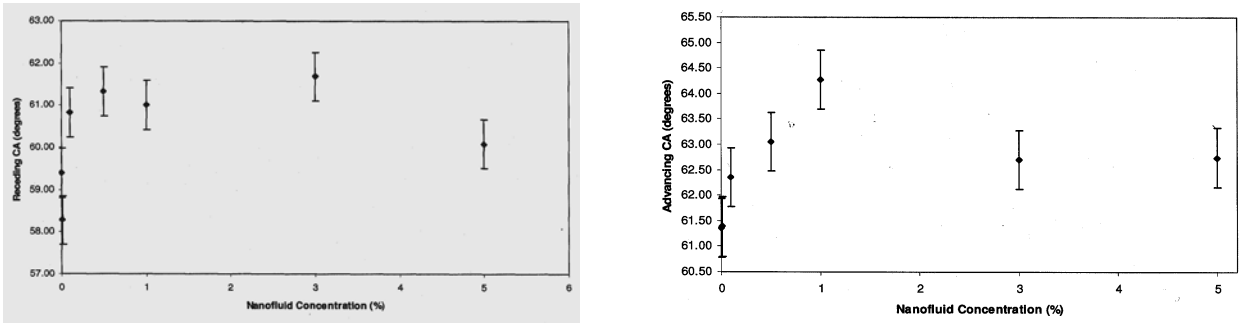

Figure 3. 17. Plot of advancing and receding contact angles against nanofluid concentration. The effect of concentration has been shown to alter the contact angle in both cases. a) Receding contact angle b) Advancing contact angle (MaGillivray & Sefiane [46].

These results appear to be similar to the equilibrium contact angle results of Vafaei, with a maximum contact angle observed at a certain concentration and a decrease of contact angle for any further concentration increase. This phenomenon was observed for both advancing and receding contact angles.

3.2.5 Pattern formation

Using the ability of evaporating liquids to position solid particles into organised patterns has many possible applications, such as in paint drying and ultra-thin film formation. The fabrication of highly-ordered thin structures is a must for the advancement of many scientific areas, such as optics, electronics and in surface chemistry. Deegan et al. [10], built upon his earlier work on evaporating drops, providing a theory which accounted for the flow velocity, the rate of growth of the ring, and the distribution of solute within an evaporating drop containing small particles. The success of this theory was found to be suited for sub-micron sized particles, with deterioration in the predicted ring growth for particles which were of 1μm in size. They observed stratification in the micro-sized particles which was not observed in nano-sized experiments. Several important factors were not investigated such as vertical mixing, viscous stresses, and Marangoni effects; all which have some bearing on the deposition of the solute. By recognising that 100% of the solute can be transferred to the drop edge, combined with the fact that the deposition can be controlled to some extent by means of manipulating the vapour field around the drop, the potential for pattern formation becomes apparent.

Maenosono et al. [77], utilized this pattern forming potential to study the growth process of an array of colloidal semiconductor nanoparticles (quantum dots). Nanoparticle rings were prepared using 5 nm CdS and CdSe/SdS (core/shell) particles suspended in both water and pyridine. These suspensions were deposited on glass, with a drop radius of approximately 1.2mm and drop volume of around 0.3μl. They noted that the ring width was dependent on the initial volume fraction of the solute, and also that the use of organic solvent introduces peculiarities of ring growth which are not present with water suspensions. They were thus able to readily produce nanometer-sized arrays of semi-conductive nanoparticles.

Sommer et al. [78] studied the effect of the gravitational force on particle deposition. Evaporative ring patterns were investigated, this time using nano-particles of 2 distinct sizes. The effect of gravity on the deposition of 10 μl drops containing equal volumes of 60 and 200 nm polystyrene nanospheres was studied. Analysis of the ring

deposits using optical and atomic force microscopy yielded interesting results. At the outer ring edge, a crystalline structure formed by densely packed and highly ordered 200 nm spheres was found. In the surrounding ring-apex there was a predominance of 60 nm particles (Figure 3.18).

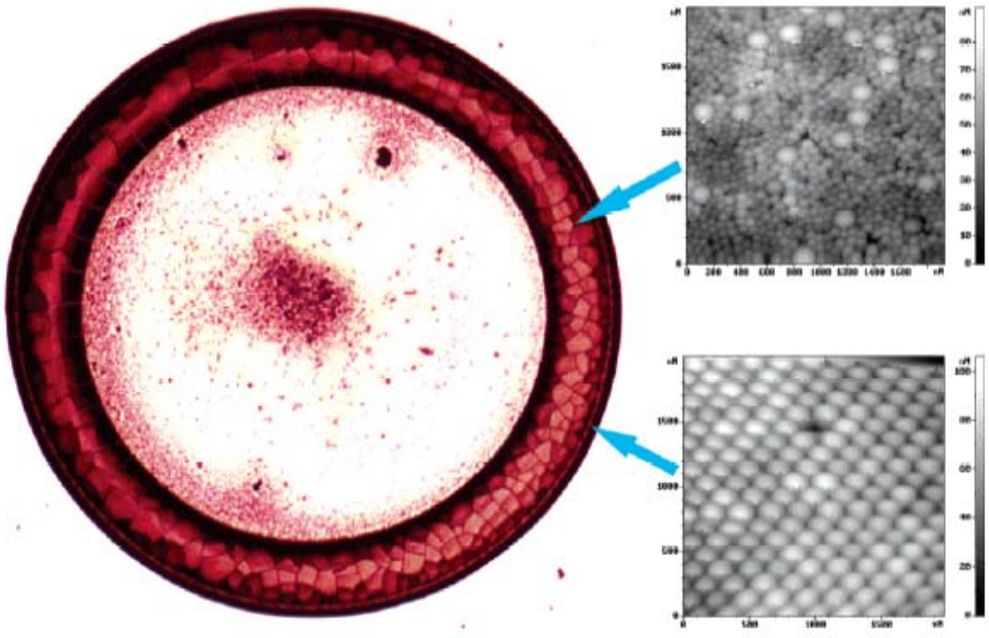

Figure 3. 18. Ring of nanoparticles formed by the evaporation of a sessile droplet. A nanofluid containing equal volumes of 200nm & 60nm particles was studied, the evaporative ring was found to favour the 200nm particles at the outer drop periphery, with the 60nm particles in the inner layer. Sommer et al [78]

This phase separation was noted to be as a result of three major factors 1) depletion of the surface tension at the triple line, as described by Deegan et al. 2) a vertical temperature gradient, the driving force behind the ascendancy of nanospheres to the drop apex, and 3) gravity, causing sedimentation and settling of larger particles. What this work does not take into account, is the role of capillary attraction, which will be greater for the larger nanospheres, and may have a role in the observed phase separation. Prevo et al. [79], fabricated gold nanocoatings using a convective assembly method at high volume fraction. Traditional vacuum deposition and electrostatic self-assembly methods cannot be used to fabricate such multilayered films, leading to applications in nonlinear electronics and quantum electronic devices as well as in chemical/bio sensors. Uniform films of gold were produced without the need for pre-treatment or the use of ligands to aid deposition. 10-30µl droplets of

nanofluid were injected into a wedge between a flat substrate and movable screen (figure 3.19).

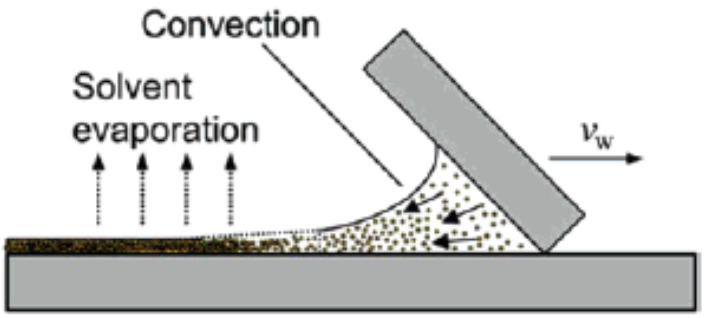

Figure 3. 19 Nanoparticle pattern formation as a result of controlled solvent evaporation. The velocity of the receding screen could be manipulated, along with the substrate temperature, to produce various structures upon evaporation. Prevo et al. [79].

Capillary forces held the drop between the surfaces and thin films were formed by drawing the screen across the substrate, stretching the meniscus. The underlying structure of the nanocoatings could be controlled by both by speed of deposition, and also by post-deposition heating. Intricate manipulation of these techniques allows for a wide range in the spectral and electronic properties observed, from a near-percolated structure (conductivity around 2000 ohm $^{-1}$ cm^{-1}) to discontinuous insular structure (less than 10 ohm $^{-1}$ cm^{-1}).

A similar study was conducted by Huang et al. [80], into the formation of stripe patterns through dewetting of nanofluids, figure 3.20. Spoke like patterns of nanoparticles were formed during the evaporation of thin films of gold nano-particles. In the initial dewetting stage, particles were observed to cluster along the contact line, as evaporation proceeds these clusters seem to serve as nucleation sites, drawing in more nanoparticles as evaporation continues.

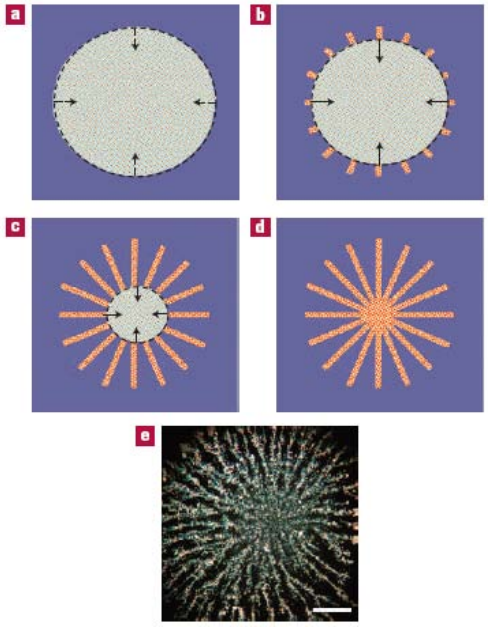

Figure 3. 20 a) Evaporation of a thin film reaches the dewetting stage where the contact line begins to recede. b) Local pinning of the contact line caused by particle clusters leads to areas of high particle density. c) As evaporation proceeds, particles are drawn towards the receeding liquid front. d) Spoke like bands are observed after complete evaporation. e) Spoke like image of evaporated liquid film Huang et al. [80].

This phenomenon was extended by using a dip coating technique to obtain linear nanoparticles alignments, with uniform thickness and inter-stripe distance. This study was primarily interested in the ability to create and manipulate patterns by evaporation; however an insight is gained into the fundamental evaporation mechanisms as a result. Using the observations of Deegan, Chon et al. [81], investigated the formation of particulate rings during evaporation. They investigated the patterns formed using different types of nanoparticles (Au, Al_2O_3, and CuO) in distilled water. The nanofluid drops (0.5% vol) were placed on a heater array held at 80^{o}C. Larger nanoparticles were found to form the most distinct rings, with smaller particles forming less pronounced rings. They postulated that slower flow and higher viscous effects inherent in suspensions which contain small nanoparticles may account for this observation.

A highly uniform deposit of nanoparticles was achieved by Bigioni et al. [82], using attractive particle-interface interactions, combined with rapid early stage evaporation,

2-dimensional nanoparticles solutions were found to grow at the liquid-vapour interface (Fig 3.21).

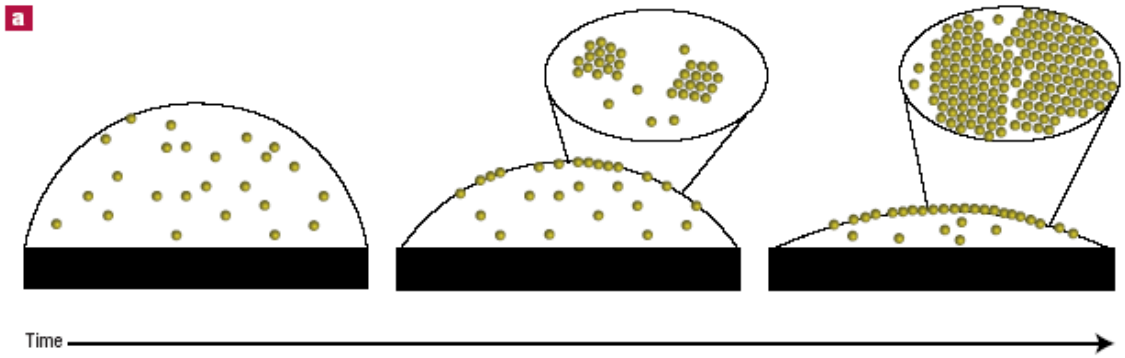

Figure 3. 21 Evaporation of a pinned sessile drop containing surface active particles. As the evaporation proceeds, the particles migrate to the liquid-vapour interface. When the evaporation is of sufficient speed, a 2 dimensional nanoparticle film can be grown. Bigioni et al [82]

This leads to the formation of thin films of highly ordered monolayers of nanoparticles. Even though the evaporation process may be very far from equilibrium, the monolayer formation is achieved. Manipulation of this technique may be particularly useful in ultra thin film materials for sensors and magnetic storage devices. By slowing down the evaporation rate, no monolayer formation was observed, and the Deegan like ring structure was observed. Gordon and Peyrade [83], recently showed that the capillary forces which drive particle agglomeration in colloidal suspensions can be also be used to separate them. By manipulating surface wettability and creating templates with desired specifications nanoparticles can be separated. By restricting the geometry of the evaporating fluid the free surface of the liquid is affected (Fig 3.22).

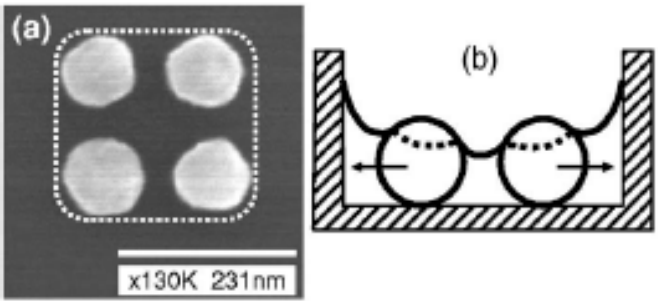

Figure 3. 22 a) nanofluids can be deposited in cells of various geometries. b) The free surface of the liquid in confined geometries acts to provide a net force which 'pulls' the particles towards the cell walls [83].

The perceived tilt in the contact line results in a net force which drives the particles toward the wall. In this way Au nanoparticles (d=50-200nm) in solution were separated by immersion in lithographically patterned substrates and then evaporating the liquid. Different geometries were also tested, circles, squares, rectangles, and triangles. These geometries could be used to localise the nanoparticles resulting in very precise placement of nanostructures, which have resolutions much smaller than that used in lithography alone, with length scales of <100nm achievable.

4 Infra – red measurements of volatile liquid drops.

4.1 Introduction

In this chapter the evaporative behaviour of several volatile liquid drops is investigated using infra red thermography. Four liquids were tested in these experiments, Water, Methanol, Ethanol, and FC-72. In addition, four distinct surfaces were investigated, Teflon, Macor (ceramic), titanium, and copper. The effect of substrate temperature was also investigated. Spontaneously occurring hydrothermal waves (here after referred to as HTWs) and patterns are identified in evaporating droplets; HTWs are thermally induced travelling waves [84], which occur in the absence of surface deflection, and obtain their energy via the application of temperature gradients. Previous observations of HTWs have been reliant upon fixed prescribed temperature gradients and constant thickness fluid layers, and have not been observed during evaporation.

4.2 Experimental Parameters

4.2.1 Liquids

The four liquids used in this experiment were de-ionised water, methanol, ethanol, and FC-72. The liquids were selected to provide a range of volatilities. In addition, all the liquids are readily available and are used in many wide ranging applications. The boiling points of each liquid are 100, 78.3, 64.7, and 56°C, respectively, under standard atmospheric conditions. Ethanol and methanol were purchased from Fisher Scientific (Loughborough, UK). FC-72 is a clear, colourless, fully-fluorinated liquid. It is thermally and chemically stable, non-flammable, and leaves essentially no residue upon evaporation. FC-72 was purchased from Fisher. De-ionised water was supplied from a high purification system called the “Barnstead NANOpure Diamond” system. It supplies water with a resistivity of 18.2mΩ/cm. Details of the physical properties are given in table 4.1.

		Water	Ethanol	Methanol	FC-72
γ	mN/m	71.99	22.39	22.07	10.00
ρ	Kg/m^3	998	789	790	1680
κ^{-1}	mm	2.71	1.7	1.69	0.78
μ	mPa.s	0.890	1.200	0.544	0640
BP	°C	100	78.3	64.7	56

Table 4.1: List of physical properties of the various liquids used in the experiment.

4.2.2 Substrates

To investigate the effect of substrate material on the test liquids, four different substrates were selected. These were chosen so that they represented a large degree of difference in their respective thermal conductivities. The four surfaces were PTFE, Macor (ceramic), titanium, and copper, and their respective thermal conductivity values were 0.25, 1.46, 21.9, and 401 $Wm^{-1}K^{-1}$. Care was taken to ensure homogeneous wettabilities and accurate contact angle measurement; to this end, the substrates were coated with a very thin layer of fluoropolymer Cytop. PTFE is a common polymer which is characterised with a low surface energy and thermal conductivity. MACOR is a brand name for a glass ceramic material. White in appearance, the material is composed of 55% fluorophlogopite mica and 45% borosilicate glass. It has a thermal conductivity that is similar to that of glass. Titanium and Copper are common metals that have many wide ranging uses. The thermal conductivity of Copper is higher than that of Titanium which is useful in these experiments for giving a comparison of two conductive materials. A table of physical properties of each surface is given in Table 4.2.

		PTFE	MACOR	Titanium	Copper
k	$Wm^{-1}K^{-1}$	.25	1.46	21.9	401
ρ	Kgm^{-3}	1200	2500	4507	8940
Cp	$Jg^{-1}K^{-1}$	1	0.79	0.523	0.385

Table 4.2: Physical properties of the various surfaces used in the experiment.

4.3 Experimental Setup

4.3.1 Infrared Camera

The Infrared camera used in this experiment was a FLIR Thermacam SC3000, which has a range of -20 to 20 000 °C and a thermal sensitivity of 20mK. A microscopic lens was fitted to the camera with a 10 X 7.5 mm^2 field of view and a minimum focal length of 26mm. Accompanying software was supplied which enabled the images to be acquired and stored in digital format. The spatial resolution of the system is 8-9 μm. To obtain images of the drop behaviour, the Infrared camera was mounted directly above the substrate, facing vertically downwards onto the evaporating drop. A schematic of the experimental setup is shown in Figure 4.1.

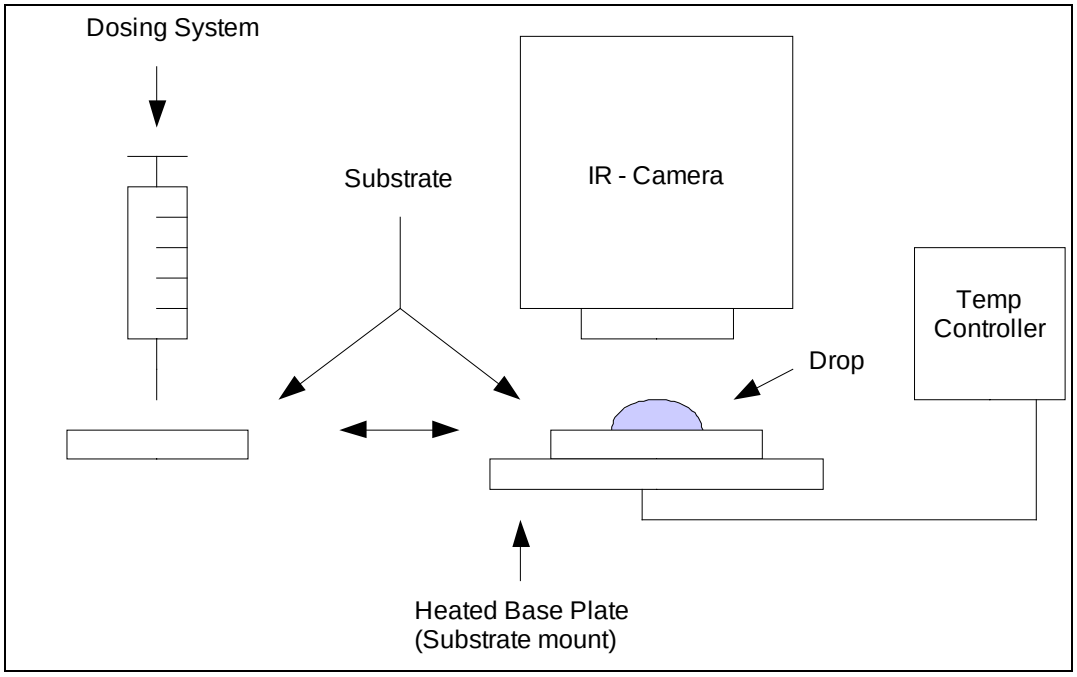

Figure 4. 1. Schematic depicting the experimental setup.

Drops were deposited onto the substrate and then immediately placed under the camera. The investigated drops have contact lines that remain pinned to the substrate for the majority of the drop lifetime. Hence, basal radius remained essentially constant in time, whilst both the height and drop contact angle decreased in time.

4.3.1.1 Calibration.

The Infrared camera used in this experiment was supplied by the EPSRC instrument loan pool, which is a facility providing research instruments available for short-term (1-3 months) loan to research grant and studentship holders. Calibration of the system is conducted by the EPSRC prior to each delivery.

4.3.2 Software

Accompanying software (Thermacam Researcher Pro 2.8) is supplied with the camera which is used for image capture and analysis. The software has many useful features such as real time IR video and data analysis, high speed digital IR data acquisition, automatic temperature vs. time plotting, and simple data exporting mechanisms.

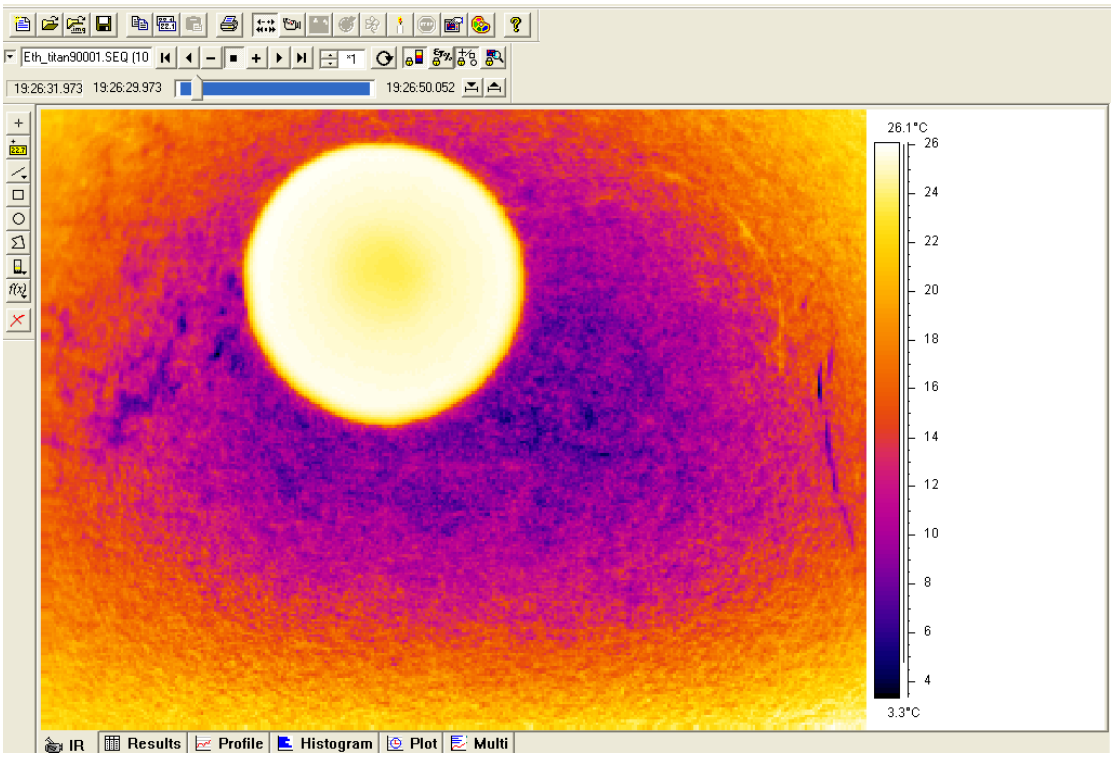

Figure 4. 2. Software interface for data acquisition and analysis.

4.4 Results

4.4.1 Comparison of liquids

Tests were conducted for four liquids. Initial tests for the case of small water drops (r =1.5mm) show that the thermal activity is very weak, with the temperature remaining approximately uniform spatially. This work is supported by the work of Girard et al. [85]. who showed that the magnitude of the temperature gradients that accompany the evaporation of water droplets to be small. An image depicting the behaviour of water is shown in Figure 4.3.

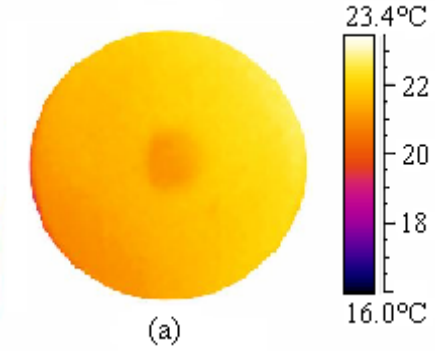

Figure 4. 3. Thermal activity observed from an evaporating water droplet. Typical base radius, r ≈ 1.5mm

As can be seen from the image, there is very little thermal activity observed in the water image the temperature profile at the drop centre differs very little from that at the drop periphery.

In contrast, the results obtained for the other liquids tested were more interesting. Methanol and ethanol appeared to show distinct thermal fluctuations which were observed to vary temporally. These spoke like wave trains were found to travel around the drop periphery. The number of waves observed and the respective travelling velocities of the waves were found vary depending on the substrate which was being used. Thermal images depicting an ethanol and methanol drop are given in Figure 4.4.

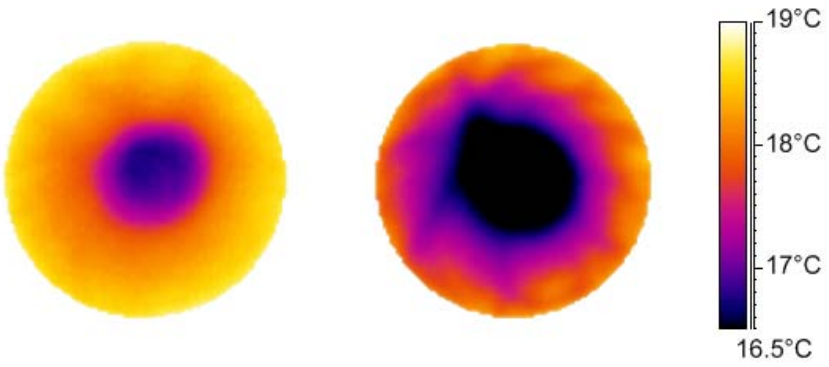

Figure 4. 4. Infra-red image depicting thermal behaviour of Ethanol and Methanol drops evaporating on a ceramic (MACOR) substrate at atmospheric temperature.

From Figure 4.4 it can be seen that there is more distinct thermal activity present in the more volatile methanol droplet. Faint thermal waves are observed in the ethanol droplet, the behaviour of these waves is more easily observed in video format. The waves are more pronounced in the methanol droplet and are characterised alternating warm and warm/cool regions, which travel in the azimuthal direction. These patterns are reminiscent of HTWs observed in thin annular pools of silicon oil subjected to differential heating. No preferred direction of propagation of these waves was observed: both clockwise and anti-clockwise propagation was recorded; in certain cases, the waves appeared to emanate from a source on the drop surface.

Taking drops of similar sizes of ethanol and methanol, it is possible to directly compare the evaporative behaviour. This is shown in Figure 4.5. The images represent the observed thermal activity at distinct intervals in the evaporation process, with τ = 1 representing the end of a particular run.

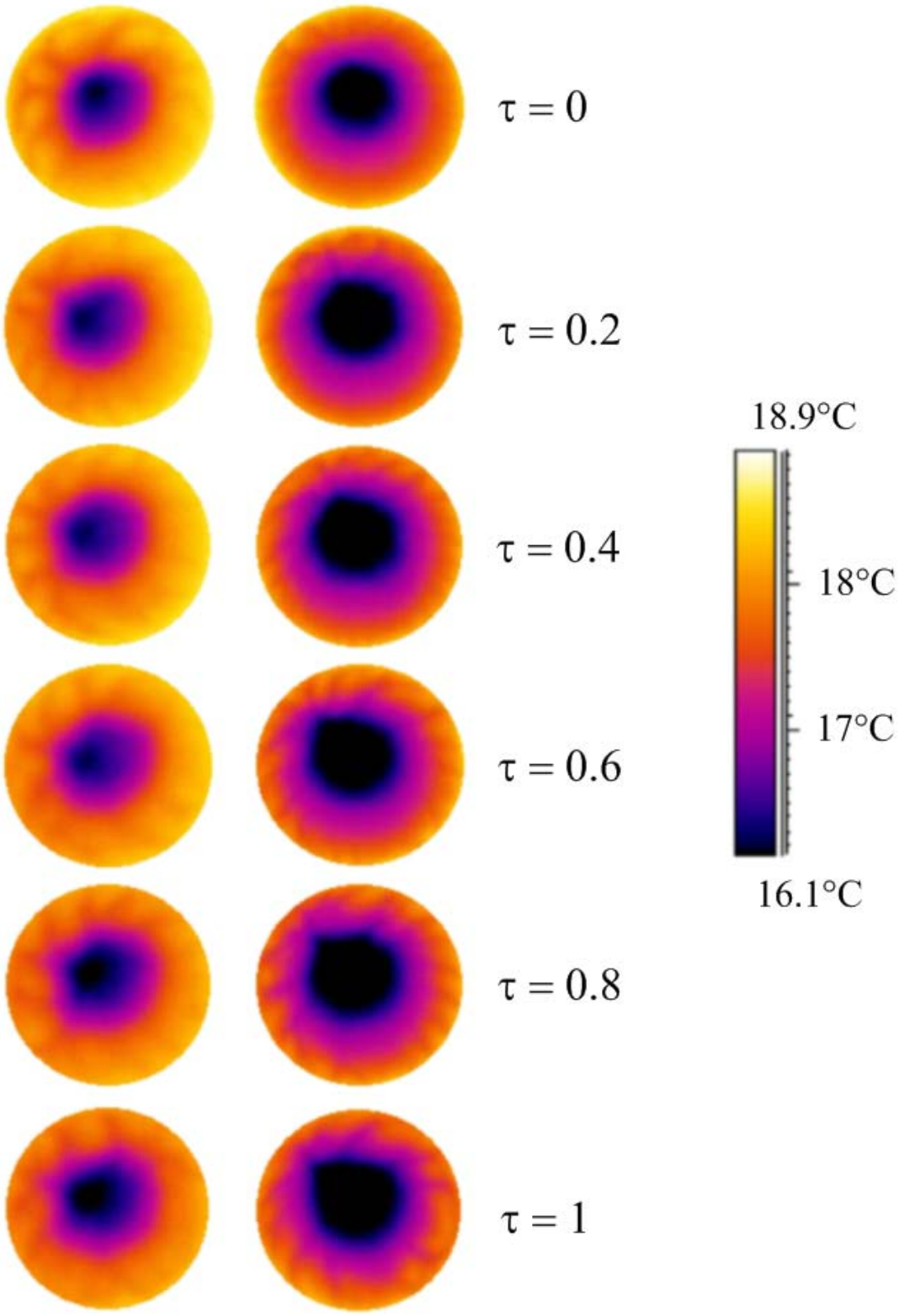

Figure 4. 5. Direct comparison between the evaporative behaviour of ethanol (left hand column) and methanol (right hand column) evaporating on a ceramic substrate at room temperature.

As can be seen from Figure 4.5, there is an appreciable difference in the evaporative behaviour of the two liquids. Although they both possess spoke-like wave patterns,

there appears to be greater thermal activity and more pronounced waves in the methanol drop. The recording period for obtaining these results was 20 seconds, and each image represents a still frame taken as a fraction of the whole recording period. As a result the first and last frames correspond to the initial and final recorded frames (t = 0 and t = 20s) and have values of $\tau = 0$ and $\tau = 1$ respectively. It is clear that there is increased thermal activity present in the more volatile methanol droplet. In addition to possessing more waves than its less volatile counterpart, waves observed in methanol appear to possess a greater travelling velocity along the drop periphery. As evaporation proceeds, it can be seen that the number of waves present in the Methanol drop decreases, whilst the magnitude of the fluctuations appears to increase. This is less clear in the Ethanol droplet due to the fact that there is less activity present.

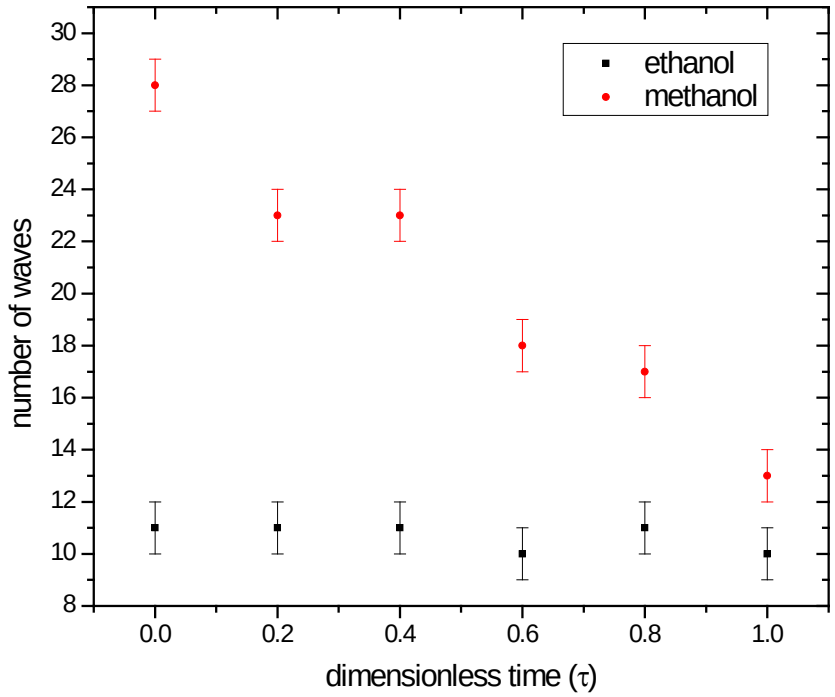

Figure 4. 6. Visible waves as a function of time for methanol and ethanol drops evaporating on a ceramic tile at room temperature.

Figure 4.6 attempts to indicate graphically the temporal change in thermal fluctuations present in the drops depicted in Figure 4.5. The number of visible waves present was

determined by optical measurement using the thermacam software. Errors were included to account for difficulties in observation due to relatively weak behaviour in the case of ethanol, and due to the close proximity of the waves in the case of methanol, this was more problematic in the initial stages of the evaporative lifetime. An example of the numerical determination is shown in Figure 4.7.

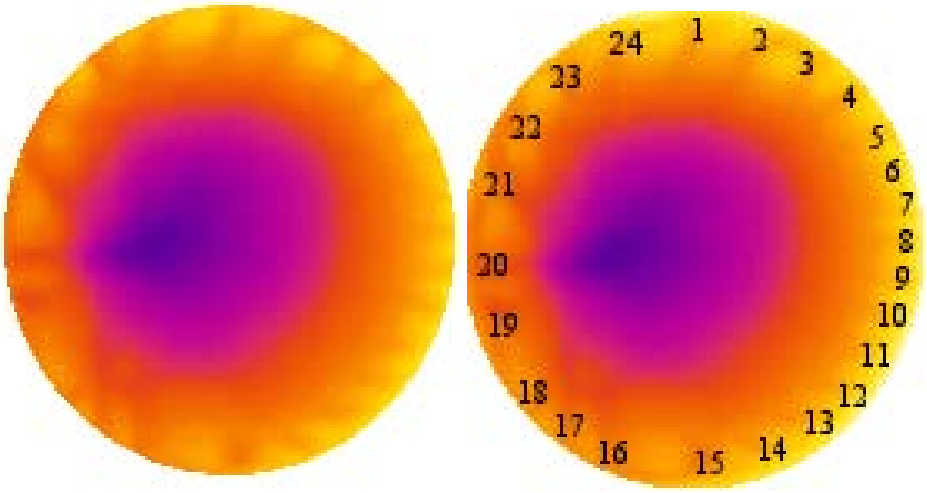

Figure 4. 7. Typical wave train pattern shown by a methanol drop evaporating on a ceramic substrate (at 24°C). An attempt has been made to number the individual waves present.

In addition to the interesting behaviour of ethanol and methanol, results were also obtained for the refrigerant FC-72. Thermal imaging of the FC-72 drops shows a distinct evaporative behaviour which is very different from those observed for the alcohols. In the case of FC-72, no spoke like waves are observed. Instead, thermally-driven cells rather than HTWs were observed emerging near the drop centre and drifting towards the edge. The cells were larger near the drop apex than in the vicinity of the contact line, see Figure 4.8. During the evaporative process these cells were shown to propagate more or less perpendicularly to the drop contact line. The cells appear large as they first emerge, and are then reduced in size as they propagate and new cells emerge behind them. Figure 4.9 shows the evolution of the patterns at various stages of the lifetime of the drop evaporating on a titanium substrate. It can be seen clearly in Figure 4.9(a) that, at early times, the drop develops a relatively cool region near its apex. The average interfacial temperature increases radially and exhibits a maximum near the drop edge.

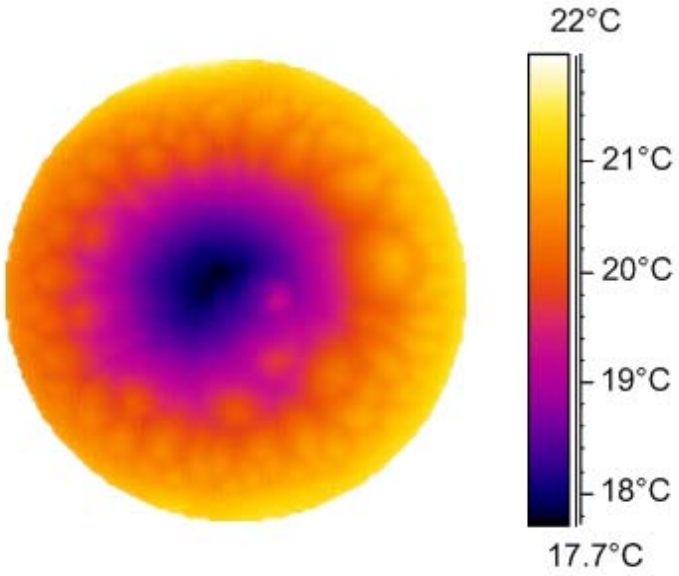

Figure 4. 8. Infra-red image depicting the thermal behaviour of an FC-72 drop evaporating on a ceramic (MACOR) substrate at room temperature.

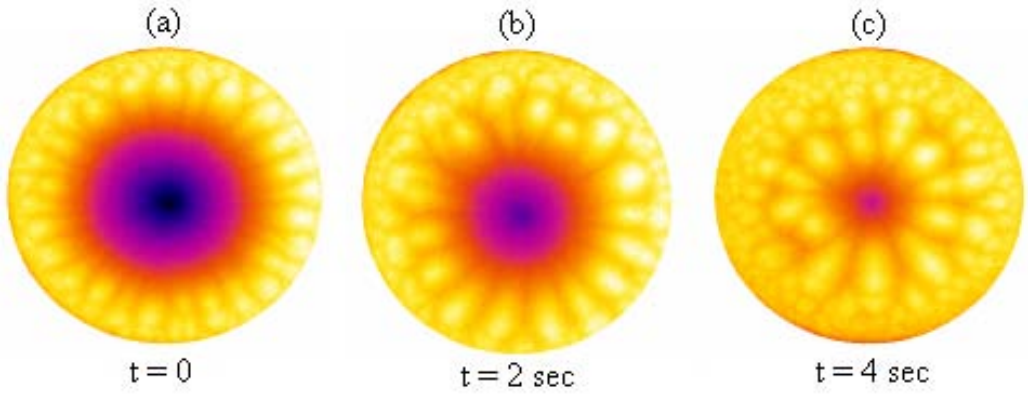

Figure 4. 9. Evolution of the patterns observed during the evaporation of a FC-72 drop on a Titanium substrate. The time interval separating consecutive snapshots in (a)-(c) is 2 seconds.

During the course of the evaporation process, the minimal temperature at the apex and the extent of the cool region are reduced and the overall temperature gradient between the apex and the drop edge decreases (see Figure 4.9(b), (c)). It is also seen in Figure 4.9 that the cells, which are evident at early times, appear to extend from the flow origin to the region immediately upstream of the contact line (see Figure 4.9(a)); in the region nearest the contact line, cells of smaller dimension are discernible. With increasing time and decreasing drop height, the extent of the region populated by the

larger cells decreases and appears to become increasingly confined to the centre of the drop; the region occupied by the smaller cells, on the other hand, increases substantially. It is important to note that, in contrast to the ethanol and methanol drops, the patterns observed in the case of FC-72 drops do not correspond to propagating waves.

4.4.2 Comparison of Substrate Material

Four separate substrates were selected for these experiments; they were selected to provide a wide range of thermal conductivity values. As previously stated these substrates were:

- PTFE (polytetrafluoroethene), a common polymer used in many wide ranging applications such as in non-stick frying pans or as insulating material.
- MACOR, a glass-ceramic which is used in a wide range of industries such as in aerospace and nuclear engineering. It displays good thermal properties and exhibits excellent temperature stability.
- Titanium, a strong, low density metal used in numerous industrial areas.
- Copper, a very high thermal conductivity metal which has many applications in industry.

In order to ensure that the wettabilities of each surface were uniform, a thin coating of a hydrophobic fluoropolymer material was applied to each substrate. The material chosen was CYTOP, which displays a strong chemical resistance and high optical transparency. The coating itself was implemented using a spin coating technique which enabled a very thin layer of material to be applied to each surface. It was important to make sure that the layer was kept as thin as possible to ensure that the thermal conductivity of the surface was not hindered.

Initial tests for each liquid were conducted on the least conductive substrate, PTFE. From the infrared videos obtained for methanol, ethanol and FC-72, parameters such as number of wave like spokes and/or cells, spoke/cell velocity and temperature gradients were obtained.

Ethanol

Results are presented in Figure 4.10 which show the typical evaporative behaviour observed when ethanol evaporates on the four selected substrates at room temperature. The temperature in the lab was observed to fluctuate between 18° and 23°, care was taken to ensure that tests were conducted when the working temperature in the lab was at around 20°C. The results show the variation of evaporative behaviour between the different substrates. On the least conductive substrate, PTFE, the thermal fluctuations observed in the droplet are very slight, and are difficult to accurately visually observe. As we progress towards to the cases of the MACOR and Titanium substrate we begin to see more defined thermal wave patterns. It appears that on more conductive substrates the number of visible waves tends to increase. The result observed on the most conductive substrate, copper, appears to support this observation. In addition, it is shown that the number of waves appears to decrease as time progresses.

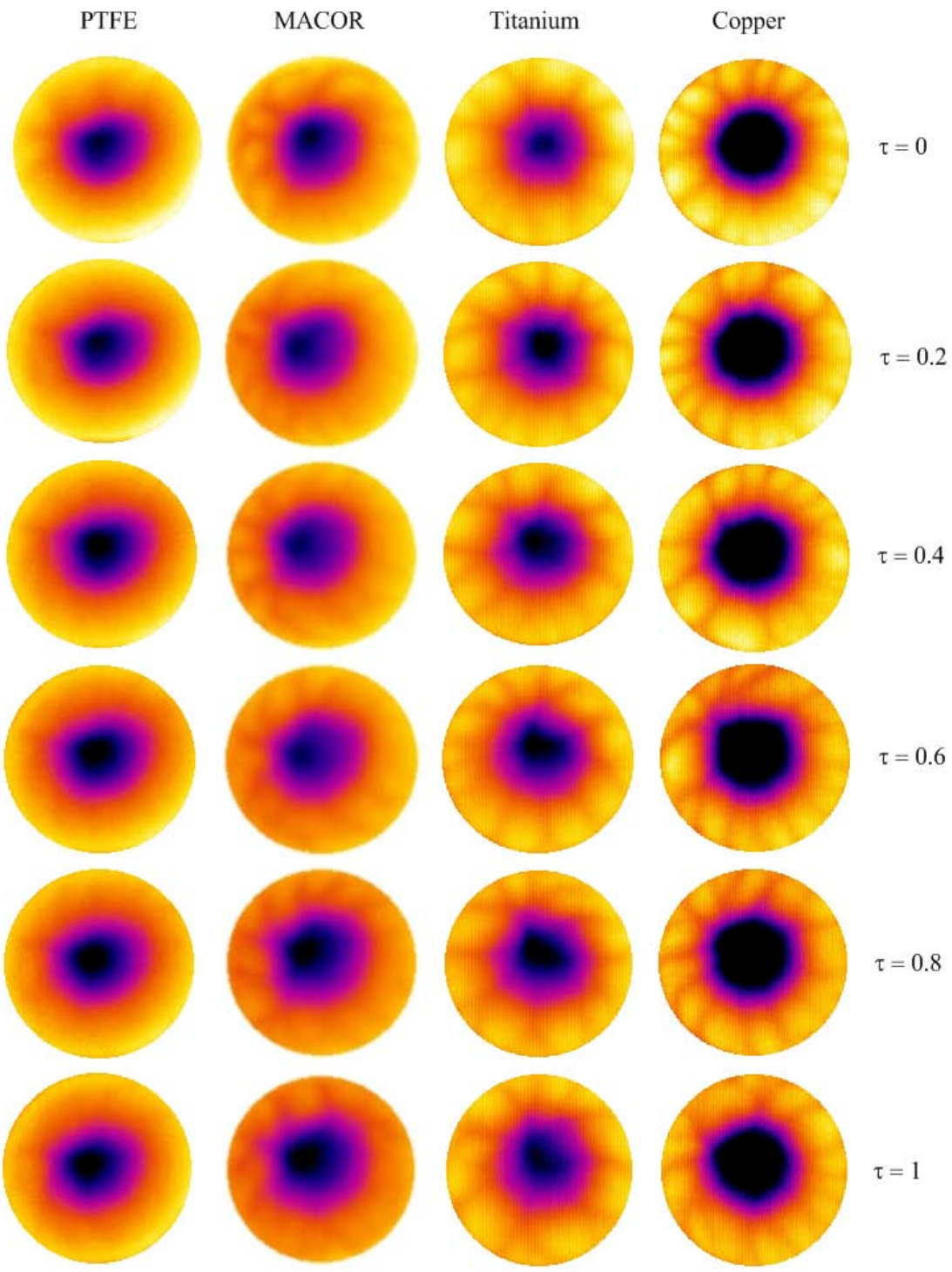

Figure 4. 10. Ethanol drops on four substrates are depicted with images showing the thermal behaviour observed at specific intervals during evaporation.

Figure 4.11 displays a graph of the number of waves present as a function of time for the ceramic substrate and the most conductive copper surface to give a comparison.

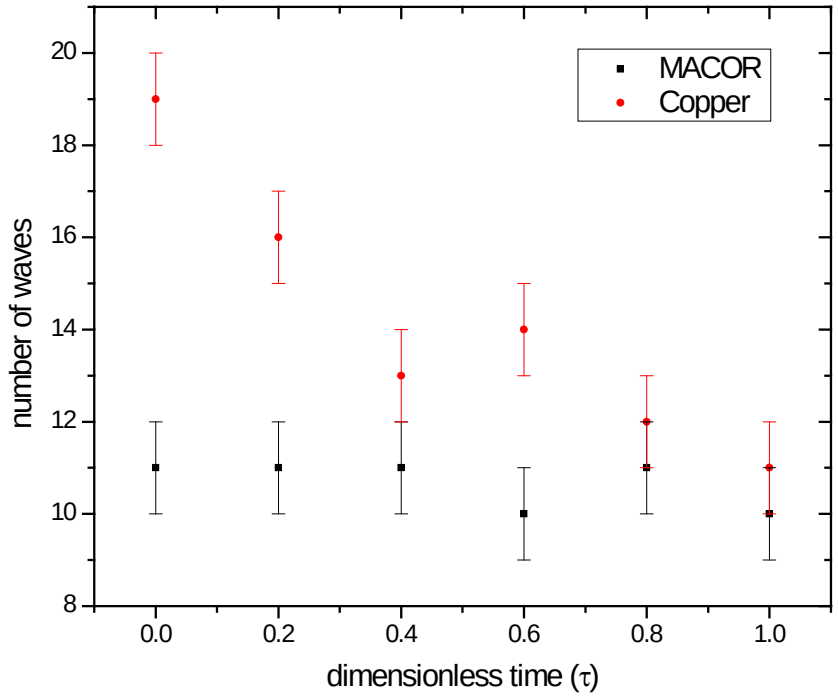

Figure 4. 11. Visible waves as a function of time for ethanol drops evaporating on a ceramic substrate (MACOR) and copper at room temperature.

The similarities between Figures 4.6 and 4.11 indicate that increased thermal activity (the presence of more waves) can be observed by selecting a substrate material of higher conductivity or by selecting a liquid which is more volatile. Thus, a more volatile liquid which evaporates on a conductive surface should possess many waves.

Methanol

Methanol was tested on the same four substrates, and the results were analysed in the same manner. The results obtained are depicted in Figure 4.12. The thermal activity present in methanol is clearly more vigorous than in ethanol at the same temperature. At an early stage of evaporation the methanol tests often seem to possess vigorous thermal behaviour in which thermal waves cannot easily be determined, these seem to ‘emerge’ as the drop evaporates. The pictorial results shown for methanol are less clear than those of ethanol; this is due to the vigour with which the thermal activity is taking place. Direct comparison between Figure 4.10 and 4.12 shows the enhanced thermal activity that is present in methanol drops. A graph illustrating the effect of substrate conductivity on the number of visible waves in an evaporating methanol drop is given in Figure 4.13.

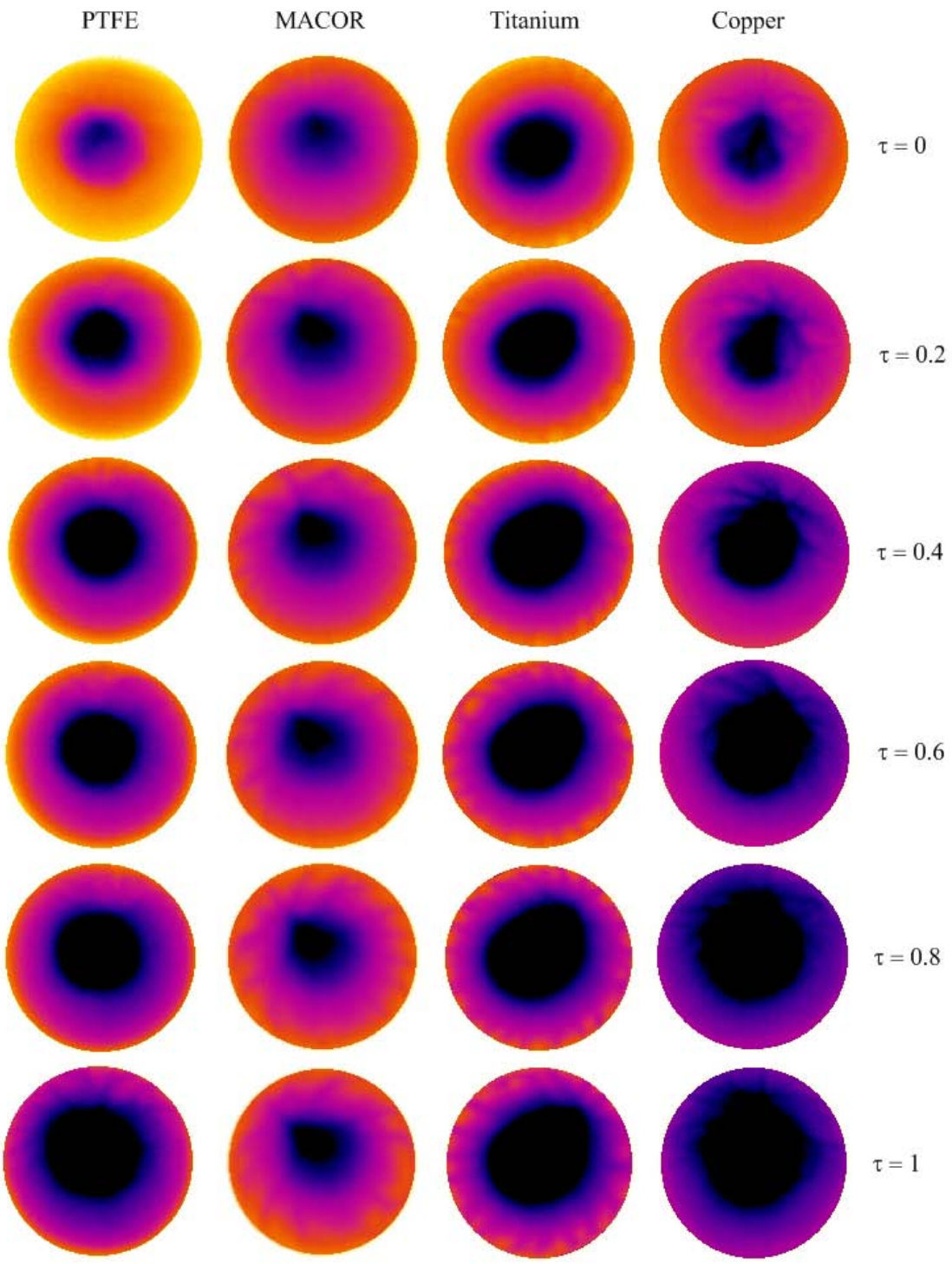

Figure 4. 12. Methanol drops on four substrates are depicted with images showing the thermal behaviour observed at specific intervals during evaporation.

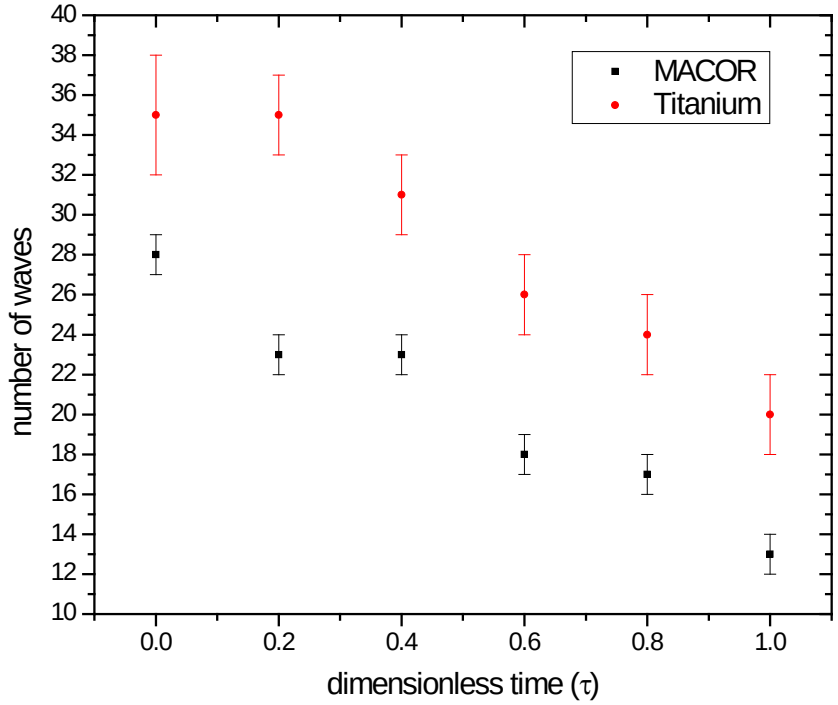

Figure 4. 13. Visible waves as a function of dimensionless time for methanol drops evaporating on a ceramic substrate (MACOR) and titanium at room temperature.

As can be seen from the graph, methanol also possesses a decreasing number of waves as time progresses. There are also more waves observed on the more conductive titanium substrate. The larger error bars at early stages are due to the difficulty in observing the frantic behaviour occurring at these times. It can be seen that an increased number of HTWs can be observed by either selecting a substrate of higher conductivity or by switching from ethanol to the more volatile methanol liquid.

FC-72

As has been discussed previously FC-72 appears to possess very different thermal activity to that of the alcohols ethanol and methanol. Results are presented depicting the evaporation of FC-72 on the four different test substrates in Figure 4.14. As can be seen in the figure, results for FC-72 show cells which propagate from the drop centre

out towards the contact line in each case. Each experiment was repeated at least 5 times to ensure repeatability.

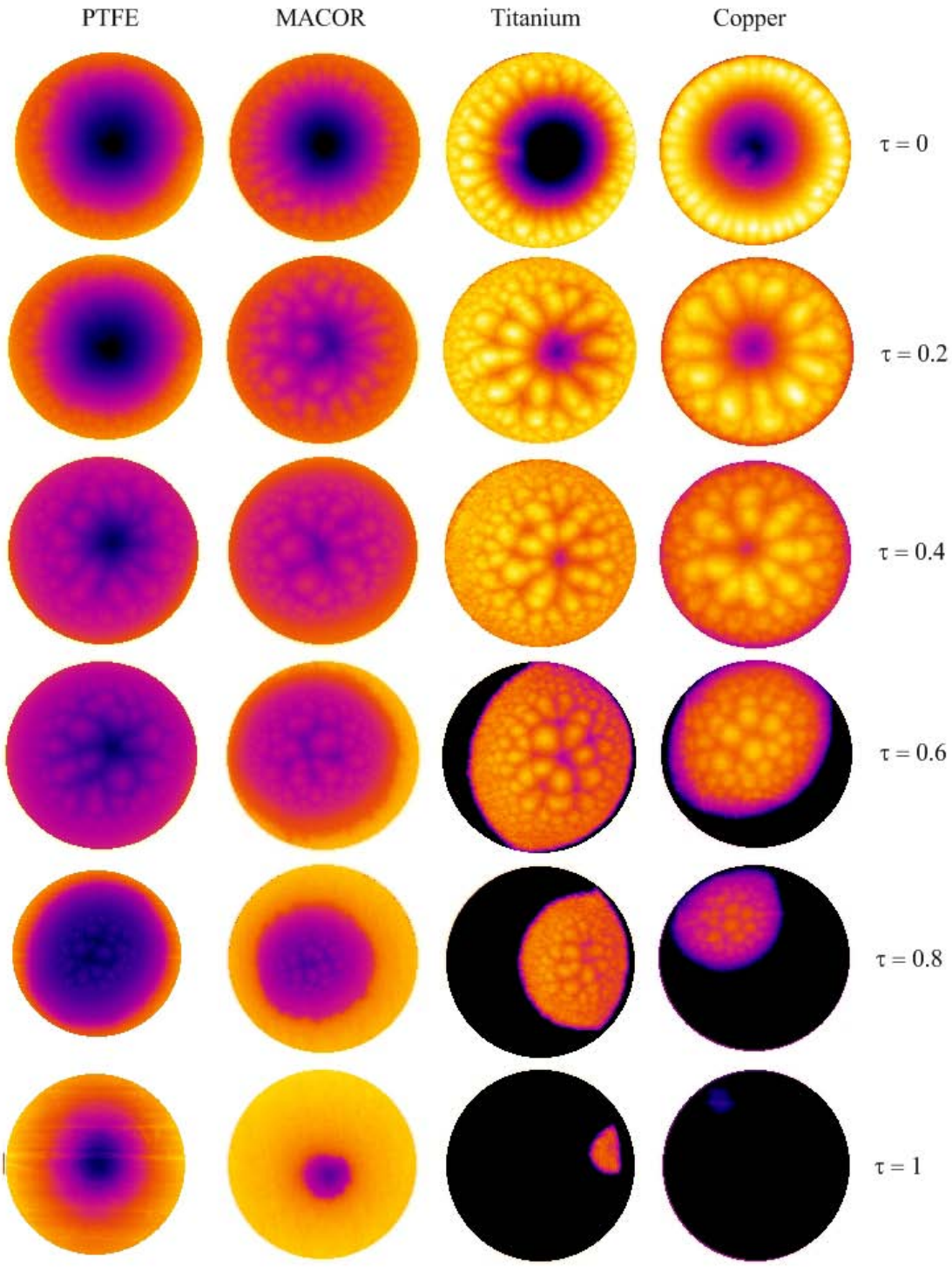

Figure 4. 14. FC-72 drops on four substrates are depicted with images showing the thermal behaviour observed at specific intervals during evaporation.

4.4.3 Comparison of Substrate Temperature

The effect of substrate temperature was investigated by constructing a substrate mount which was capable of heating the substrate to a desired temperature. The substrate temperature was controlled via a temperature controller whilst the temperature readings were obtained from a thermocouple which was embedded in the substrate mount. Initial recordings were taken at temperatures of 26°C & 29°C, and later some additional results were obtained for 24° & 32°C for the cases of methanol and FC-72.

Care was taken to ensure that there was good thermal contact between the heated plate and the test substrate in each case. This was done by affixing the substrate to the heated plate with the use of a thermally conducting contacting adhesive. Before testing, care was taken to ensure that the substrates were at the required temperature, and that the temperature was being controlled adequately. This was more of a concern when testing the thermally insulating PTFE and MACOR substrates. However, the thicknesses of the substrates were relatively thin, and the substrates were found to heat up to the required temperature in a few minutes. The results of increasing the temperature for methanol and ethanol are given below.

Ethanol

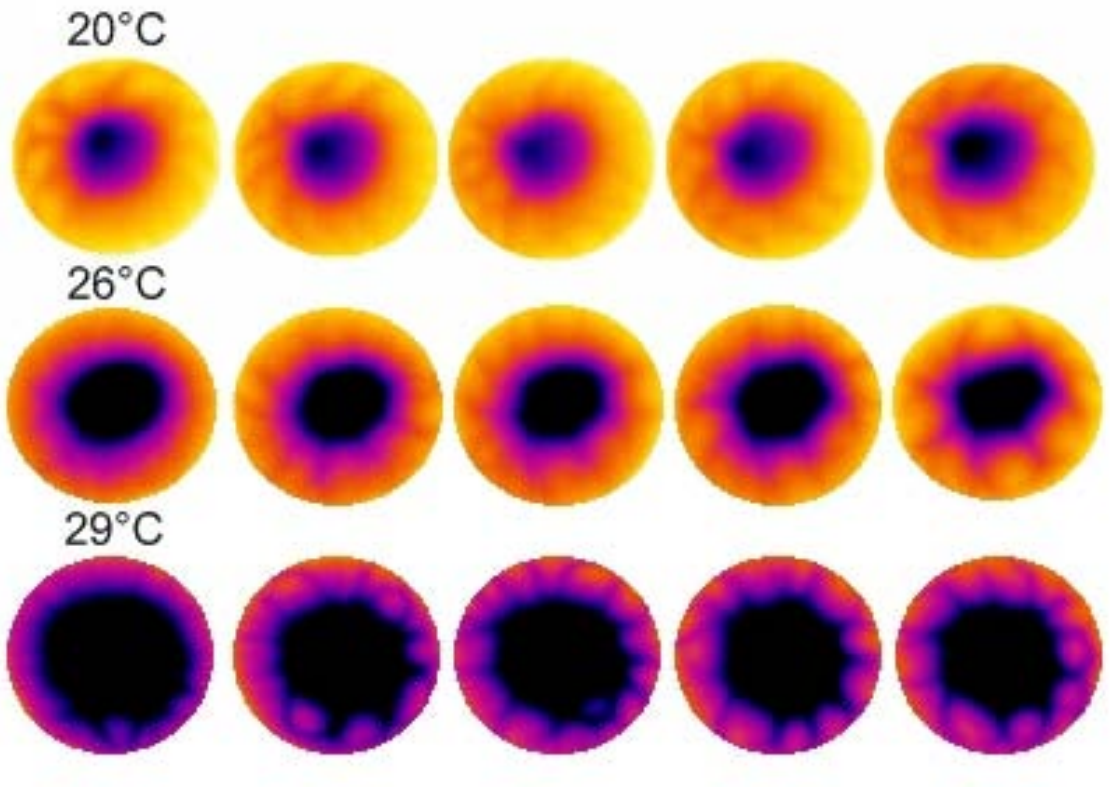

Figure 4. 15. The evaporative behaviour of an ethanol drop evaporating on a ceramic substrate at 20°C, 26°C, and 29°C.

From Figure 4.15 we can see a slight increase in thermal activity as the temperature increases. The HTWs appear to be more clearly defined, showing a slightly increased temperature difference between warm and cool regions. The increase in thermal activity has been plotted in Figure 4.16. The narrow range of temperature reading means that in order to display all three samples at the given temperatures, some trade off is necessary in range of interest.

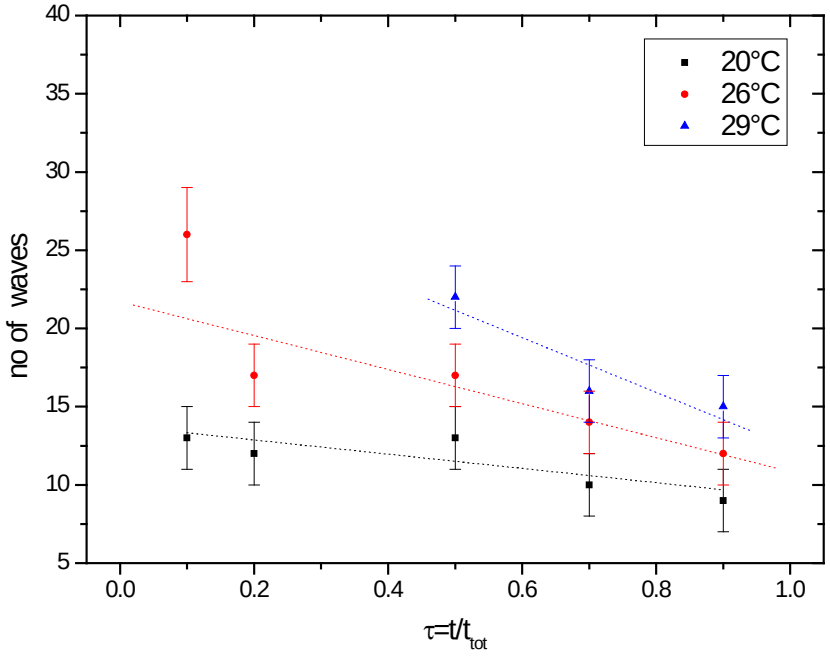

Figure 4. 16. Graphical representation showing the variation in number of visible waves as time progresses for ethanol drops evaporating on substrates held at 20°C, 26°, and 29°C respectively.

In Figure 4.16 the reduction in number of visible waves as a function of time is evident. The number of visible waves is still clearly less than that which is observed in evaporating methanol drops owing to the less thermal activity present in ethanol.

Methanol

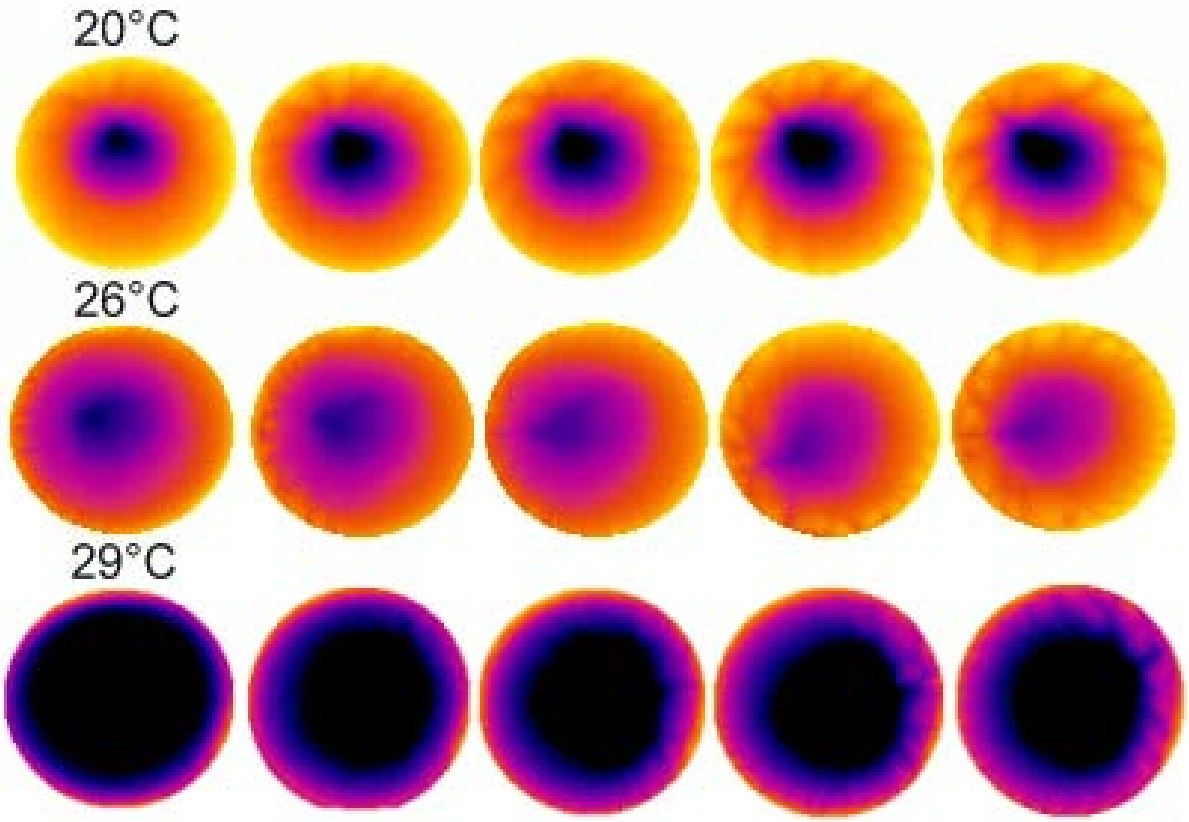

Figure 4. 17. The evaporative behaviour of a methanol drop evaporating on a ceramic substrate at 20°C, 26°C, and 29°C.

The increase in visible waves as substrate temperature increases is more pronounced in the case of methanol. Also direct comparison between Figures 4.15 and 4.17 help to illustrate the increased thermal activity shown by methanol. A graph illustrating the change in visible waves against evaporation time is depicted in Figure 4.18.

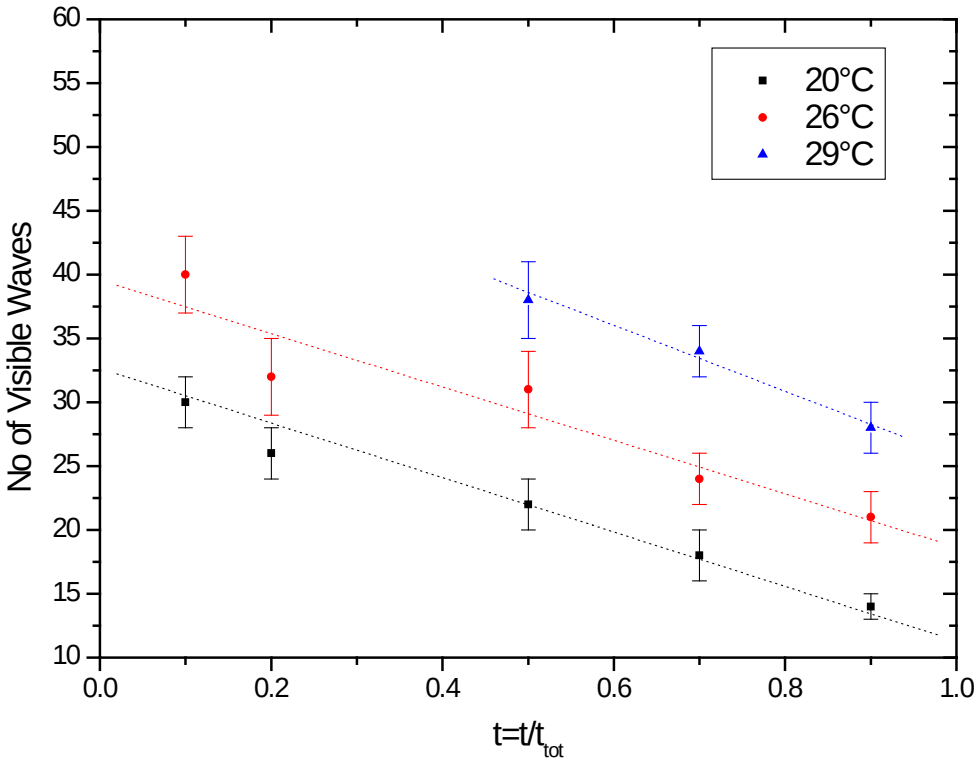

Figure 4. 18. Graph depicting the change in visible waves as evaporation proceeds for a methanol drop on a ceramic substrate at various temperatures.

In this figure the change in visible waves is clear to see. It is shown that at all temperatures the methanol follows the general trend of decreasing waves in time, much like the ethanol drops. There are more waves present for methanol however, and the trend is clearer to see than for ethanol. Figure 4.19 depicts the evaporative behaviour for both methanol and ethanol on titanium substrates at different temperatures and is provides a good comparison of the differing behaviour.

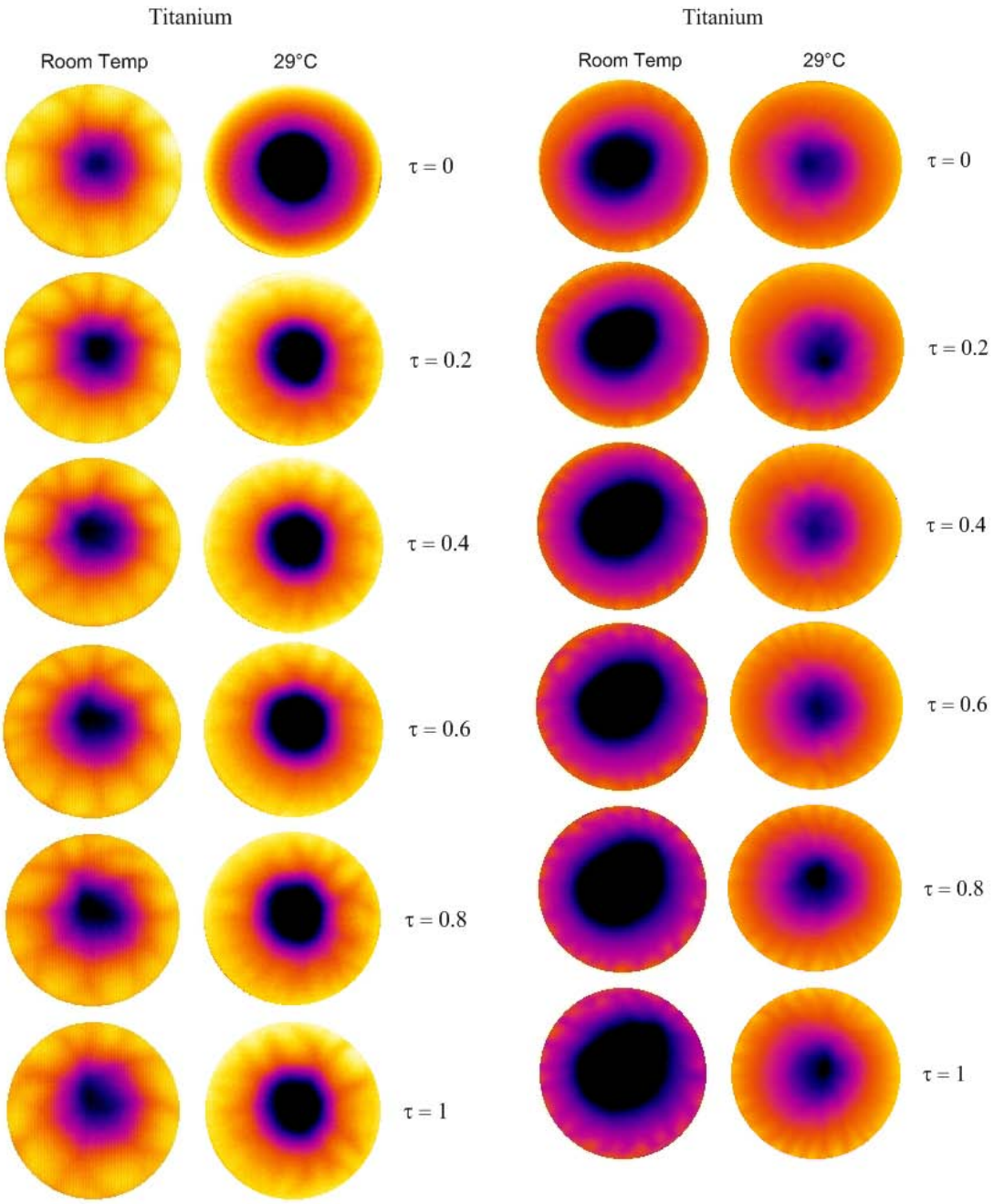

Figure 4. 19. Comparison of ethanol (left hand column) and methanol (right hand column) drops evaporating on a titanium substrate, at room temperature and 29°C. More waves are observed in the case of the substrate with the higher temperature and more volatile liquid.

4.5 Discussion

The interesting results presented here are very similar in nature to the work by Garnier et al. [86, 87], who studied thermocapillary-driven patterns in shallow annular pools of silicon. Garnier et al. correlate their results by estimating the values of the Marangoni, Rayleigh and Bond numbers, given by *Ma*, *Ra* and *Bo*. Estimates of these numbers have been made in table 4.3 for the three liquids methanol, ethanol, and FC-72. Here, T denotes the temperature, H and l are characteristic vertical and radial length scales, ρ, υ and κ are the density, kinematic viscosity and thermal diffusivity respectively; g is the gravitational acceleration, σ is the surface tension; $\alpha = (1/\rho)(\partial\rho/\partial T)$ is the coefficient of thermal expansion and $\gamma = -(\partial\sigma/\partial T)$, a positive quantity for most pure fluids. It is also useful to define χ: for $\chi << 1$ one would expect to observe thermocapillary-driven waves and then beyond a threshold to observe rolls.

	Methanol	**Ethanol**	**FC-72**
$M = \gamma H^2 \Delta T / \rho \nu \kappa$	8.7×10^{2}	3.6×10^{3}	4.9×10^{2}
$Ra = \alpha g H^4 \Delta T / \nu \kappa$	58.6	16.8	10.2
$\chi = Ra / Ma$	6.7×10^{-2}	4.7×10^{-3}	2.1×10^{-2}
$Bo = \rho g H^2 / \sigma$	0.16	0.13	0.11

Table 4.3: Estimates of dimensionless parameters.

For the test liquids average values were selected for ΔT, H, and l with the height and length scales obtained using a contact angle analyser which can also be used to obtain drop heights and base diameters. In the case of both ethanol and methanol $\chi << 1$ indicating that thermocapillary forces do indeed dominate those related to buoyancy. Thus, for these liquids the dynamics should be accompanied by the formation of thermocapillary-driven patterns such as the HTWs observed by Garnier et al [87]. The small values obtained for Bo also indicate that surface tension should dominate and that gravitational forces are expected to play a relatively minor role. It is also shown from Table 4.3 that thermocapillary forces should be dominant in the case of FC-72, however the patterns observed seem to indicate a rolling pattern.

The magnitude of the temperature gradients that accompany the evaporation of a sessile drop decreases with increasing time and decreasing drop thickness. As a result the driving force for the formation of HTWs is reduced leading to a reduction in the number of visible waves as evaporation proceeds.

It is important to note that in contrast with the work of Garnier et al, as well as in other cases in which thermally-induced waves result from the imposition of constant temperature gradients, the gradients in the case of evaporating sessile drops are self-generated due to the spatially non-uniform evaporative flux. Furthermore, the conditions of criticality are now both spatially and temporally-varying due to the evolving drop height and temperature gradients; these features are absent in the case of differentially heated pools.

The angle of propagation of the thermally-induced wave-trains, which measures the deviation of the axis of an individual wave from the radial direction, was also measured for methanol and ethanol. Previous work has shown this quantity to be strongly dependent on the Prandtl number, $Pr = C_p\mu/\lambda$, for HTWs ; here, Cp, μ, and λ denote the specific heat capacity, dynamic viscosity and thermal conductivity, respectively. Our results indicate that the propagation angles for methanol and ethanol (Pr = 6.4 and 12, respectively) are 11° and 20° for PTFE, 14° and 25° for Macor, and 19° and 28° for titanium, respectively. This finding is in line with the results of previous work on differentially heated thin liquid pools, which showed that the propagation angle increases with Pr. Moreover, it appears that substrates of larger thermal conductivity, which lead to larger evaporation rates, also give rise to higher propagation angle.

4.6 Conclusion

In summary, the spontaneous evaporation of sessile drops of varying volatility on substrates with a wide range of thermal conductivity using IR thermography has been studied; attention was focused on the thermally-induced dynamics that accompanies

the evaporative process. Experimental evidence for the presence of interfacial temperature wave-trains has been presented, which, in the case of methanol and ethanol, are identified with the HTWs observed previously in the literature; the dependence of the wave-train characteristics on system parameters provides strong supporting evidence allowing us to identify these waves as HTWs. Previous studies have observed HTWs resulting from the imposition of temperature gradients. However, the driving force for the wave-trains in the volatile sessile drops investigated here are self generated temperature gradients resulting from non-uniform evaporation. The magnitude of these spontaneously-formed gradients and the drop thickness decrease with time and these, along with the substrate thermal properties were shown to influence the observed pattern characteristics.

5. Theoretical Model

5.1 Objective

A theoretical study was conducted by researchers from Marseille Université using the experimental findings from the previous chapter as a basis on which to build the theory. The main aim was to try and provide an insight into the observed behaviour from a theoretical perspective. The purpose of this theoretical analysis is to track the threshold of the onset of HTWs by means of a linear hydrodynamic stability analysis. Only the main results are presented in this section, a rigorous description of the theory has been published and can be found in Colloids and Surfaces A: Physicochemical and Engineering Aspects, **365**, 1-3, 95-108, 2010. This approach focuses on droplets under atmospheric pressure. The droplets under investigation are millimetre in size and hence have spherical cap geometry as a result of the negligible effect of gravity. The analysis is restricted to pinned drops i.e. drops with a constant contact line radius r_d. Evaporation takes place as a result of the unsaturated vapour in the surrounding atmosphere. At the free surface, the vapour concentration is assumed to be the saturation concentration, in the vapour phase a steady diffusive regime sets in from the saturated layer to the unsaturated region. No natural convection is expected for substances heavier than air (methanol and ethanol for example). In the reference state, the two phases are at a mechanical equilibrium and isothermal. The perturbation equations have to be written in 3D as azimuthal motion is expected to set in. Trial functions are introduced to the theory to produce behaviour similar to that which was observed experimentally. The results are speculative, but give an indication towards a direction for future theoretical investigation.

5.2 Perturbation equations

The following equations are taken from the paper in which the theoretical work is published, they are presented here to show how the trial perturbations were constructed.

The velocity - temperature and vapour mol-fraction perturbed fields are expressed in terms of spherical harmonics.

$$\begin{aligned}
&\frac{\partial \vec{v}'}{\partial t} + \left(\vec{v}'.\vec{\nabla}\right)\vec{v}' = -\frac{1}{\rho}\vec{\nabla}P' - 2\vec{\Omega}\times\vec{v}' + \nu\vec{\nabla}^2\vec{v}' \\
&\vec{v}' = \vec{v}^* + \delta\vec{v} \\
&P' = P^* + \delta P \\
&\delta\vec{v} = V(R)Y_1^m(\theta,\phi)\exp(\omega\tau)
\end{aligned} \tag{5.1}$$

$$\begin{aligned}
&\frac{\partial T'}{\partial t} + \vec{v}\cdot\vec{\nabla}T' = \nabla^2 T' - \vec{v}\cdot\vec{\nabla}T^* \\
&T' = T^* + \delta T \\
&\delta T = \Im(R)Y_l^m(\theta,\phi)\exp(\omega\tau) \\
&\frac{\partial Y'}{\partial t} + \vec{v}\cdot\vec{\nabla}Y' = \nabla^2 Y' - \vec{v}\cdot\vec{\nabla}Y^* \\
&\partial Y' = Y^* + \delta Y
\end{aligned} \tag{5.2}$$

The momentum boundary conditions on the free surface have to account for the normal deformation of the drop. The evaporation front curvature has to be perturbed in the same way as done by Blinova et al. [97] for a spherical solidification front.

The reference state is a time dependent state with a characteristic time given by $\frac{\theta_c^o}{\Omega}$.

The perturbations have a time constant $\frac{1}{\omega} << \frac{\theta}{\Omega}$. The stability analysis has to be performed for asymptotic conditions at short time and short wavelengths. Exchange of stability or oscillatory instability might be obtained according to the values of the real or imaginary parts of ω. The analytical resolution of the eigen-values problem should lead to knowledge of the minimum critical value of the Marangoni number and evaporation number at which the most probable mode of deformation of the surface

should grow. The short wavelength modes growing on the receding spherical cap may be described by polynomial developments. The most classical ones are the Legendre polynomials. With various trial functions to model the perturbations of the drop surface, structures similar to the thermographic images are obtained. In Figure 5.1, the patterns obtained on sessile drops with various contact angle show clearly that the wavelength increases with decreasing contact angle as obtained by thermography.

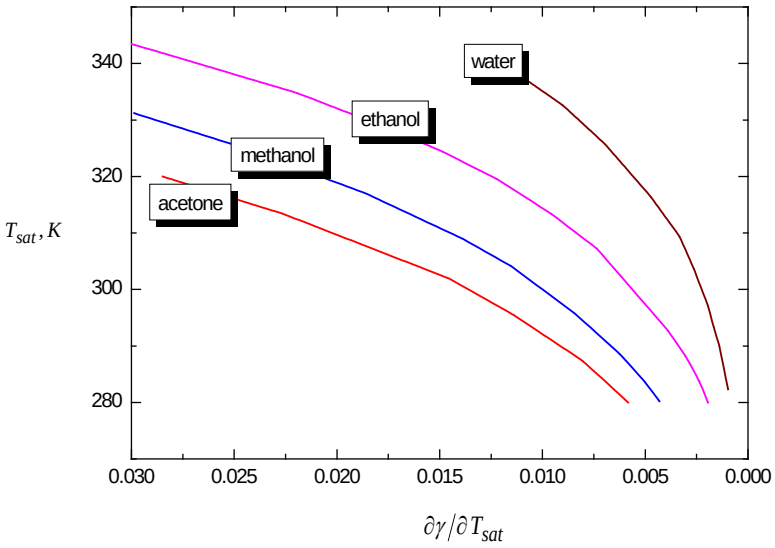

Figure 5. 1. Vapour saturation fraction-Temperature slopes; acetone, methanol, ethanol and water.

According to the trial function used, the pattern obtained on the drop may show a decreasing wavelength when approaching the triple line. A deformation in the azimuthal direction may also be predicted. The normal perturbations of the surface correspond to regions where the vaporization front penetrates in colder or warmer domains removed from the equilibrium conditions so that condensation or evaporation may proceed locally on the crests or in the wells. The surface deformation induces micro-convection in the neighbouring fluid. The problem as formulated so far cannot be solved analytically. Elaborate and tedious numerical techniques are necessary to give a full solution to the problem. Instead of going down that route, a different approach has been adopted, which aims to reveal the nature and form of the perturbations which could lead to surface waves similar to the ones observed experimentally. Using as an initial steady state a drop with a spherical cap shape, a parametric study is undertaken to evaluate the form of the solutions to perturbations

which may give rise to waves similar to the ones observe experimentally. In a first stage a perturbation of the interface is introduced, following the functions given below,

$$x + \delta x = \cos\varphi \cdot \left(\cos[\pi/2 - \theta] + \frac{1}{64}\cos 64[\pi/2 - \theta] \right)$$

$$y + \delta y = \sin\varphi \cdot \left(\cos[\pi/2 - \theta] + \frac{1}{64}\cos 64[\pi/2 - \theta] \right)$$

$$z + \delta z = \left(\sin[\pi/2 - \theta] + \frac{1}{64}\sin 64[\pi/2 - \theta] \right)$$

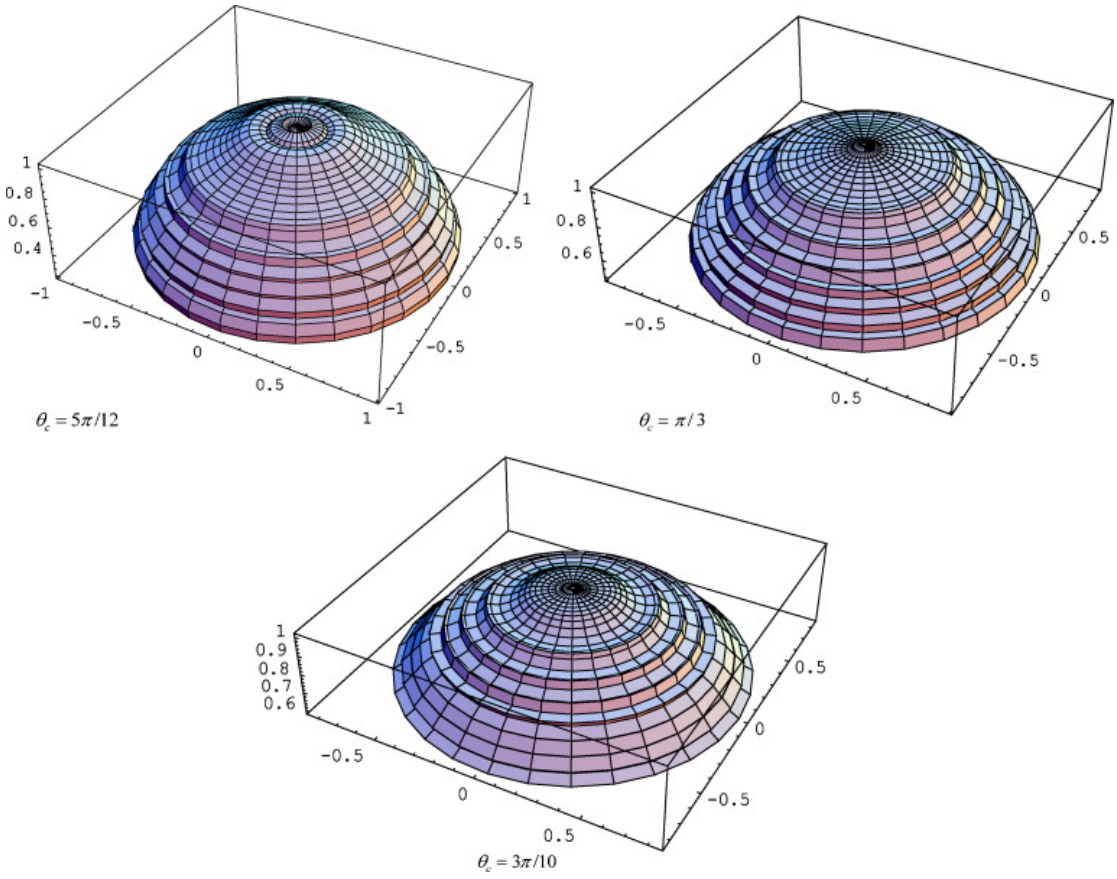

Figure 5. 2. Surface wavy perturbation obtained with arbitrary trial functions.

The resulting waves are of similar wavelength travelling from the apex to the contact line region, Figure 5.2. In a second stage the perturbation functions are altered according to the format given below,

$$x+\delta x=\cos\varphi\cdot\left(\cos\left[\pi/2-\theta\right]+\frac{1}{64}\cos 64\left[\pi/2-\theta\right]^2\right)$$

$$y+\delta y=\cos\varphi\cdot\left(\cos\left[\pi/2-\theta\right]+\frac{1}{64}\cos 64\left[\pi/2-\theta\right]^2\right)$$

$$z+\delta z=\left(\sin\left[\pi/2-\theta\right]+\frac{1}{64}\sin 64\left[\pi/2-\theta\right]^2\right)$$

The resulting waves are still travelling from the apex to the contact line, with the wavelength decreasing as we move from the apex to the contact line. In a last stage, and in addition to the perturbations on the longitudinal angle, a perturbation on the azimuthal angle is introduced. The perturbations functions are selected in such a way that the contact line is not deformed (since we are dealing with pinned drops). This last form of perturbation functions seems to yield waves that are very similar to the ones observed in the experiments. Circling waves, with a wavelength that depends on position are obtained when trying the following functions,

$$x+\delta x=\left\{\cos(\varphi-\left[\pi/2-\theta\right])+\frac{1}{6}\cos 6\varphi\cdot\sin(\theta-\theta_c)\right\}\cdot\left(\cos\left[\pi/2-\theta\right]+\frac{1}{64}\cos 64\left[\pi/2-\theta\right]^2\right)$$

$$y+\delta y=\left\{\sin(\varphi-\left[\pi/2-\theta\right])+\frac{1}{6}\sin 6\varphi\cdot\sin(\theta-\theta_c)\right\}\cdot\left(\cos\left[\pi/2-\theta\right]+\frac{1}{64}\cos 64\left[\pi/2-\theta\right]^2\right)$$

$$z+\delta z=\left(\sin\left[\pi/2-\theta\right]+\frac{1}{64}\cos 64\left[\pi/2-\theta\right]^2\right)$$

In addition to circling waves on the drop surface which replicates the observed experimental trend, the above perturbation functions, and in agreement with experiments, indicate that the wave number decreases as the drop evaporates, Figure 5.3.

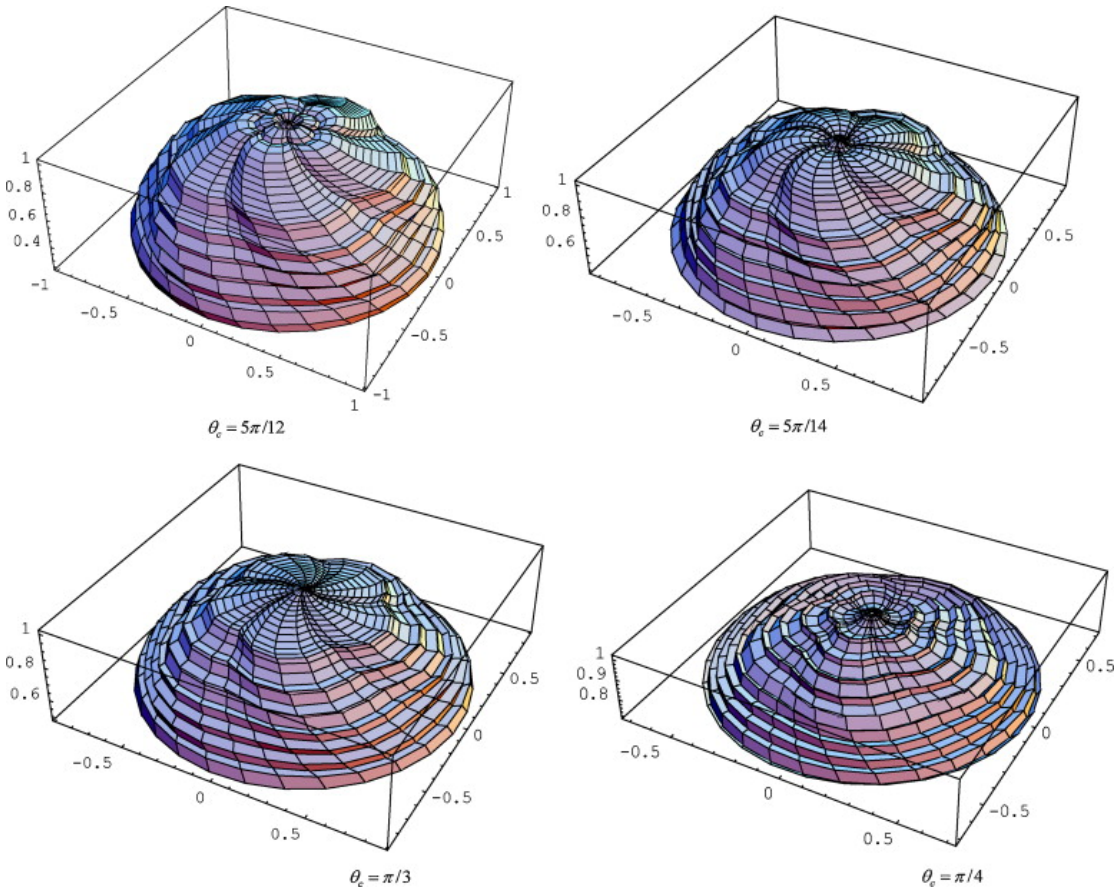

Figure 5. 3. Azimuthal motion obtained with trial functions.

The approach adopted above may be qualitative in nature; nonetheless it unravels very useful information on the form the perturbations may have in order to give rise to waves similar to the ones observed experimentally. This approach also can guide modellers in selecting the right form of perturbation functions, when attempting a more complete theoretical resolution of the problem.

5.3 Conclusion

The complexity of the evaporative process of sessile drops has been investigated by means of IR thermography. The spontaneously occurring thermal instabilities shown by ethanol, methanol and FC-72 are clearly distinct from each other, and can also be manipulated by altering the evaporation parameters such as substrate material and substrate temperature.

Hydrothermal waves on evaporating sessile drops are evidenced by infrared thermography. A theoretical method for the rationalization of the results is proposed on the basis of a stability analysis of the normal deformation of the drop surface resulting from a combined Marangoni instability carried by the time dependent regression motion due to evaporation. Trial functions are used to reproduce the patterns observed experimentally. These functions may be used as a basis for future research, and can help in guiding researchers to select the most appropriate forms of perturbation functions for future investigation.

6. Stick-slip behaviour in evaporating nanofluid drops

6.1 Introduction

In this section the various factors which may influence the evaporative behaviour of a nanofluid droplet are studied. In particular, the particle concentration, substrate hydrophobicity, and particulate material are investigated. A drop evaporating on a non-ideal substrate will tend to be pinned to the surface. The drop radius will remain essentially constant during the evaporation process, whilst the contact angle will continuously decrease until it reaches a limiting value, at which point the contact line begins to recede [36, 98]. Deegan et al. [10] investigated the evaporation of pinned droplets containing colloidal particles to study internal flow patterns within a sessile drop. Evaporation at the contact line was found to induce an internal flow of liquid which is drawn to the drop periphery to replace the evaporating liquid. This flow results in the colloidal particles accumulating at the contact line, leaving concentrated rings of particles upon total evaporation.

In this section the evaporation kinetics of sessile nanofluid droplets is investigated. The pinning enhancement observed with the addition of nano-particles is discussed, and a comparison between the results obtained between TiO_2 and Al_2O_3 nanofluids of various concentrations and with different base fluids on various hydrophobic substrates is made. The effect of substrate hydrophobicity is also examined and an attempt is made to provide a simple interpretation of the observed results.

6.2 Experimental Parameters

6.2.1 Setup

The experimental aim was to observe the effect of nano-particle addition on the evaporation kinematics of a pure fluid, namely ethanol. Drops of known volume were deposited on a substrate and the evaporative process was observed visually. An experimental set up was constructed which consisted of a drop shape analyzer (Kruss, DSA 100) which could record the evolution of drop profile (contact angle, drop radius, drop volume) with time, using high speed imaging, an image depicting the system is shown in Figure 6.1. The analyzer provides high-precision dosing and positioning of liquid drops and permits recording and evaluation of video images through accompanying PC controlled software.

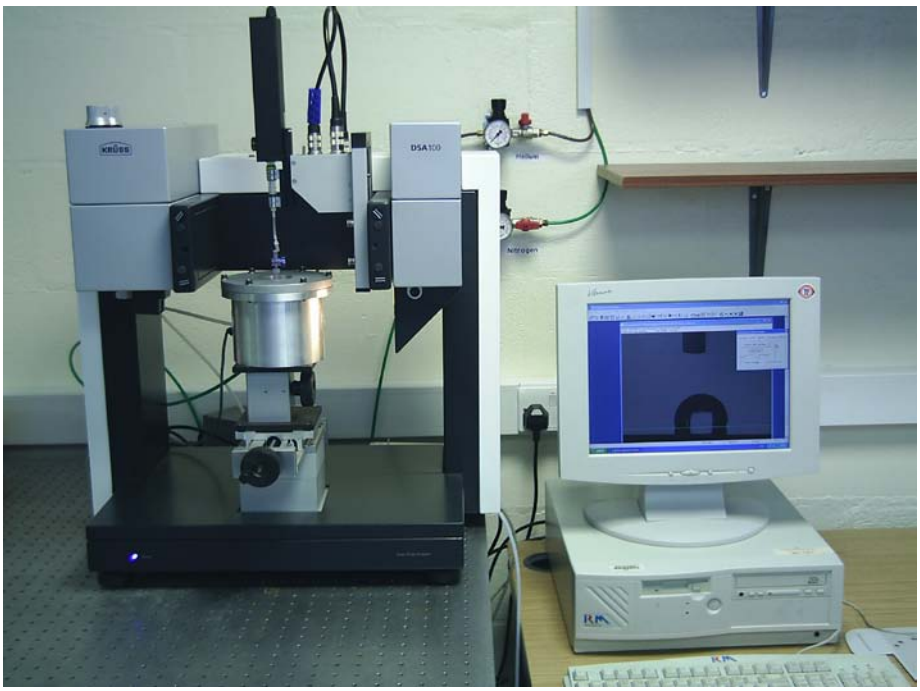

Figure 6. 1. Drop Shape Analyser Kruss DSA 100

A cylindrical chamber, shown in Figure 6.2, was developed to ensure that the experiments were conducted in a clean and controlled environment. As well as preventing contamination from atmospheric particulates, the chamber was also used to control the working atmosphere. All runs were conducted using a nitrogen

atmosphere. The chamber itself was constructed from stainless steel, with borosilicate glass viewing windows embedded in the side walls. Separate connections to the chamber were also constructed, one for the nitrogen supply, a connection line to a vacuum pump to remove the ambient air in the chamber, and one for an electrical cable connected to the horizontal plate. The plate was attached to a vertical axis enabling it to be raised or lowered to control drop deposition.

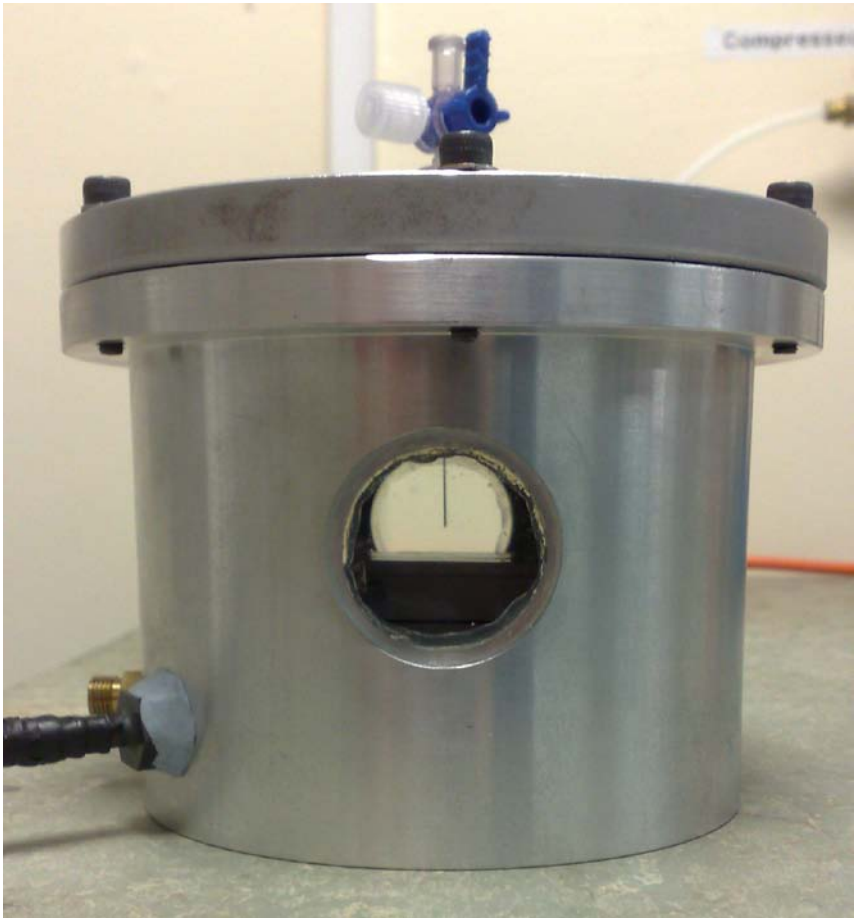

Figure 6. 2. Stainless steel chamber, constructed to maintain a clean nitrogen atmosphere and to control pressure.

6.2.2 Nanofluid Preparation.

Titanium oxide and Aluminium Oxide nanoparticles (Sigma Aldrich) were purchased in powder form; manufacturers specifications give the particle size to be typically <50nm for TiO2 and < 100nm for Al_2O_3. A T.E.M image of the particles revealed an ellipsoidal shape for the Titanium Oxide, and a spherical shape for the Aluminium Oxide particles. Images of the two materials can be seen in Figures 6.3 and 6.4. The particle size was also shown to be in agreement of that given by the manufacturer.

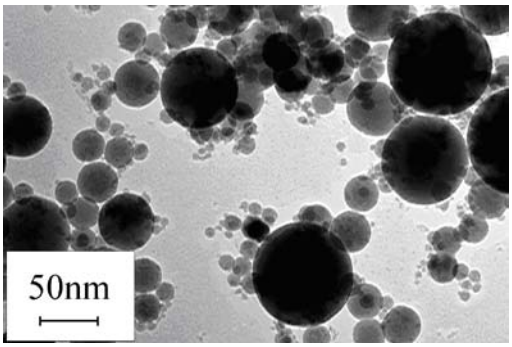

Figure 6. 3. TEM of Al2O3 nanoparticles

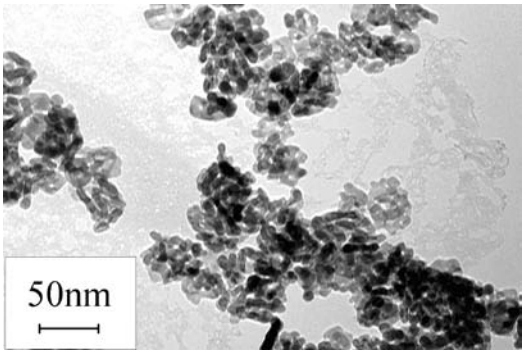

Figure 6. 4 TEM of TiO2 nanoparticles

Nanofluid solutions were prepared by carefully weighing the mass of nano-particles required to achieve the desired concentration onto a microbalance. The fluids were then prepared by adding the required amount of ethanol. In order to achieve a good suspension, the fluids were placed in an ultrasonic bath for 1hr immediately prior to testing.

6.2.3 Substrate preparation.

Three substrates were utilized in these experiments, CYTOP C4F8 and Teflon. These substrates were selected due to their hydrophobic properties and coated onto silicon, a very smooth surfaces which is a requirement to eliminate pinning due to roughness. The substrates themselves were fabricated by using a spin coating method to deposit a sub-micron thick polymer layer over an oxidised silicon wafer. After coating the silicon wafer was then diced into 1cm x 1cm tiles. Prior to commencing

the experimental tests, the surface roughness of each substrate was obtained. Scanning white-light interferometry, a technique in which a pattern of bright and dark lines (fringes) result from an optical path difference between a reference and a sample beam was used to analyse the surface roughness, the results indicate that all surfaces are extremely smooth, as shown in Fig. 6.5.

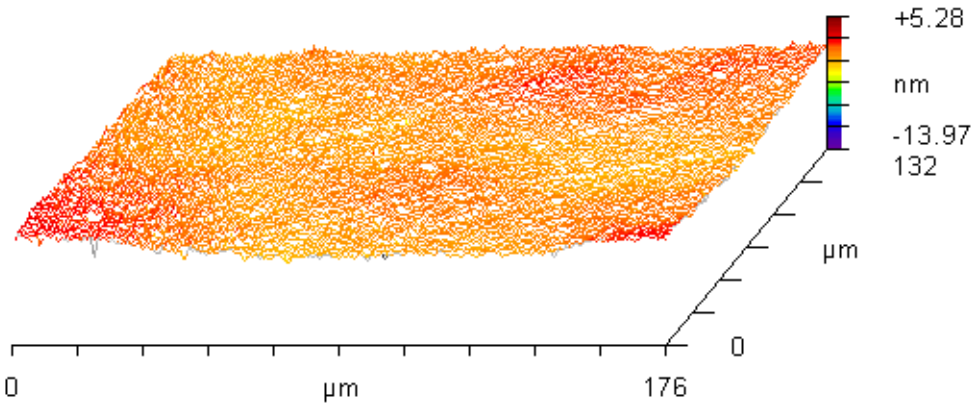

Figure 6. 5. Surface roughness profile obtained with a microscope interferometer(New View 100, Zypo Corp, USA).

6.2.4 Experimental Procedure

Each substrate sample was cleaned before use. This was done by first immersing the substrate in a bath of IPA for approximately 5 minutes to remove any small particles and contaminants from the surface. Compressed air was then used to ensure that any remaining contaminants were removed from the surface, which was subsequently placed in the evaporation chamber. Before each drop was deposited**,** the pressure in the chamber was reduced to 50mbar using a vacuum pump that was connected to the chamber, nitrogen was then supplied until a pressure of 1000mbar was attained. Having reached the required pressure, the liquid was then dispensed from the syringe mounted onto the chamber lid. Scale bars on screen were used as indicators to try and maintain equivalent drop volumes for each experimental run. Once the required pendant drop volume was reached, the substrate was raised until it made contact with the liquid, and then lowered, detaching the drop from the syringe. Care was taken to ensure that the image was as sharp as possible; this was done by

manipulating the manual controls until a sharp, focussed image was displayed on screen, with a clear definition at the contact line.

6.3 Results

6.3.1 Effect of Substrate Hydrophobicity.

Three substrates were prepared to allow us to compare the effect of substrate hydrophobicity, Teflon, CYTOP, and C_4F_8. As previously stated these were prepared using a spin coating technique. Sample tests using pure ethanol indicate that the equilibrium contact angle for ethanol on Teflon was ca 10-15° higher than that of CYTOP, with the lowest contact angle found on the C4F8 surface. The equilibrium contact angle of ethanol on C_4F_8 was ca. 18°C, CYTOP was around 44° and Teflon was ca. 58°C. Results are presented in Figure 6.6 of base radius, R vs. time, t, on each of the three substrates. It can be clearly observed from the graph that the base radius appears to recede quite homogeneously, and monotonically, as time progresses in the case of Cytop and Teflon. These results are similar to that expected during evaporation on an ideal surface, where surface roughness and chemical heterogeneity isn't a factor. In contrast, the base radius appears to remain essentially constant on the less hydrophobic C_4F_8 substrate.

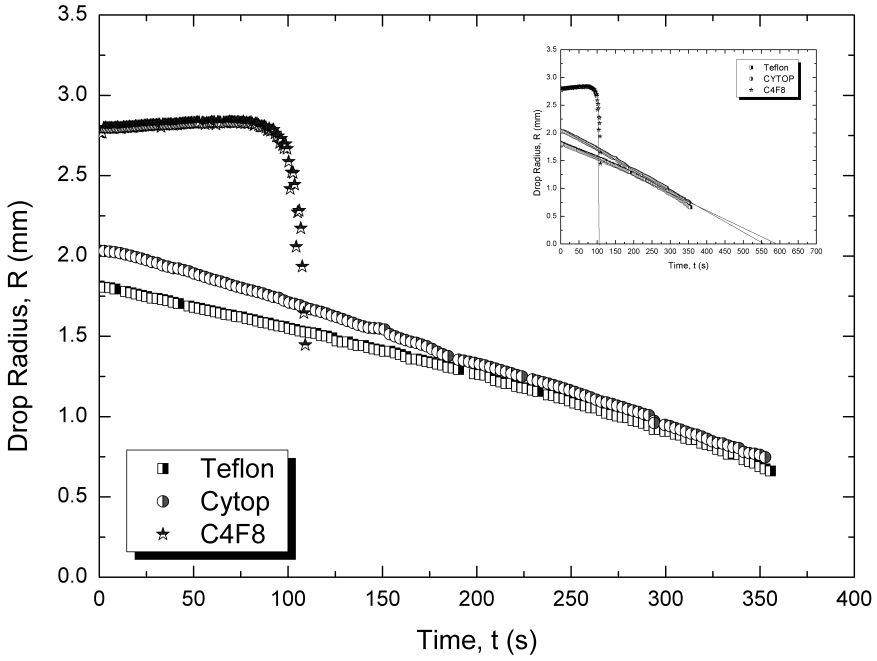

Figure 6. 6. Contact Radius, *R*, vs. time, *t*, for ethanol on PTFE, Cytop, and C_4F_8. Inset shows extrapolation to estimate total time to evaporation.

In contrast, the contact angle, θ, is observed to remain almost constant during the evaporative lifetimes on the Cytop and Teflon surface, whilst it decreases temporally on C_4F_8. This behaviour is indicated in Figure 6.6.

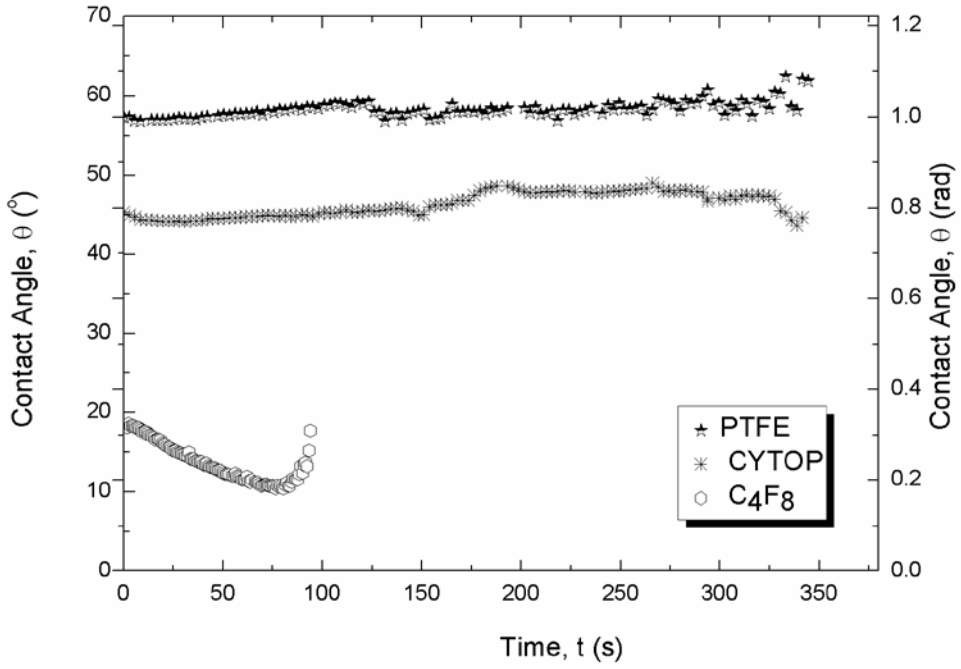

Figure 6. 7. Contact angle, θ, vs. time, t, for ethanol on PTFE, Cytop, and C_4F_8.

These results indicate that there is little pinning of the contact line in the case of Teflon and Cytop, whilst the contact line remains essentially pinned for the bulk of the evaporative lifetime in the case of C_4F_8, which is similar to what would be expected on a non-ideal surface. Similar results were obtained on subsequent runs (3-5 per surface).

6.3.2 Effect of nanoparticle addition

The evaporative behaviour of pure ethanol on the three surfaces provides a good basis to examine the effect of nano-particle addition. The results in this section will focus on the behaviour mainly of nanofluid drops on both the Cytop and Teflon surfaces. As C_4F_8 was already shown to exhibit almost total pinning, testing nanofluids on this surface was essentially redundant.

TiO_2 – Ethanol nanofluids

Initial tests were conducted on Cytop substrates. TiO_2 ethanol nanofluids were prepared in several concentrations (0.01%, 0.05%, 0.1%, and 1% by weight). Care was taken to ensure that drops were placed on the substrates in the same way as had been conducted with the pure ethanol tests. Initial tests at 0.01% indicated that the introduction of particles into the bulk fluid began to alter the evaporative process. Perturbations were observed in the drop contact angle as evaporation proceeded, this is shown in Figure 6.8.

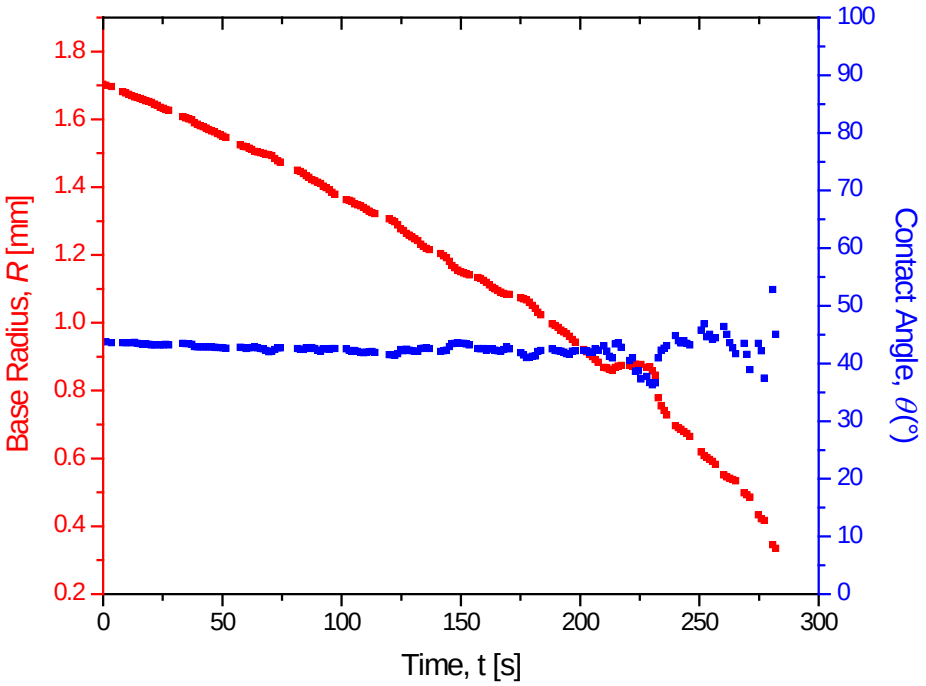

Figure 6. 8. Evaporative behaviour of 0.01% TiO_2 nanofluid on Cytop, mild stick slip perturbations can be seen.

The perturbations are seen to be very minimal at early drop lifetimes, and begin to increase as the drop evaporated. Overall the contact angle did not deviate significantly over the whole drop lifetime at a concentration of 0.01%. Increasing the concentration to 0.05% was shown to enhance this pinning effect, Figure 6.9.

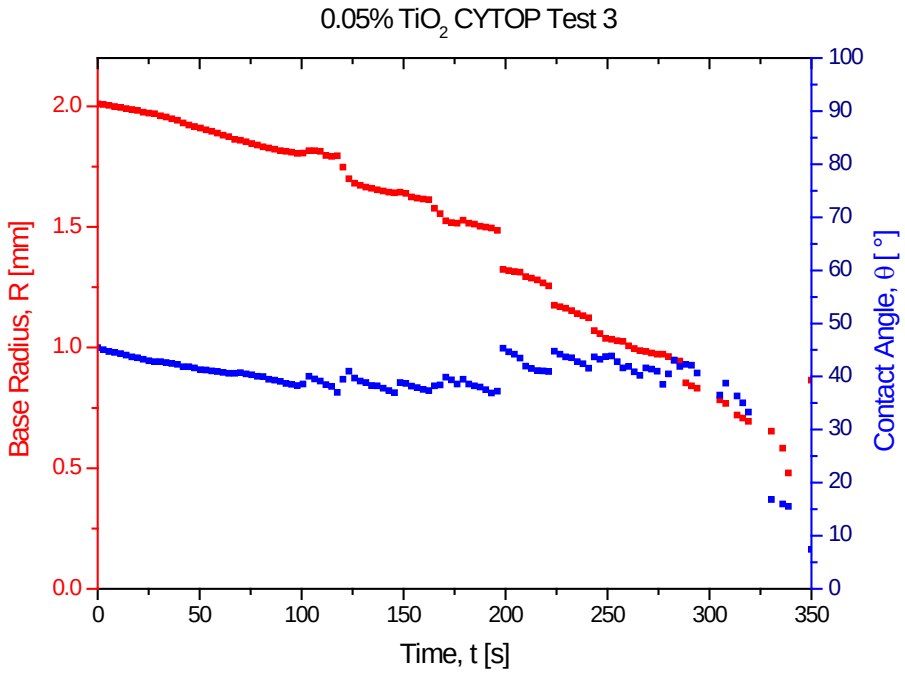

Figure 6. 9. Evaporative behaviour of 0.05% TiO_2 nanofluid on Cytop, distinct stick slip perturbations can be seen.

In Figure 6.9 distinct periodic stick-slip is present, the base radius initially decreases in time in a similar fashion to the case of pure ethanol. However there are periodic stages where the base does not recede, resulting in a decrease of drop contact angle as evaporation occurs. This behaviour is even more evident when the concentration of nanoparticles is increased even further. Figure 6.10 presents the evaporative behaviour of a 0.1% TiO_2-ethanol drop.

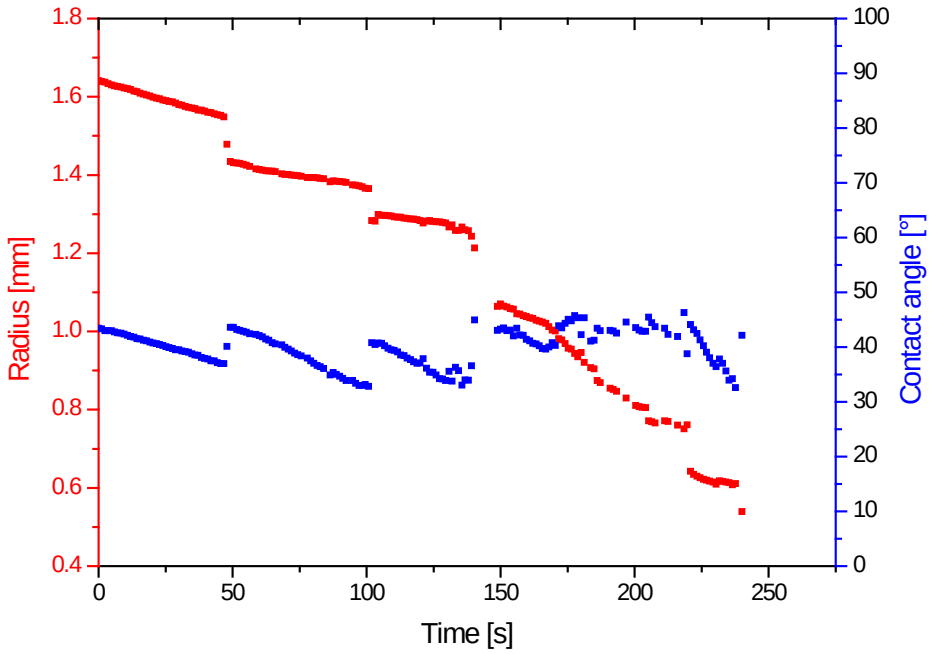

Figure 6. 10. Evaporative behaviour of 0.1% TiO_2 nanofluid on Cytop, distinct stick slip perturbations can be seen.

As can be observed from Figure 6.10, a distinct stick slip evaporative behaviour is observed at this concentration. The drop contact angle decreases as evaporation procedes, until it reaches a critical angle, at which point the drop base 'de-pins' from the surface and recedes to a new, smaller radius, at the same time the drop contact angle increases. We can see from the figure that during the evaporative stick phase, there is still some evidence of receding drop radius present, this is discussed more fully in the discussion section. Upon complete evaporation, we can observe the nanoparticles which have been deposited on the substrate surface. When these are examined, the stick slip phenomenon can be easily identified. Figure 6.11 illustrates the deposit patterns left by the drop which is presented in figure 6.10.

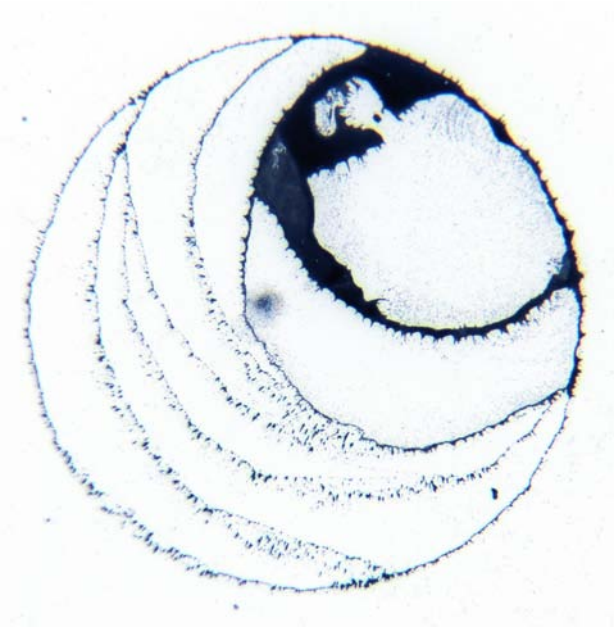

Figure 6. 11. Photograph of substrate surface after evaporation of ethanol containing a 0.1% by weight suspension of TiO2 nano-particles. Rings of accumulated particles correspond to ‘stick’ in the stick-slip cycle. Outer ring diameter ca. 2.4mm

The figure illustrates the stick slip pinning and de-pinning phenomenon at work. The rings of particles accumulate at the drop contact line during the pinned phase, the relatively particle free regions are the result of the de-pinning stage where the drop rapidly recedes to a smaller radius. Clearly, increasing the particle concentration appears to increase the transition from constant contact angle evaporation to intermittent stick slip. By increasing the concentration even further, a point can be reached in which the drop remains essentially pinned for the majority of the drop lifetime. This is shown in figure 6.12.

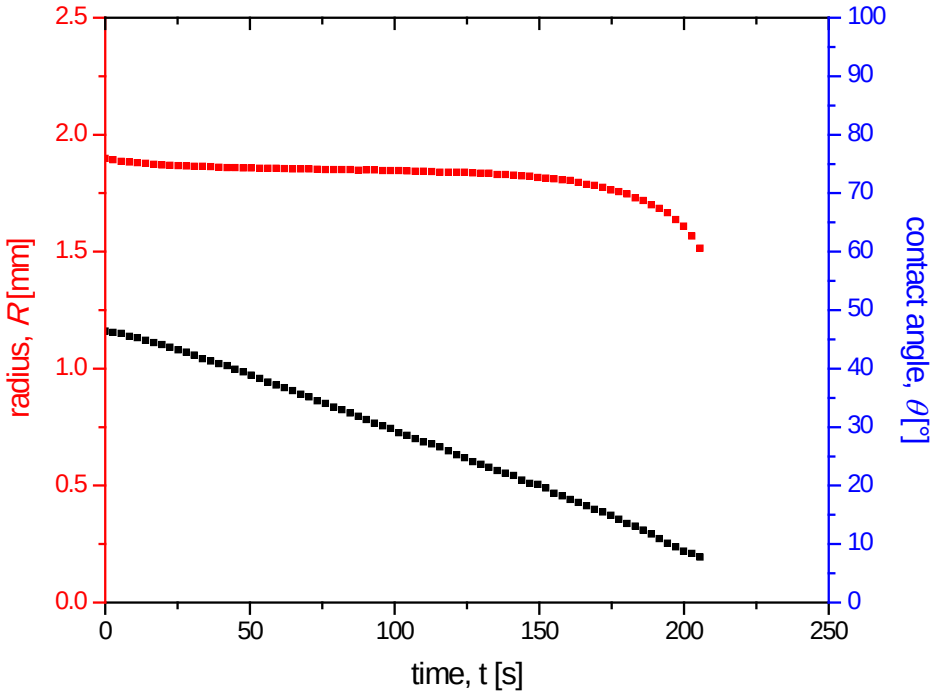

Figure 6. 12. Evaporative behaviour of 1.0% TiO_2 nanofluid on Cytop Almost total pinning is observed for majority of drop lifetime.

The drop radius remains constant for the vast majority of the drop lifetime and appears to drift only at a late stage in the evaporative process. Clearly increasing the concentration of nanoparticles has direct effect on the evaporative process. This interesting result was then investigated on Teflon coated substrates to provide a comparison with a surface which displays a higher degree of hydrophobicity. Initial tests were conducted with a particle concentration of 0.1%. These results are presented in Figure 6.13.

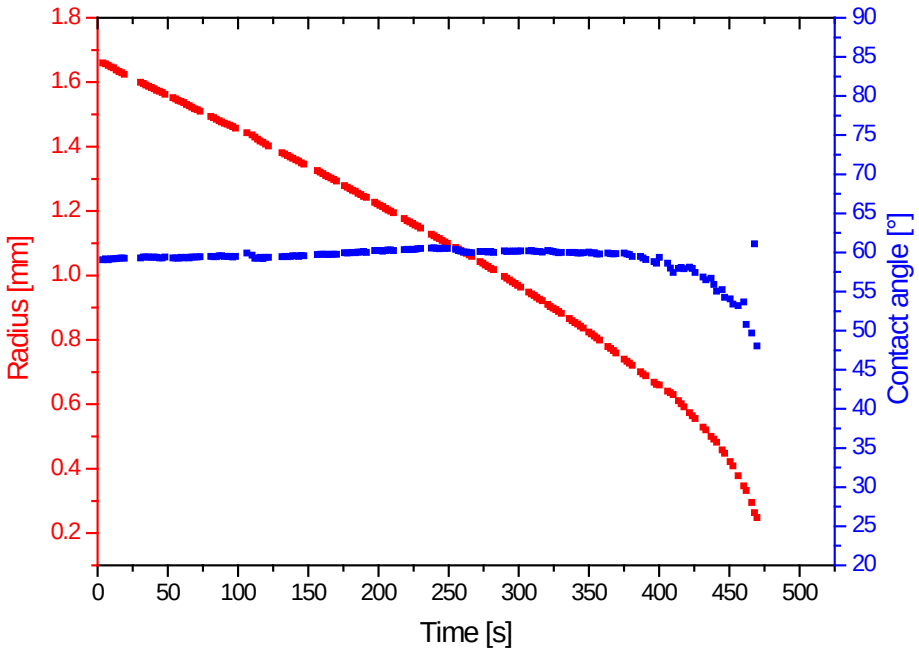

Figure 6. 13. Evaporative behaviour of 0.1% TiO_2 nanofluid on Teflon, vary little pinning is observed.

Direct comparison between the two surfaces for the case of 0.1% TiO_2- ethanol drops indicates that the particles enhance pinning on Cytop in a more pronounced fashion. On Teflon the drop continues to evaporate with a constantly decreasing drop radius. The fact that the same concentration of nanofluid can behave quite differently on CYTOP than it does on Teflon is an interesting result. It is clear that on Cytop the drop spreads further than on Teflon, this is shown by the larger initial drop radius and lower contact angle observed in Figs. 6.9,6.10, and 6.11, in comparison to Fig. 6.13. It appears that the lower initial contact angle enhances pinning of the substrate. To investigate this further, a comparison was made between the two substrates using the Al_2O_3 nanofluid. Figure 6.14 shows the evolution of drop radius and contact angle in time for a 0.05% Al_2O_3 nanofluid drop. It is clear from the graph that on the CYTOP substrate the drop is pinned for the majority of the evaporative process. The contact angle decreases steadily and the base radius is essentially constant.

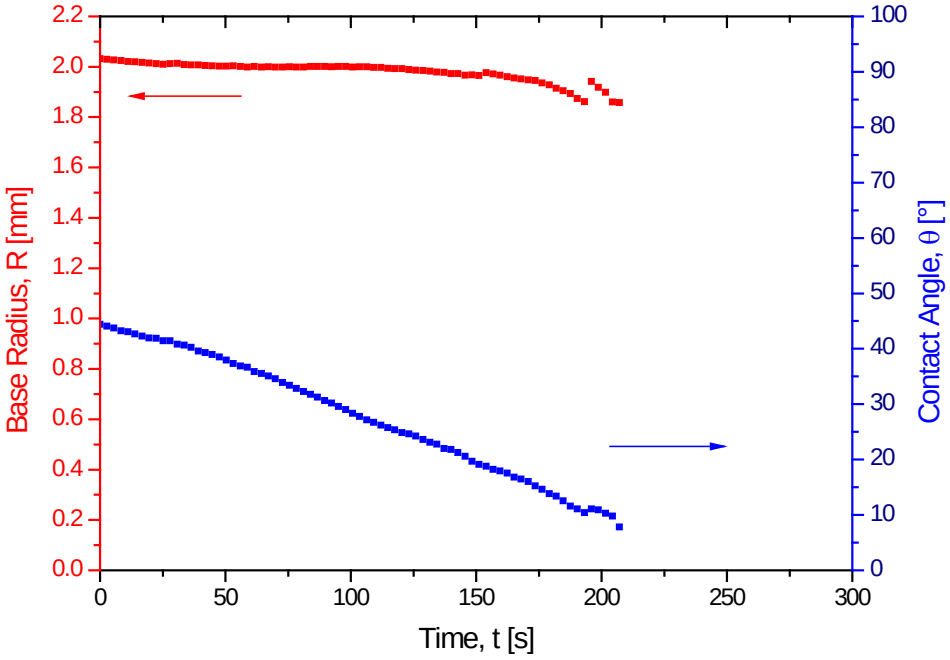

Figure 6. 14. Radius and Contact Angle vs. Time for 0.05% Al_2O_3 drop on CYTOP substrate.

This pinning is also evident at higher concentrations of Al_2O_3 nanofluids on CYTOP. Evaporation of Al_2O_3 nanofluid on Teflon however, displayed very different results. On Teflon the pinning effect was again minimal, as was the case with TiO_2 particles on the Teflon substrate. Figure 6.15 depicts the drop evolution for a 0.05% Al_2O_3 drop on Teflon. Again the base radius can be seen to constantly decrease, much like the results in Fig. 6.14.

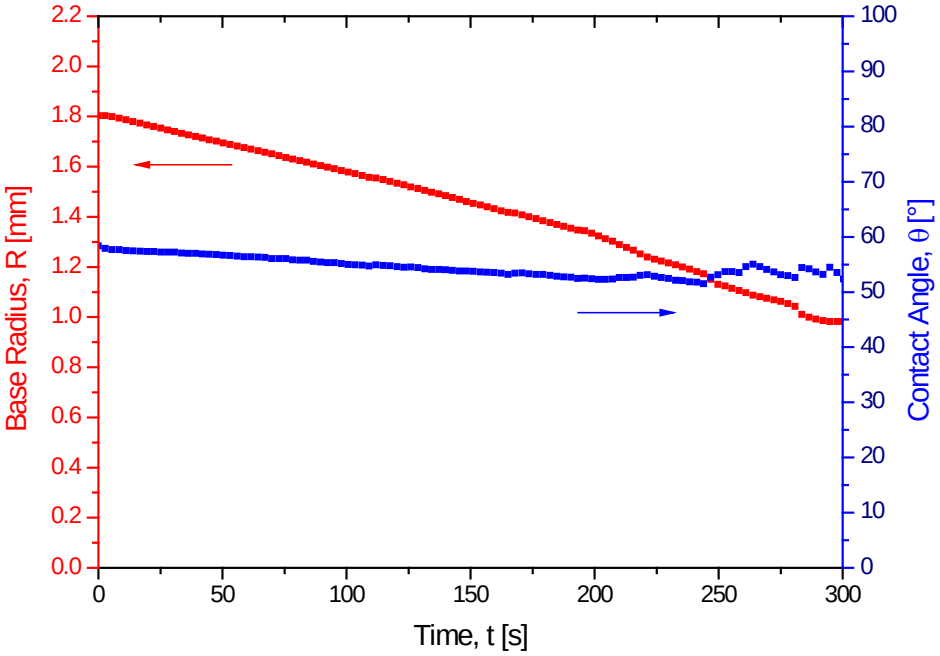

Figure 6. 15. Radius and Contact Angle vs. Time for 0.05% Al_2O_3 drop on Teflon substrate.

The contact angle remains essentially constant in time, with small perturbations towards the end of the drop lifetime. This behaviour is noticeably distinct from the same drop concentration on Cytop. It is clear that the hydrophobicity of the substrate plays a role in determining the evaporative behaviour of the drop. It appears that drops with higher initial contact angles (i.e. drops deposited on very hydrophobic surfaces) exhibit less pinning during evaporation than those with a lower initial contact angle. The evaporative process must then be in some way reliant on the hydrophobicity of the surface. From these results a simple attempt at interpreting the data has been made.

6.4 Discussion and interpretation

6.4.1 Dependence of drop lifetime on substrate hydrophobicity

In Figures 6.6 and 6.7 results are presented of drop contact radius, *R*, and contact angle, θ, *vs* time, *t*, for pure ethanol. It is clearly visible, apart from a few slight experimental variations, that contact radius, *R*, decreases (approximately) linearly with time, whilst contact angle, θ, remains essentially constant. Similar results were obtained by several independent experimental runs. This is quite consistent with what would be expected during the evaporation of an ideal sessile liquid drop on an ideal solid surface, for which hysteresis effects are nonexistent, or at least, negligible. Provided the kinetics of evaporation is relatively slow compared to the kinetics of accommodation of the drop to its configuration of minimum free energy for a given volume (by internal flow and recession of the triple line), then the contact angle should indeed remain constant. This indicates that pinning of the TL is inconsequential. It is instructive at this point to consider the essential differences between the behaviour of Cytop® and Teflon® on one hand and that of C_4F_8 on the other. The last has by far the lowest (typical) value of contact angle, θ. Young's equation may be written as:

$$0 = \gamma_{SL} - \gamma_{S(V)} + \gamma \cos\theta_o \qquad (6.1),$$

where γ_{SL}, $\gamma_{S(V)}$ and γ are respectively solid/liquid, solid (in the presence of vapour) and liquid surface tension, and θ_o is equilibrium contact angle. If the contact angle decreases by a small amount, $\delta\theta$, following evaporation, there exists a force (per unit length of triple line), $\delta\vec{F}$, 'attempting' to move the triple line (to cause recession) (see Figure 6.16):

$$\delta\vec{F} = \gamma_{SL} - \gamma_{S(V)} + \gamma \cos(\theta_o - \delta\theta) \approx \gamma \sin\theta_o . \delta\theta \qquad (6.2).$$

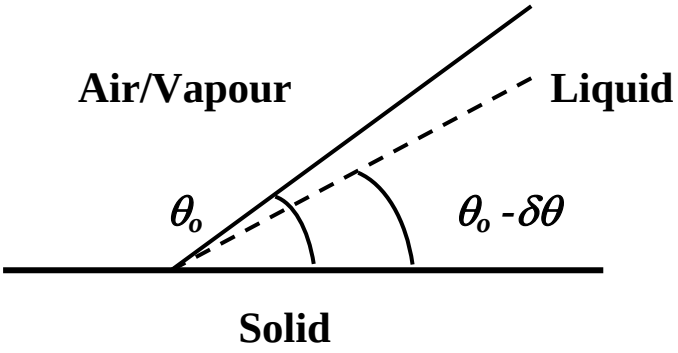

Figure 6. 16. Schematic representation of triple line region with liquid surface at its equilibrium contact angle, θ_o , and at a slightly smaller angle, $(\theta_o - \delta\theta)$.

If there exists an intrinsic energy (or force) barrier, *U*, opposing triple line motion (wetting hysteresis) [36], then for a given liquid, a small value of θ_o implies a small value of $\delta\vec{F}$ unless $\delta\theta$ is larger. Thus a larger deviation from equilibrium is required before the triple line depins. Presumably, with the results obtained, θ_o is sufficiently large for ethanol on both Cytop® and Teflon® in order for depinning to occur virtually continuously, or for very small $\delta\theta$, leading to a constant value of θ, at least at the observable scale. (The slight variations seen in Figure 6.6 could well be related, at least partially, to small scale unpinning.) However, ethanol on C_4F_8, with a much lower value of θ_o , presumably cannot 'generate' enough force to overcome the barrier created by the accumulation of particles, at least until θ has decreased to *ca*. 12°, towards the end of drop lifetime. Returning to Figures 6.6 and 6.7, in which it can be seen that for pure ethanol, contact angle, θ, remains essentially constant during the entire process of evaporation for the PTFE and the Cytop® substrates, an attempt can be made to explain drop lifetime, t_f, as follows. Evaporation flux, $\vec{J}.\vec{n}$ (the vector notation with $\vec{n}$ as unit normal to the surface is simply to 'formalise' evaporation, $\left|\vec{J}\right|$, perpendicular to the liquid surface) may be expressed as:

$$\vec{J}.\vec{n} = J_o\left(1-\frac{r^2}{R^2}\right)^{-\lambda(\theta)} \qquad (6.3),$$

where J_o represents flux perpendicular to a planar liquid surface, r is radial distance and R is drop contact radius. The exponent $\lambda(\theta)$ is equal to $(\pi-2\theta)/(2\pi-2\theta)$, according to Deegan *et al.* [10] whereas an apparently improved version is given by $\lambda(\theta)$ equal to $0.5-\theta/\pi$, suggested by Hu and Larson [14]. The latter is adopted in the following. In either case, evaporation rate is exacerbated near the triple line, and increasingly so for small values of contact angle. Assuming the above, it is possible to calculate overall evaporation rate, $\dot{M}(\theta)$, or rate of mass loss, as a function of θ from:

$$\dot{M}(\theta) = -\int_0^R 2\pi r\sqrt{1+y'^2}.\,\vec{J}.\vec{n}\;dr \approx -2\pi R^2 J_o\int_0^1 \frac{z\left[1+(z^2\theta^2/2)\right]}{(1-z^2)^{\lambda}}\,dz \qquad (6.4),$$

where $z = r/R$ and spherical drop geometry of sufficiently low θ may be approximated by height, $y \approx (R^2 - r^2)\theta/2R$. In fact, the term on the right, in $(z^2\theta^2/2)$, only contributes *ca.* 22% of the integral, even for the 'worst' case considered, of $\theta \approx 1$ radian, but it is retained nevertheless below, since it only slightly complicates the algebraic expressions. Integration leads to:

$$\dot{M}(\theta) \approx \frac{-\pi R^2 J_o}{(1-\lambda)}\left[1+\frac{\theta^2}{2(2-\lambda)}\right] \qquad (6.5).$$

Interestingly, equation (6.5) shows a quite distinctive scaling law of $\dot{M} \sim R^2$. This is *not* in agreement with Deegan et al.'s postulate [10] of $\dot{M} \sim R$. Despite the recognised, exacerbated evaporation near the contact line, the expression formally retains an R^2 dependence.

In the general case, $\theta = \theta(t)$, which would make integration of $\dot{M}(\theta(t))$ in equation (6.5) very difficult, since $\lambda = \lambda(\theta(t))$ also. Fortunately, there are two limiting cases, at least to a good approximation, which allows considerable simplification. As discussed above, for both Cytop® and Teflon®, contact angle, θ, remains virtually constant throughout evaporation, whilst for C_4F_8, contact radius, R, does not change significantly until near the end of drop lifetime.

In the former case, drop volume, V, is approximated by $V = M/\rho \approx \pi R^3\theta/4$, where M is drop mass and ρ is liquid density, leading to:

$$\dot{M}(\theta) \approx \frac{-d}{dt}\left(\frac{\rho\pi\theta R^3}{4}\right) = \frac{-3\rho\pi\theta R^2}{4}.\frac{dR}{dt} \approx 2\pi^2 R^2 J_o \frac{(3\pi + 2\theta + \pi\theta^2)}{(3\pi^2 + 8\pi\theta + 4\theta^2)} \qquad (6.6).$$

With θ constant (= initial value θ_o), direct integration of equation (6.6), with the boundary condition of $R(t = 0) = R_o$ (R_o is initial contact radius) leads to:

$$(R_o - R) \approx \frac{8\pi J_o t}{3\rho\theta_o}.\frac{(3\pi + 2\theta_o + \pi\theta_o^2)}{(3\pi^2 + 8\pi\theta_o + 4\theta_o^2)} \qquad (6.7).$$

Figure 6.6 corroborates the linear dependence of drop radius decrease with time in agreement with equation (6.7) for ethanol on Cytop® and Teflon®. Taking t_f as drop lifetime, *i.e.* when R becomes zero, we may express equation (6.7) as:

$$t_f \approx \frac{3\rho}{8\pi J_o}\left[\frac{4V}{\pi}\right]^{1/3}.\frac{\theta_o^{2/3}(3\pi^2 + 8\pi\theta_o + 4\theta_o^2)}{(3\pi + 2\theta_o + \pi\theta_o^2)} \qquad (6.8),$$

where V refers to initial drop volume.

On the other hand, if wetting line pinning occurs, it is R (= R_o) which remains (approximately) constant and θ which decreases, in which case:

$$\dot{M}(\theta) \approx \frac{-d}{dt}\left(\frac{\rho\pi\theta R^3}{4}\right) = \frac{-\rho\pi R^3}{4}.\frac{d\theta}{dt} \approx 2\pi^2 R^2 J_o \frac{(3\pi + 2\theta + \pi\theta^2)}{(3\pi^2 + 8\pi\theta + 4\theta^2)} \qquad (6.9).$$

Alternatively, assuming drop lifetime to be terminated at $\theta = 0$ (starting at θ_o):

$$\frac{8\pi J_o t_f}{\rho R} \approx \int_0^{\theta_o} \frac{(3\pi^2 + 8\pi\theta + 4\theta^2)}{(3\pi + 2\theta + \pi\theta^2)} d\theta \approx \pi(4\theta_o - \frac{9\pi}{2}\ln(1+\frac{2\theta_o}{3\pi})) \approx \pi\theta_o \qquad (6.10).$$

The integral above is not straightforward, but since small values of θ are relevant (< 0.35 rad.), it may be simplified without much loss of precision by neglecting terms in θ^2, to give the right hand term of equation (6.10). In fact, equation (6.10) also implies a linear dependence of θ on time, as suggested in Figure 6.7. More significant is the expression estimating drop lifetime:

$$t_f \approx \frac{\rho R\theta_o}{8J_o} \approx \frac{\rho\theta_o^{2/3}}{8J_o}\left[\frac{4V}{\pi}\right]^{1/3} \qquad (6.11).$$

Equations (6.8) and (6.11) could be used to estimate drop lifetime for the two cases discussed, but unfortunately, little *a priori* knowledge of J_o, the evaporation current flux at the drop centre exists, although θ, ρ and V are accessible. Hu and Larson [14] suggested that J_o depended on intrinsic contact angle, although Kelvin's equation would tend to indicate that any effect is negligible, for the following reason. It is true that J_o is the evaporative flux at the drop centre, which, strictly speaking, is curved and not flat. The equilibrium vapour pressure, p, for this curved surface, of radius of curvature, κ^{-1}, is related to that of a flat liquid surface, p_o, by:

$$p = p_o \exp\left(\frac{2V_m\gamma\kappa}{RT}\right) \qquad (6.12),$$

where V_m is the molar volume of the liquid and *RT* have their usual meaning of the product of ideal gas constant and absolute temperature. It is readily checked, with V_m of order 5 x10^{-5} m^3 $mole^{-1}$ and κ^{-1} *ca*. 1 mm, that the exponential argument is of order of 10^{-6} for the drop sizes in question and thus $p \approx p_o$. However, there *is* a potential effect of drop curvature, which is discussed below.

Notwithstanding, to circumvent the absence of definitive knowledge of J_o (see below) let us define a constant, *K*, by: $K \approx 3\rho\left[4V/\pi\right]^{1/3}/8\pi J_o$, in which case with a 'normalised' lifetime, $\tilde{t}_f = K^{-1}t_f$, we have:

$$\tilde{t}_f \approx \frac{\theta_o^{2/3}(3\pi_o^2 + 8\pi\theta_o + 4\theta_o^2)}{(3\pi + 2\theta_o + \pi\theta_o^2)} = f(\theta_o) \qquad (6.13a),$$

$$\tilde{t}_f \approx \frac{\pi\,\theta_o^{2/3}}{3} = g(\theta_o) \qquad (6.13b),$$

where equations (6.13a) and (6.13b) refer respectively to the cases of smooth wetting line recession (Cytop® and Teflon®) and pinning (C_4F_8). Functions $f(\theta_o)$ and $g(\theta_o)$ can be readily calculated.

Simple regression theory can now be applied to the equations $t_f = Kf(\theta_o)$ and $t_f = Kg(\theta_o)$ in order to estimate *K*, taking $f(\theta_o)$ and $g(\theta_o)$ as the independent variable, and using the experimental values of both t_f and θ_o for the three substrates. This may either be done by straightforward regression analysis [*viz*. $t_f = a + b\,f(\theta_0)$, or $t_f = a + b\,g(\theta_0)$; *a* and *b* being constants], using four effective experimental points [since (0,0) is also a valid point], or by using a fit forced by the origin [*viz*. $t_f = K\,f(\theta_0)$ and $t_f = K\,g(\theta_0)$]. Both procedures have been used and Figure 6.17 shows the results. The standard fit leads to *a* = 13 s and *b* = 169 s (equivalent to *K*), and for the forced fit, *K* = 172 s, with correlation coefficients of *ca*. 0.999. It may be seen that there is

little to chose and a reasonable value of 170 ± 30 s for *K*, given the degree of precision in question.

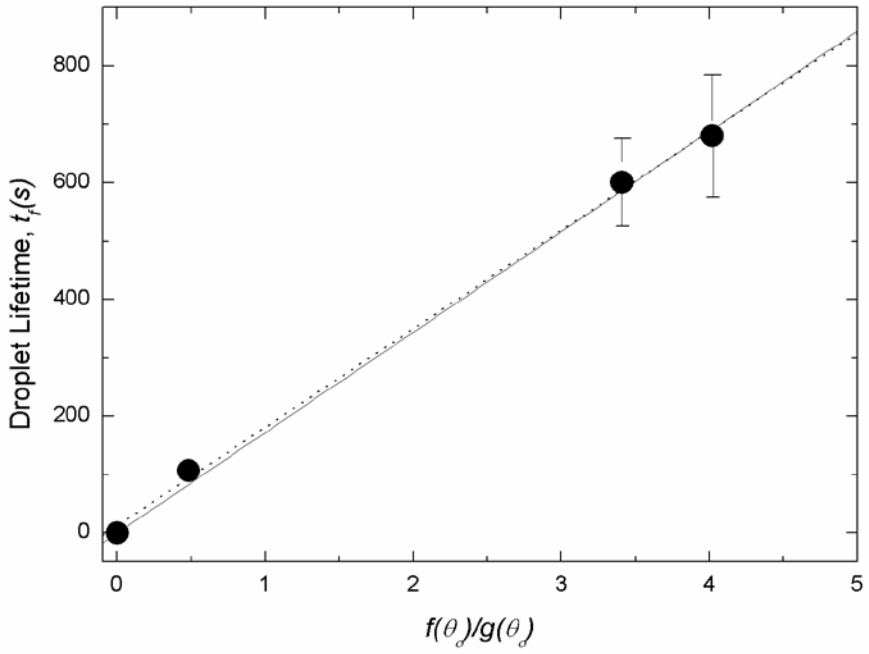

Figure 6. 17. Drop lifetime, t_f, *vs* either function $f(\theta_o)$ or $g(\theta_o)$, as given by equations (13). Continuous line corresponds to 1-parameter regression fit and dotted line to normal, 2-parameter fit.

Figure 6.17 presents $\tilde{t}_f$ *vs.* θ(rad.) as two curves, calculated from equations (6.13). For higher values of θ_o , (6.13a) is applicable and for lower, (6.13b). The solid lines in Figure 6.18 correspond to the approximate ranges of validity and the dotted lines represent continuity of the functions. However, the transition value is not known, only that it is somewhere between θ_o equal to *ca*. 20° and 45°. Applying expressions (6.8) and (6.11), the experimental values are then placed on Figure 6.17 using the accepted value of *K*. The agreement is acceptable and certainly shows a clear correlation between drop lifetime and intrinsic contact angle. Note that the two curves coincide *nowhere*, excluding the origin, of course. These are two *distinct regimes*. Agreement of the values for Cytop® and Teflon® and for C_4F_8 hinges on the success of the calculation of *K*. In Figure 6.17 a transition is surmised between the two regimes over a range of intermediate values of θ_o , corresponding to the change between pinning

and (virtually) continuous triple line recession, and shown as a sigmoidal dotted line. Its position, however, is not known. These experimental results belong either to the constant pinning range (apart from a final jump of the wetting line near final disappearance), or smooth triple line recession.

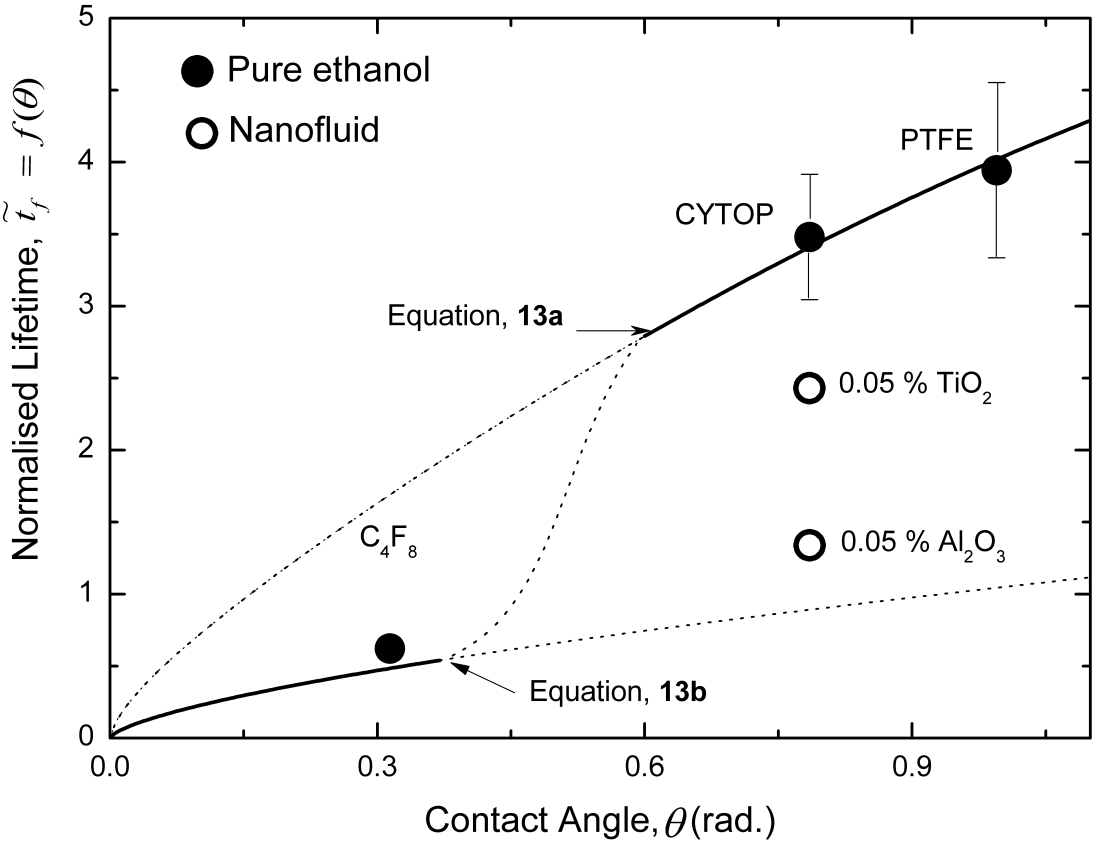

Figure 6. 18. Normalised drop lifetime, $\tilde{t}_f = f(\theta)$ or $\tilde{t}_f = f(\theta)$ [see equations (13)] *vs*. contact angle, θ, and experimental points (black) after application of calculated scaling factor, *K*. Upper curve corresponds to behaviour at constant contact angle, and lower curve at constant contact radius. The two nanofluid results represent examples of 'stick-slip' behaviour, between the two extremes.

It is worth noting from Figure 6.17 that for a given (initial) value of contact angle, the pinning regime leads to a considerably shorter drop lifetime than the smooth, triple line recession regime, and therefore higher overall evaporation rate. This may possibly be useful in certain cooling applications and since pinning may be increased by suitable surface treatment (*e.g*. by roughening), these observations may prove of practical use. (Also, the inclusion of nanoparticles may be exploited, as results above suggest.)

Drop volume, V, and density, ρ, are respectively *ca*. 5 μL and 790 kg m^{-3}. Using the expression above to evaluate $J_o \approx 3\rho[4V/\pi]^{1/3}/8\pi K$, a value for J_o of *ca*. 1.0 ± 0.2 x 10^{-3} kg m^{-2} s^{-1} is obtained. (The error incurred by the uncertainty on V is, in fact, negligible, representing less than 5% of that on K.)

There is some doubt about values of J_o, and therefore the estimate above is difficult to consider in absolute terms. Notwithstanding, an attempt can be made at an order of magnitude calculation as follows, assuming that an average value [not allowing for differences of flux on the drop surface, *cf*. see equation (6.3)] is reasonable. Using the steady state simplification of Fick's laws of diffusion to account for evaporation:

$$J_o = -D\frac{\partial C}{\partial \tilde{r}}; \qquad \tilde{r} > R \tag{6.14},$$

$$\nabla^2 C = \frac{1}{\tilde{r}^2}\frac{\partial}{\partial \tilde{r}}\left(\tilde{r}^2 \frac{\partial C}{\partial \tilde{r}}\right) \approx 0 \tag{6.15},$$

where $\tilde{r}$ is radial distance from the *spherical centre of symmetry* (*i.e.* below the solid surface) of the drop (but treating it as a 'point', with respect to the environmental chamber, which is much larger), D is diffusion coefficient of ethanol in air (nitrogen) and C is vapour concentration (kg m^{-3}). Assuming saturation in ethanol vapour, C_{SAT}, at the drop surface, corresponding to a radius *of curvature* of *ca*. $R/\sin\theta$, and $C = 0$ at infinity, it is readily shown from equations (6.11) and (6.12) that:

$$J_o \approx \frac{DC_{SAT}\sin\theta}{R} \tag{6.16}.$$

C_{SAT} may be calculated from $C_{SAT} = M_W P_V/(RT)$, using the law for ideal gases, where M_W is the liquid molecular weight (46 g mole^{-1}) and P_V is the saturated vapour pressure (*ca*. 6 x 10^{-2} bar), giving a value of *ca*. 0.11 kg m^{-3}. With D = *ca*. 1.1 x10^{-5} m^2 s^{-1}, and R = *ca*. 1mm, a value is obtained $J_o \approx$ 4-10 x 10^{-4} kg m^{-2} s^{-1}, depending on the contact angle. (As suggested above, this is where the radius of curvature may play a role, if in an approximate manner.) Clearly the order of magnitude is the same

as that calculated above, tending to corroborate the findings in this chapter. It is accepted that precision is necessarily poor, but the value at the top of the range, obtained from the first calculation involving experimental values, may possibly be attributed to the exacerbation of evaporation near the triple line, first noted by Deegan *et al*. [10]. Given the simplicity of the approach, the agreement may be considered satisfactory.

6.4.2 Influence of nanoparticles on evaporative behaviour

The previous section discussed the interesting behaviour of pure ethanol evaporating on substrates of varying hydrophobicities. This section shall rationalize the results obtained when nanoparticles are introduced.

As the percentage of TiO_2 nano-particles is increased, behaviour becomes more "stick-slip". Let us consider the more marked case of the addition of 0.1% of TiO_2 particles. Both contact radius, R, and contact angle, θ, are shown *vs* time, t, in Figure 6.10. The contact radius can be seen to decrease with time, but this occurred in different ways. There are periods of slow decrease, for example between *ca*. 50 and *ca*. 100 seconds, but also rapid downward jumps between these former steady reductions. This behaviour is clear for relative short times after the beginning of the experiment, but is maintained in a less clear-cut way even towards the end of drop lifetime.

Investigating the corresponding contact angle, θ, there is a correlation between decreasing contact angle and (slowly) decreasing contact radius, R, but there are rapid *increases* in θ coinciding with the contact radius jumps. These jumps were sufficiently rapid for individual experimental points to be difficult to record. The slow "drift" periods are similar, but not identical to the "stick" phases anticipated in reference [36], and corresponding to pinning (or in this case, "braking") of TL recession. The effect is more marked with the higher TiO_2 concentration. Another point of interest is that the average speed at which the TL recedes appears to be lowered by the inclusion of nano-particles in the ethanol. It is as if the nano-particles were increasing the effective liquid viscosity as, indeed, is known to happen in at least some circumstances [99-102].

Clearly, in the absence of nano-particles, the behaviour is virtually ideal, yet the addition of a small quantity of TiO_2 disturbs things considerably. It was observed by Deegan *et al.* [10]that the addition of only *ca*. 2% of sulphate-terminated polystyrene micro-spheres to water effectively led to pinning of the triple line, TL, of sessile drops throughout the evaporation process. It is therefore perhaps not surprising that in the present case, there is a tendency for pinning (or "self-pinning") to occur

with low concentration suspensions of nano-particles. Pinning is synonymous with wetting hysteresis. However, there is also what appears to be “pseudo-pinning” present. The TL is essentially static, at least compared to its behaviour, at a jump, but there is nevertheless a slow receding drift.

The basis of the simple proposition is that, as a liquid drop evaporates, if wetting hysteresis is present, its contact radius, R, remains constant (pinning) whilst contact angle, θ, decreases, Figure 6.19 (a). This implies that the drop is then out of thermodynamic equilibrium since Young’s equation is no longer respected. However, when the excess free energy due to a contact angle which has become too low, is sufficiently great, this may suffice to overcome the hysteretic energy barrier, and make the TL jump towards a more conducive position: a smaller value of R, and a greater value of θ, Figure 6.19 (b).This can be expressed mathematically as follows.

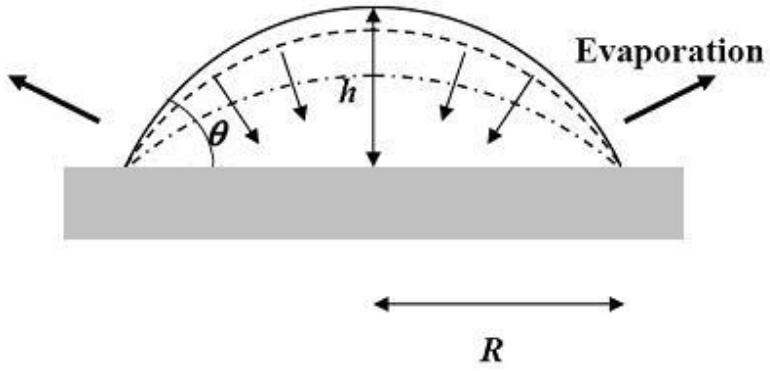

(a)

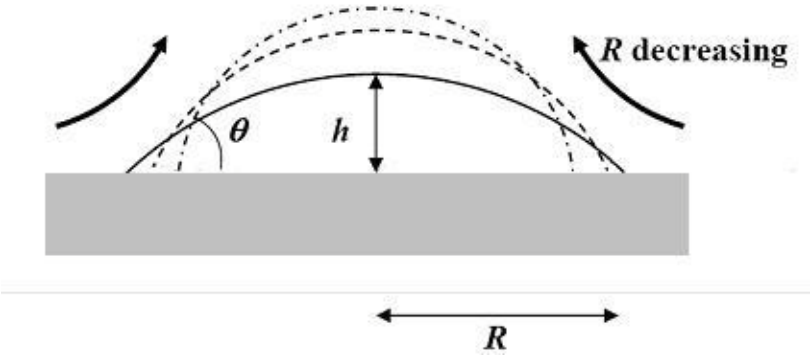

(b)

Figure 6. 19. (a) Representation of pinned droplet. Radius is fixed, both contact angle and drop height decrease in time. (b): Representation of triple line jump. Excess free energy increases until it exceeds the hysteretic energy barrier. At this point the drop de-pins and the contact radius, *R*, is reduced, whilst the contact angle, θ, and drop height, *h*, are both increased.

Assuming gravitational flattening to be negligible, the drop is represented by a spherical cap of contact angle θ and contact radius *R*. Drop volume, *V*, and liquid/vapour surface area, *A*, are given by:

$$V = \frac{\pi R^3}{3} \frac{(1-\cos\theta)^2(2+\cos\theta)}{\sin^3\theta} \tag{6.17},$$

$$A = \frac{2\pi R^2}{(1+\cos\theta)} \tag{6.18}.$$

To within an additive constant, the associated Gibbs free energy, *G*, is given by:

$$G = \gamma A + \pi R^2(\gamma_{SL} - \gamma_{SV}) = \gamma\pi R^2\left[\frac{2}{(1+\cos\theta)} - \cos\theta_o\right] \tag{6.19},$$

where use of Young's equation, (2.6), has been made to replace $(\gamma_{SL}-\gamma_{SV})$ by $-\gamma\cos\theta_o$.

For a given volume, V, equilibrium contact radius, R_o, corresponds to contact angle θ_o. However, if the drop gets out of thermodynamic equilibrium with, let us say, a contact radius $R = R_o+\delta R$ (and therefore a contact angle $\theta_o-\delta\theta$), it will possess *excess* free energy, δG, up and beyond that which it would have in its equilibrium configuration, at the *same* volume. This excess free energy is given by:

$$\delta G = G(R) - G(R_o) = \delta R\left[\frac{dG}{dR}\right]_{R=R_o} + \frac{(\delta R)^2}{2}\left[\frac{d^2G}{dR^2}\right]_{R=R_o} + O\left[(\delta R)^3\right] \qquad (6.20).$$

Being an equilibrium value, at $R = R_o$ (and $\theta = \theta_o$), we have a minimum of free energy, thus $[dG/dR]_{R=Ro}=0$. As a consequence, we need only treat the second order term in equation (6.18) in order to estimate δG. Defining δG per unit length of TL as $\delta\tilde{G}$ ($\delta\tilde{G} = \delta\Gamma/(2\pi P)$), and neglecting 3rd and higher order terms in equation (6.20), we find:

$$\delta\tilde{G} = \frac{\gamma\sin^2\theta_o(2+\cos\theta_o).(\delta R)^2}{2R} \qquad (6.21).$$

During evaporation, free energy excess $\delta\tilde{G}$ increases, if the TL is pinned. Continued evaporation at constant contact radius will increase $\delta\tilde{G}$ until it *just* exceeds a potential energy barrier, U, physical or chemical, for de-pinning. At this moment, the TL will unhook and recede, leading to a smaller value of R and higher value of θ.AN assumption is made that the TL jumps virtually instantaneously (obviating consideration of continued evaporation during the jump), and that this jump is to a new equilibrium value of R_o, corresponding to the recently diminished drop volume (and therefore corresponding to contact angle θ_o again). (To clarify: θ_o is an (assumed) constant of the system solid-liquid-vapour, whereas R_o is the drop contact radius corresponding to θ_o *for a given drop volume*, and will therefore decrease as

evaporation ensues.) Drop height, $h_{(o)}$, and radius, R, are then assumed both to be reduced to conserve the relation $\tan\left[\theta_o / 2\right] = \left[h_{(o)} / R_o\right]$ Also, to facilitate treatment, all motion of the TL is taken to be axisymmetric, although as will be seen below, experimentally there was some asymmetry, presumably due to more effective pinning in some places than others along the TL. This effect, however, should not alter the basic physics of the analysis.

The resulting graphs of R and θ should qualitatively resemble the simplified sketches in Figure 6.20, in which R decreases in steps and θ follows a zigzag pattern. Comparing Figures 6.20 and 6.10, a distinct resemblance is clear. Not only does contact radius, R, decrease for the major part in steps, but within experimental scatter, contact angle, □, decreases and jumps back to an essentially constant value after falling too low during the evaporation with "pinning" stage. The behaviour does seem however a little erratic towards the end of drop lifetime. We write "pinning" in quotes since some drift is clearly obvious in Figure 6.10; a point to which we shall return later.

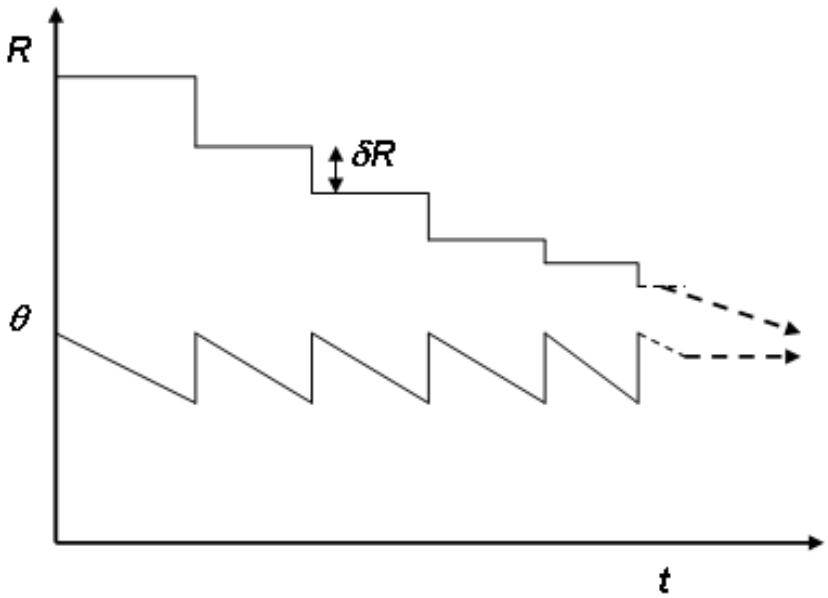

Figure 6. 20. Schematic representation of concomitant stick-slip decrease in contact radius, R, and oscillating behaviour of contact angle, □, as anticipated from reference 29.

With the essential features of the predictions of reference 29 present, some rudimentary analysis can be undertaken. The above theory invokes an excess free energy, $\delta\tilde{G}$, which is taken with reference to a supposed equilibrium state with contact angle θ_o. A value of $44 \pm 2°$ would seem to be a reasonable estimate from Figure 6.10, and corroborated by Figure 6.9. Taking γ to be 22.4 mJm^{-2} at an ambient temperature of 20°C, we may then express the excess free energy (per unit length of TL) at a jump, and therefore the potential energy barrier, *U*, as $14.7(\delta R)^2 / R$ mN (or mJm^{-1}) if lengths are in meters. We can reasonably estimate $(\delta R)^2 / R$ and use this to estimate the energy barrier, *U* from equation (6). We may calculate the mean value of $(\delta R)^2 / R$ as $5.9 \pm 4.0\ x\ 10^{-6}$ m. This leads to U = *ca.* $9 \pm 6\ x\ 10^{-5}$ mN (or mJm^{-1}). Errors are considerable, and so it is clearly wiser simply to say that *U* is of the order 10^{-7} N.

As evoked elsewhere [32], the value of *U*, or $\delta\tilde{G}$ at the jump threshold is probably related to the concept of line tension. Not only are the dimensions the same, but the order of magnitude of the value obtained is consistent with certain results in the literature. They may even possibly be interpreted as manifestations of the same effect. Theoretical predictions of values of line tension are usually in the range of 10^{-12} N to 10^{-10} N [33, 34]. However, certain experimental studies suggest values nearer to 10^{-6} N [33]. The presently obtained value of *U* lies between experimental and predicted values of line tension, although considerably nearer to the former. Is this coincidental, or is line tension intimately connected with the wetting hysteresis free energy barrier?

As may be seen in Figure 6.10, even during the "stick" periods of the stick-slip wetting-evaporation process, contrary to the expectations of reference 29 and the findings of, for example Deegan *et al* [30, 31], there is some TL motion, or drift. The drift distances between jumps are typically of the order of 5 x 10^{-5} m. In Figure 6.11, an image of the solid surface after drop evaporation is presented, clearly showing the nano-particle residues following evaporation. Despite the eccentricity of the evaporation, presumably caused by preferential pinning of the TL on one side; an effect which will be exacerbated by the following accumulation of nano-particle residues, the general effect is for a set of (approximately) circular rings to occur

during evaporation. Geometrical assessment of the photograph and comparison with the results of Figure 6.10 indicates that the rings correspond to the "stick" periods, and the (apparently) clean surface corresponds to the jumps or "slips". Closer inspection also reveals that the rings are constituted of patches of nano-particle agglomerates, orientated radially, and of radial extent of the order of 5 x 10^{-5} m. Therefore, a reasonable conclusion is that the drift of the TL corresponds to the orientation of nano-particles laid down, and their agglomerates building up, during the evaporation process and slow TL motion. It is well-established that evaporation rate is highest near the TL for contact angles much less than 90°.

Hypotheses for the drift behaviour, or "pseudo-pinning" of the TL is all that can be provided at this stage. Two possible effects may explain the slight drift of R during the "stick" period of stick-slip. Firstly, whilst the contact angle is fairly near to its equilibrium value, θ_o, the driving force tending to cause TL recession is low, and pinning can easily be started by a slight, local, surface heterogeneity. This will be only temporary, and if the build-up of nano-particles due to evaporation is only fairly slow, as suggested by the photograph, there may be a continuous, but feeble, pinning effect caused by these nano-particles (self-pinning); the pinning passing from one particle to the next radially, and giving the impression of continuous, but slow, TL motion at the macroscopic scale. Presumably, the orientation of these particles also consumes energy (an entropic effect), which brakes the TL recession. If the drift mechanism is insufficient to maintain the contact angle near to its equilibrium value, which is manifestly the case, as shown in Figure 6.10, then the state of affairs will be attained, at which the imbalance of the overall pinning force (hysteretic energy barrier, U) and the excess of free energy, $\delta\tilde{G}$, described above will prevail and a jump will ensue.

A second possible explanation is that near the triple line, nano-particle concentration build-up increases local viscosity. As mentioned above, it has been shown that a 1.5% concentration of titanium oxide nano-particles in ethylene glycol increases the viscosity by 23%. It is not known what the equivalent modification would be in ethanol, and in addition, this is not a bulk effect in the present context since a small-dimensional zone is being considered, where vapour, nano-particle charged liquid, and substrate are in close proximity, by the very nature of its being a (de)wetting

front. Also, the local concentration of nano-particles will be considerably higher. If such be the case, although the triple line cannot be described as strictly pinned, the much higher local viscosity will lead to high shear forces, or alternatively, reduced flow rate. Concomitantly, evaporation of the drop continues, and when the excess free energy attains a value equivalent to *U* in the simple theory, triple line jump may occur as if the nano-particle deposition were simply acting as a permanent pinning barrier.

Assuming the observed drift is caused by increased effective viscosity, a comparison can be made between (de)wetting rate for pure ethanol and that for ethanol containing nano-particles, under the same conditions, in order to establish an order of magnitude. We have for (de)wetting speed [35]:

$$\frac{dR}{dt} = \dot{R} = \frac{\gamma\theta(t)}{6\eta L}(\cos\theta_0 - \cos\theta(t)) \sim \eta^{-1}. \qquad (6.22),$$

where η is (local) viscosity, $\theta(t)$ is (time-dependent) contact angle, and *L* is essentially a constant (defined as the logarithm of the ratio of a macroscopic distance comparable to *R*, and a microscopic cut-off, itself possibly modified by the local presence of nano-particles) . Adopting suffixes ‘e’ and ‘n’ to represent (pure) ethanol and the nanofluid, and using scaling to compare values of $\dot{R}$ we have:

$$\eta_n = \eta_e \frac{\dot{R}_e}{\dot{R}_n}. \qquad (6.23).$$

Considering the linear, or drift, portions of Figure 6.10, and taking η_e to be1.2 mPas (at 20°C), it is found that for 0.01% nano-particles (initial concentration), that the effective viscosity, η_n, is 1.4 mPas. For 0.1% nano-particles, η_n is 2.1 mPas. This marked increase of values of effective viscosity certainly suggests a *local* concentration increase of nano-particles near the triple line.

6.5 Conclusion

The evaporative behaviour of pure ethanol, and ethanol containing nanoparticles, on three smooth polymeric surfaces of different hydrophobicity has been studied. Initial tests on pure ethanol investigated the evaporative drop lifetime. It was observed that drop lifetime was a function of intrinsic contact angle. The evaporation rate is expected to depend on the contact radius squared, rather linearly, and this seems to be corroborated by interpretation of the results found. Decreasing contact angle leads to shorter drop lifetime, due to exacerbated evaporation near the drop periphery. By using some established equations for evaporation from sessile drops, and applying a few simplifying assumptions, a reasonable agreement between experimental results and theory has been found. Two regimes (at least) exist. For (relatively) large contact angles, little hysteresis is apparent and smooth triple line recession occurs. For small angles, pinning prevents wetting line motion until near drop disappearance. For a given (hypothetical) value of initial contact angle, drop lifetime is shorter and therefore overall evaporation rate higher, for a pinned drop. A possible consequence of this study is application in cooling mechanisms, where more rapid cooling may be expected from liquids possessing small contact angles on the solid in question. Alternatively, by inducing wetting hysteresis, or wetting line pinning (*e.g.* by surface roughening or other treatment) the same effect could be obtained. The introduction of nanoparticles in the ethanol drops was found to significantly alter the evaporative behaviour. Pure ethanol leads to evaporation at virtually constant contact angle and with a constantly decreasing contact radius. This system is thus very near to “ideal”. However, nano-particle addition leads to “stick-slip” behaviour. This is attributed to the effects of accumulation of nano-particle near the triple line, due to advective flow. Analysis of the “slip” behaviour suggests the existence of hysteretic energy barriers to (de)wetting, which may plausibly be compared with line tension effects. The stick behaviour is, however, not “absolute”. Slight “drift”, or triple line recession, occurs. Two possible explanations are proposed. One attributes the effect to a local weak, temporary pinning by a sequence of deposited nano-particles. The other invokes the possibility of locally increased liquid viscosity by the (higher) concentration of nano-particles.

7. Deposit patterns arising from the evaporation of nanofluid drops.

7.1 Introduction

In this chapter the deposit patterns formed via the evaporation of sessile nanofluid drops is investigated. In these experiments water based nanofluids were prepared and investigated. Evaporative behaviour of colloidal suspensions has attracted interest in many diverse areas, such as in biological research where evaporation induces DNA stretching [103] and analysis, and in the formation of crystals [104]. As has been previously discussed, many factors can affect evaporative behaviour, including surface tension gradients (Marangoni effects), internal convection, conduction through the substrate, temperature effects of fluid, substrate, and ambient vapour, mass transfer through diffusion, and various other factors, such as electrostatic attraction between the particles and substrate. As a result a wide variety of observed deposit patterns can be observed, Figure 7.1.

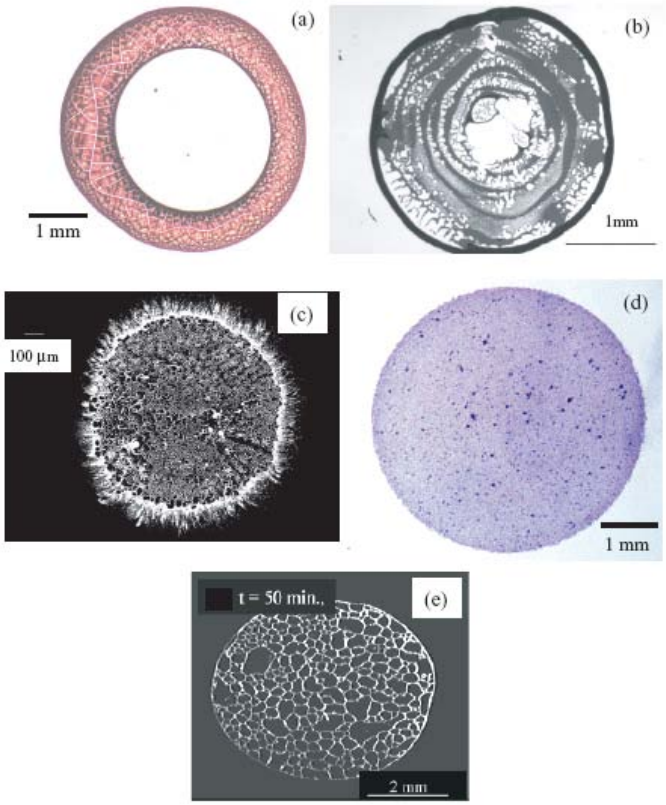

Figure 7. 1. Various deposits left upon complete evaporation of colloidal droplets. A) Ring formation formed by aqueous suspension of 60nm polystyrene spheres (Sommer et al., 2004)[78]. B) Multiple rings formed by aqueous suspension of 1µm polystyrene spheres (Bhardwaj et al, 2009)[105]. C) Fingering pattern formed by IPA suspension of 1µm polystyrene spheres (Bhardwaj et al, 2009)[105]. D) Uniform deposit formed by aqueous suspension of 60nm hydroxyapatite particles (Sommer et al, 2004)[78]. E) Cell patterns formed by aqueous suspension of 1µm polystyrene particles and added surfactants (Truskett and Stebe, 2003)[106].

Blood serum provides an interesting example of how understanding the nature of evaporating drop may be useful. The complex protein stain morphologies left behind from the evaporation of blood serum (plasma) have been shown to exhibit interesting characteristics. Analysis of these stains could prove useful for medical purposes, as it appears likely that the morphology of the final stain is dependent on the original serum composition. As a result, it may be possible to use this phenomenon to aid the diagnosis of illness. Figure 7.2 depicts samples of blood serum taken from people with various ailments.

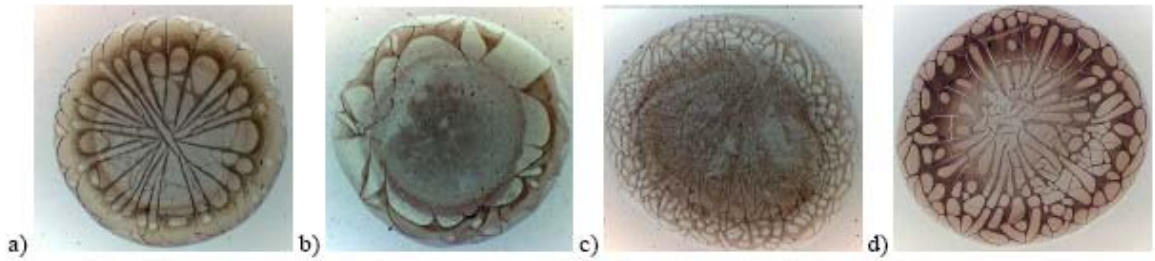

Figure 7. 2. Dried drops of blood serum: a) Practically healthy person. b), c), d) Persons with different kind of diseases.

Understanding the mechanisms of solvent transport is clearly of interest in many similar areas. In this chapter the evaporation kinetics of sessile nanofluid droplets are investigated. The pattern formation observed with the addition of nano-particles is discussed, and results are compared between water based TiO_2 and Al_2O_3 nanofluids of various concentrations on both CYTOP and Teflon substrates. Particular interest is given to the varying behaviour observed when the nanoparticle concentration and the substrate temperature is increased.

7.2 Experimental Setup

The apparatus used in this chapter consisted of a drop dosing unit, including an injection pump with sabre syringe – needle outer diameter of 0.72mm, a camera lens and CCD camera which was used to record the drop profile on the substrate; and a fixed lamp to illuminate the drop profile. The software used to record and analyse the drop evaporation was called FTA 32. This program was designed to allow the controller to vary the recording parameters to adjust for different drop volatilities, and evaporative lifetimes. Images of the experimental setup are shown in figure 7.3.

Figure 7. 3. a)The experimental apparatus: goniometer including computer with FTA-32 software. b) Camera shooting the evaporation of a sessile drop of water on a silicon substrate. Substrate elevated by movable platform and droplet of known volume deposited on substrate by sabre syringe.

The aim of the experiment was to conduct tests of drop evaporation, altering the concentration and substrate temperature to observe any changes in the final deposit patterns which are observed. The substrate temperature was manipulated and controlled by mounting a heater pad onto the underside of an aluminium plate, a thermocouple was then embedded into the plate and linked to a temperature controller, enabling the temperature to be controlled. The substrates used in the experimental tests were then deposited onto the aluminium surface, care was taken to ensure a good contact between the heated aluminium plate and the silicon substrate. A thermal contacting material was used to help improve the contact between the two surfaces.

During an experimental run, the drop profile was recorded for the entire drop lifetime. The resulting images could then be analysed and drop characteristics such as drop volume, evaporation rate, drop height etc could then be obtained. The resulting nanoparticle deposits were then observed using a microscope with a camera attachment, allowing images of the final drop deposits to be taken.

Nanofluids

Water based nanofluids were selected for testing in this chapter. Nanofluids were prepared using Al_2O_3, TiO_2, and Cu nanoparticles and dispersing them in water using the same method as has already been outlined in Chapter 4. Several concentrations of each nanofluid were prepared, 0.5 ,1 ,2 , and 5% by wt.

Substrates

The substrates used in this experiment were silicon based substrates which were coated with a hydrophobic layer of Teflon, these were the same type of substrate which were also used in the stick slip experiments presented in chapter 4 and care was taken to ensure that each substrate was prepared in the same way prior to each individual experimental run.

7.3 Experimental Results

The results presented here are split into two sections. The first section details experimental tests conducted to analyse the effect, if any, of the presence of nano-particles on the overall evaporation of the drop. The second section focuses on the wetting characteristics of the drops and analyses the interesting phenomena which is observed.

7.3.1 Evaporation rate

The experimental equipment used in these tests consisted of a digital micro balance, GR-202 with an accuracy of 10^{-5}g, and accompanying computer and software for analysis. The substrates were placed carefully on the balance and the scale re-set, drops of various volumes ranging from 2mg to 12 mg were then deposited on the substrates and the drop mass was recorded at 10 second intervals. A picture of the set up is depicted in Figure 7.4.

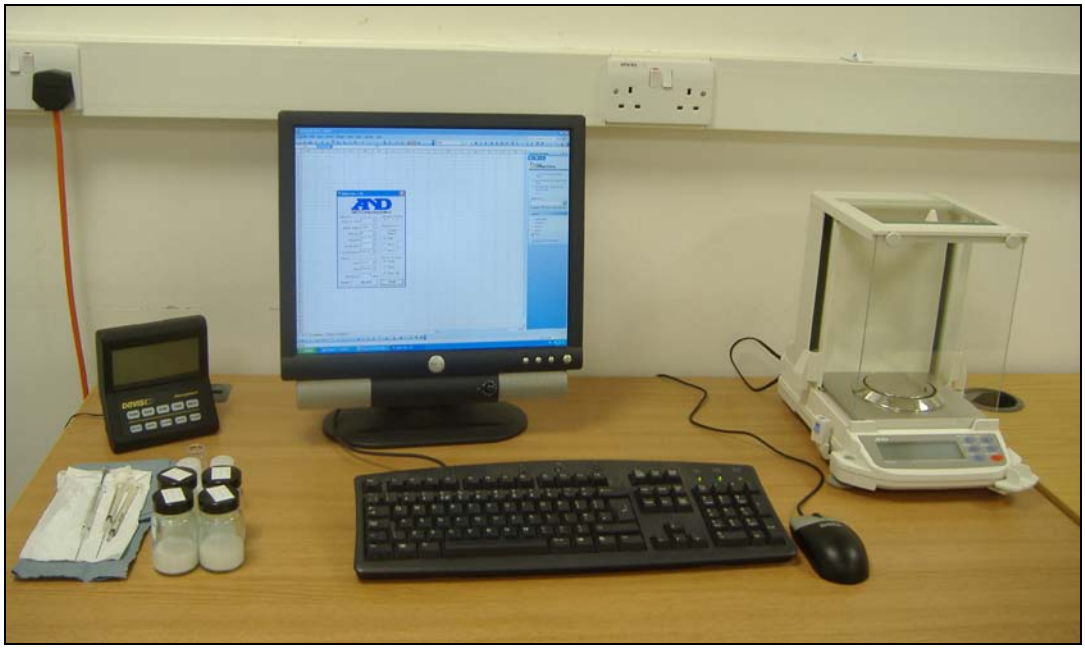

Figure 7. 4. Image depicting the experimental setup for analyzing drop evaporation rate.

7.3.1.1 Humidity

Initial tests investigated the effect of the atmospheric humidity. In order to investigate this, pure water drops were tested at different humidities and a graph was plotted which depicted the evaporation rate as a function of initial drop mass. This graph can be seen in Figure 7.5.

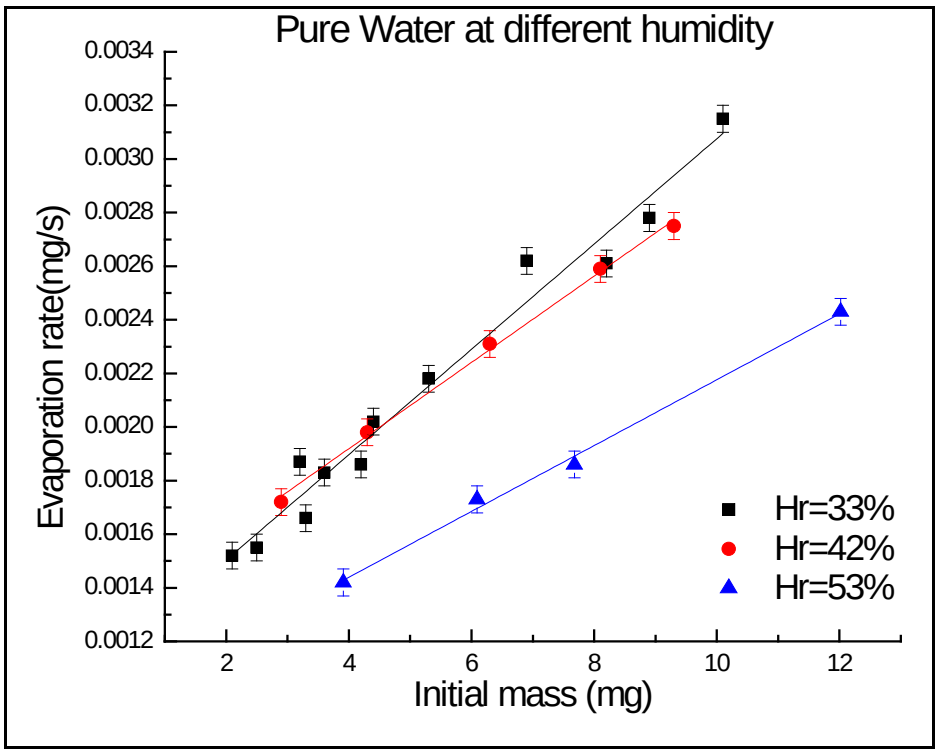

Figure 7. 5. evaporation rate of pure water as a function of initial drop mass.

It appears from the graph that increasing the humidity tends to inhibit the evaporation of the drop, however the trend for the lower two humidities is not so clear. Following this result, care was taken to ensure that all experimental measurements were taken at humidities which were as close as possible. This was achieved primarily by taking several runs together when the atmospheric conditions were similar.

7.3.1.2 Nanoparticle concentration

Next the drops were tested for different nanoparticle concentrations. This was achieved by preparing nanofluid solutions of various concentrations and depositing them in a similar method to the pure water drops. Tests were taken at two distinct humidities, ca 40% and ca 35%. The concentrations of Al2O3-Water nanofluids which were prepared were 0.5%,1%,2%,5% and 10% by wt respectively. The graphs representing the obtained results are shown in Figures 7.6 and 7.7.

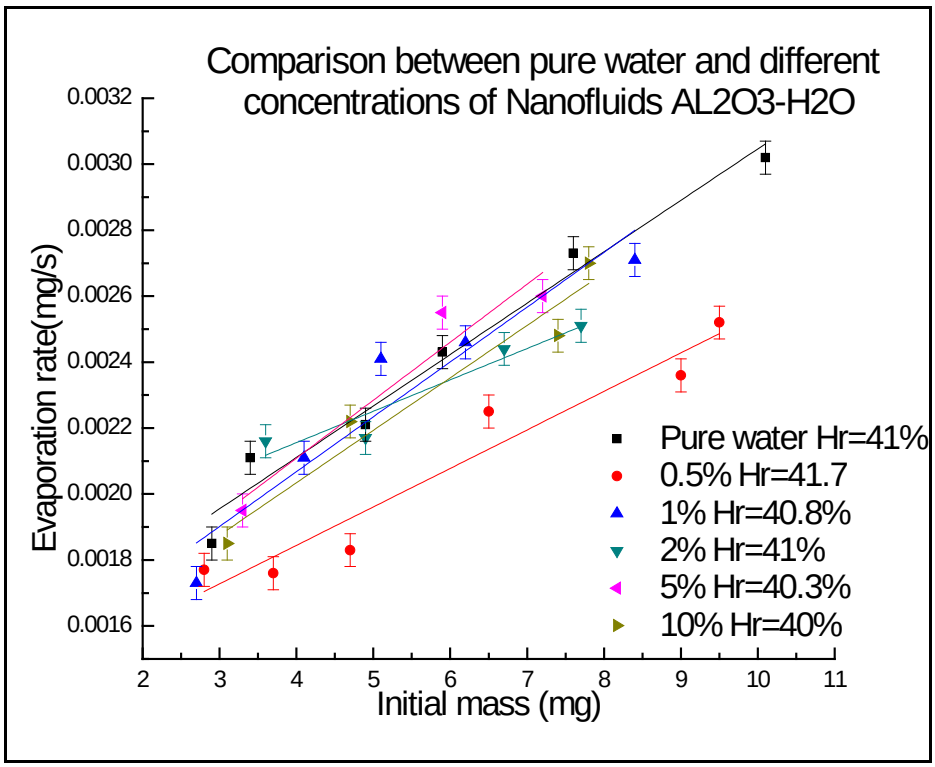

Figure 7. 6 Comparison between pure water and different concentrations of Al_2O_3-water nanofluids.

There appears to be very little discernable difference in evaporation rate as nanoparticle concentration is increased. In most cases the increase in evaporation rate follows a similar linear increase as would be expected from literature, but the affect of nanoparticle addition appears less clear. In figure 7.6 results are presented for the same concentrations evaporating with an atmospheric humidity of ca. 35%.

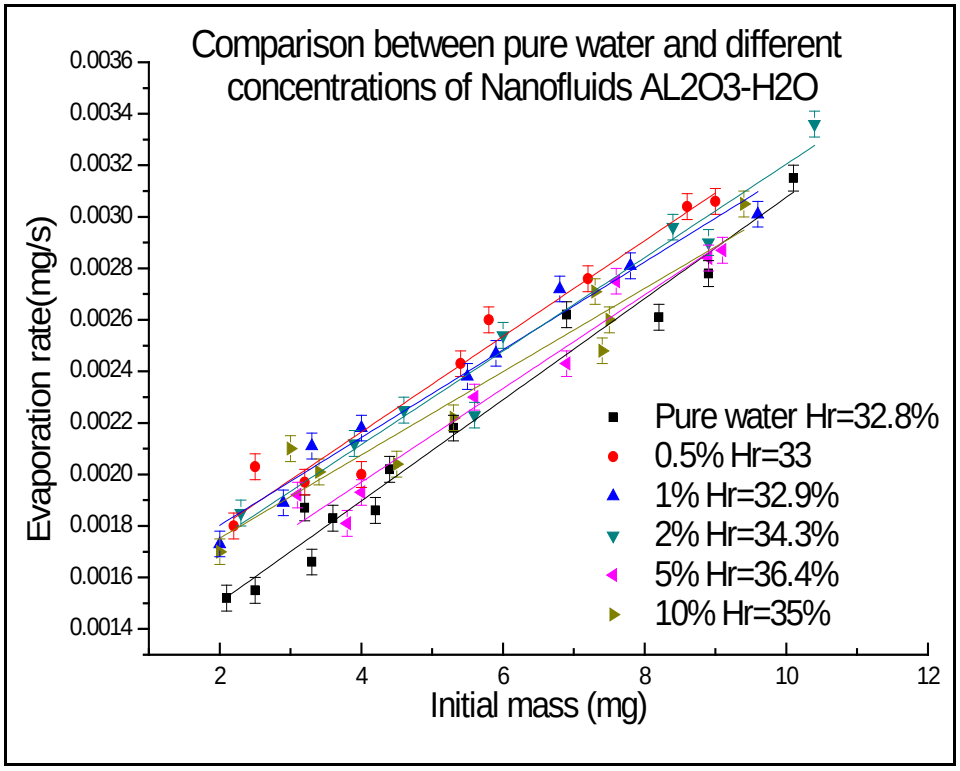

Figure 7.7. Comparison between pure water and different concentrations of Al_2O_3-water nanofluids.

As can be seen in figure 7.7, there is considerable overlap in the evaporation rate for each nanofluid concentration, indicating that particle concentration has little dependence in the overall evaporation rate. Again, the linear increase in evaporation appears to be consistent for most of the samples tested.

7.3.1.3 Nanoparticle composition

Tests were then conducted using alternative nanoparticles to examine the effect of nanofluid composition on the underlying evaporation rate. Tests were conducted for Al_2O_3, TiO_2, and Cu – Water based nanofluids at a concentration of 2% by wt. A graph depicting the results is shown in figure 7.8

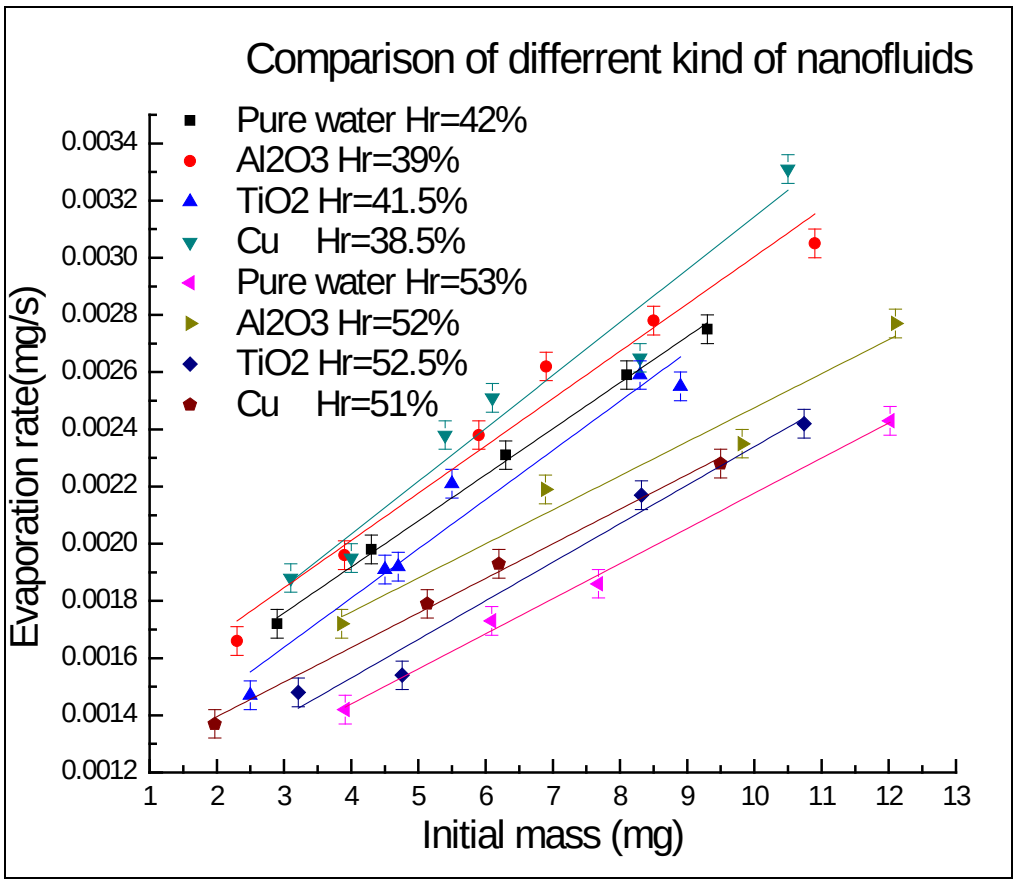

Figure 7.8. Comparison of evaporation rates of varying nanofluid compositions.

From this graph, a distinct shift can be seen for the two sets of tests conducted at different humidities, which is in accordance with the earlier experiments. However, again any perceived increase in evaporation rate between the various materials is unclear.

An attempt was made to characterize the enhancement of evaporation rate at different humidities for both Al_2O_3-Water, and TiO_2-water nanofluids. The enhancement of evaporation rate was compared with the relative enhancement in thermal conductivity which is observed between the two materials. The results are plotted in Figure 7.9. The two black points indicate the evaporation enhancement shown in TiO_2 based nanofluids at two different humidities, the red points show the same data for Al2O3 based nanofluids. The relative enhancement is grearter in the more conductive aluminium oxide nanofluids.

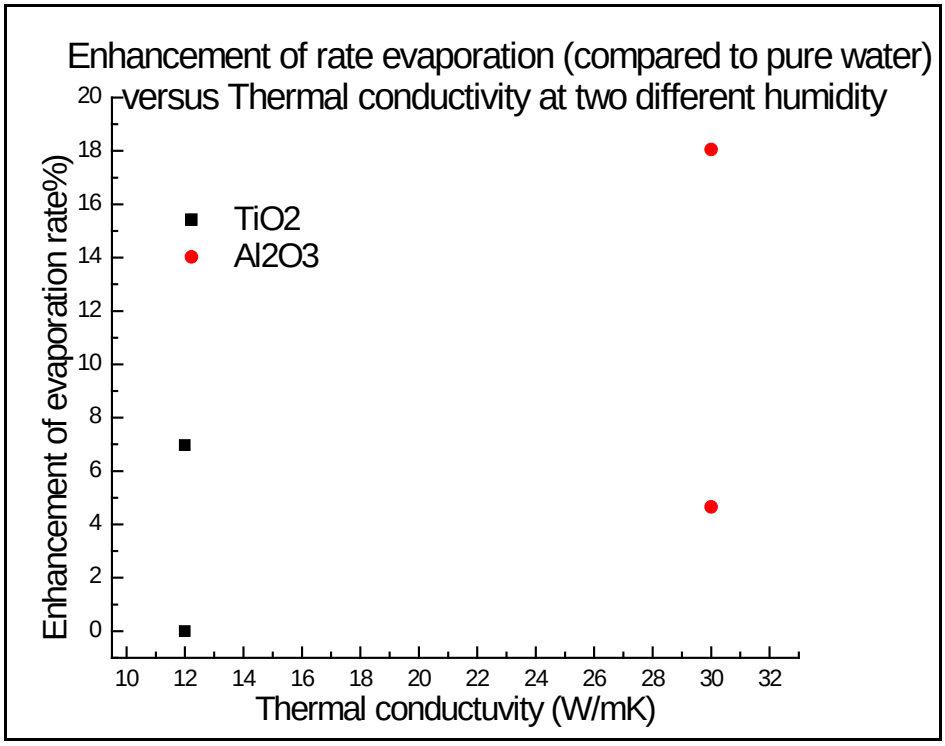

Figure 7.9. Enhancement of evaporations rate vs. thermal conductivity.

7.3.2 Wetting Characteristics

Using the expermintal setup described earlier in the chapter, data was collected for pure water, AL_2O_3-water, and TiO_2-water nanofluids. The bulk of the tests were conducted using Al_2O_3-water nanofluids at concentrations of 0.5%,1%,2%, and 5%, with additional tests being carried out using TiO2-water at concentrations of 0.01% and 0.1%.

7.3.2.1 Temperature Effect

The effect of increasing the substrate temperature on the evaporative behaviour was examined and results are presented in Figure 7.11.

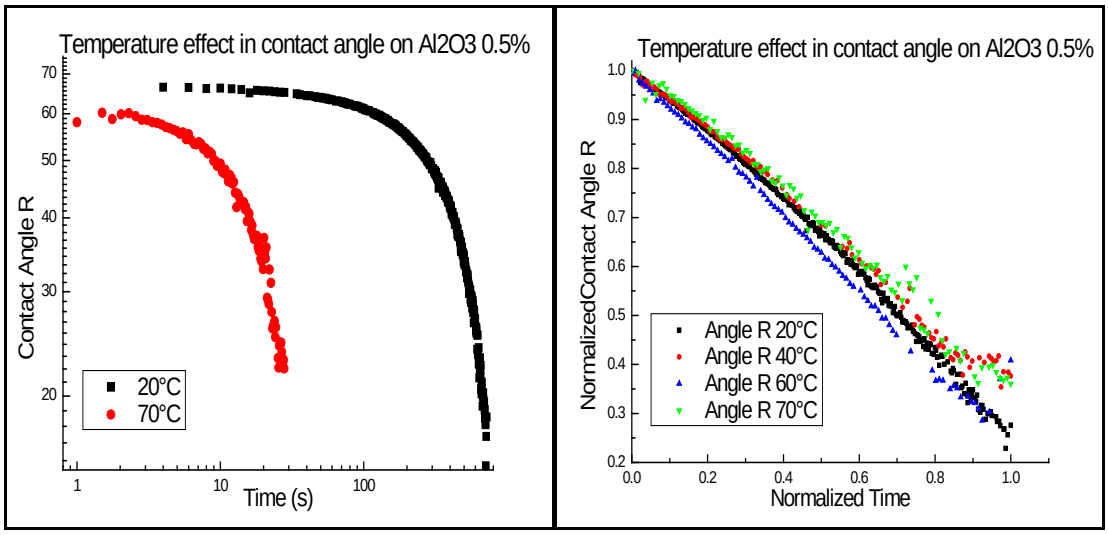

a) **b)**

Figure 7.10. Graphs depicting contact angle behaviour of Al_2O_3-water nanofluids evaporating on heated substrates.

As you would expect, increasing the substrate temperature increases the overall evaporation rate characterised by the red line in Figure 7.10 a). At a lower substrate temperature, the drop contact angle does not change significantly until later in the evaporative process, indicating drop pinning. A normalised graph indicated a similar evaporative trend as temperature is increased.

7.3.2.2 Concentration effect.

The effect of nanoparticle concentration was tested to investigate whether the base temperature played any part in the evaporative process. To allow for small discrepancies in drop volume and base diameter due to the accuracy of the depositing method, normalised graphs are presented depicting the base diameter in time in Figure 7.12.

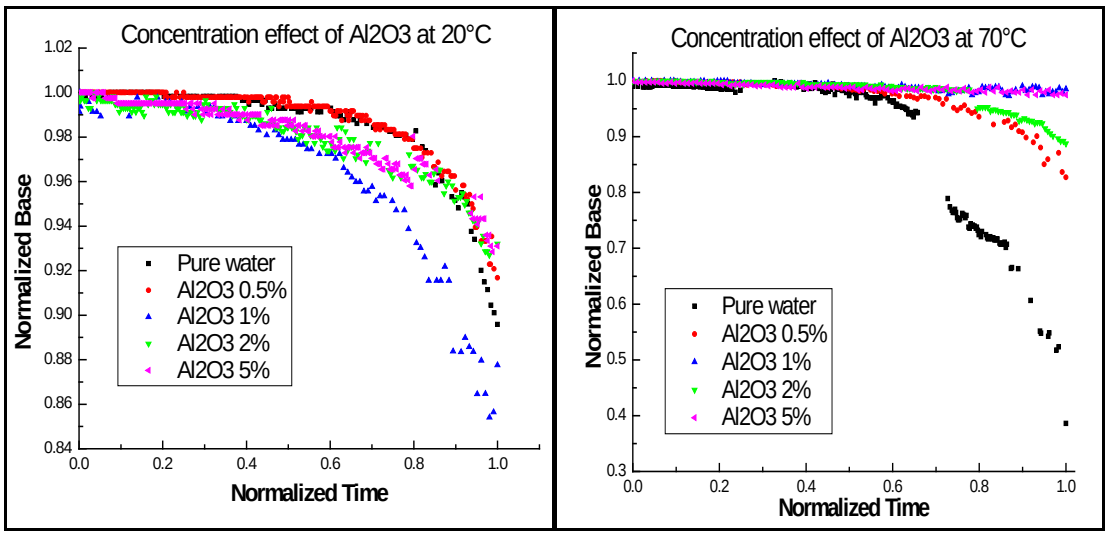

Figure 7.11. Images depicting the normalised base radii in time of various concentrations of Al2O3-Water nanofluid drops evaporating on substrates at two distinct temperatures.

As can be seen from the graphs in figure 7.11, the base radius is shown to decrease more readily on the cooler substrate, indicating contact line slip. In contrast, there is very little slip observed in the drops on the hotter surface, with the exception of water. The pure water trend appears to show a distinct shift in the drop radius, similar to a stick slip drop de-pinning. To examine these results, a closer examination was made of the resultant drop patterns formed upon complete evaporation.

7.3.2.3 Deposit patterns

Images of the various deposit patterns left behind upon total evaporation are presented in Figure 7.13. They depict the various formations that were produced for Al_2O_3-water based nanofluids, and are arranged according to drop concentration and substrate temperature.

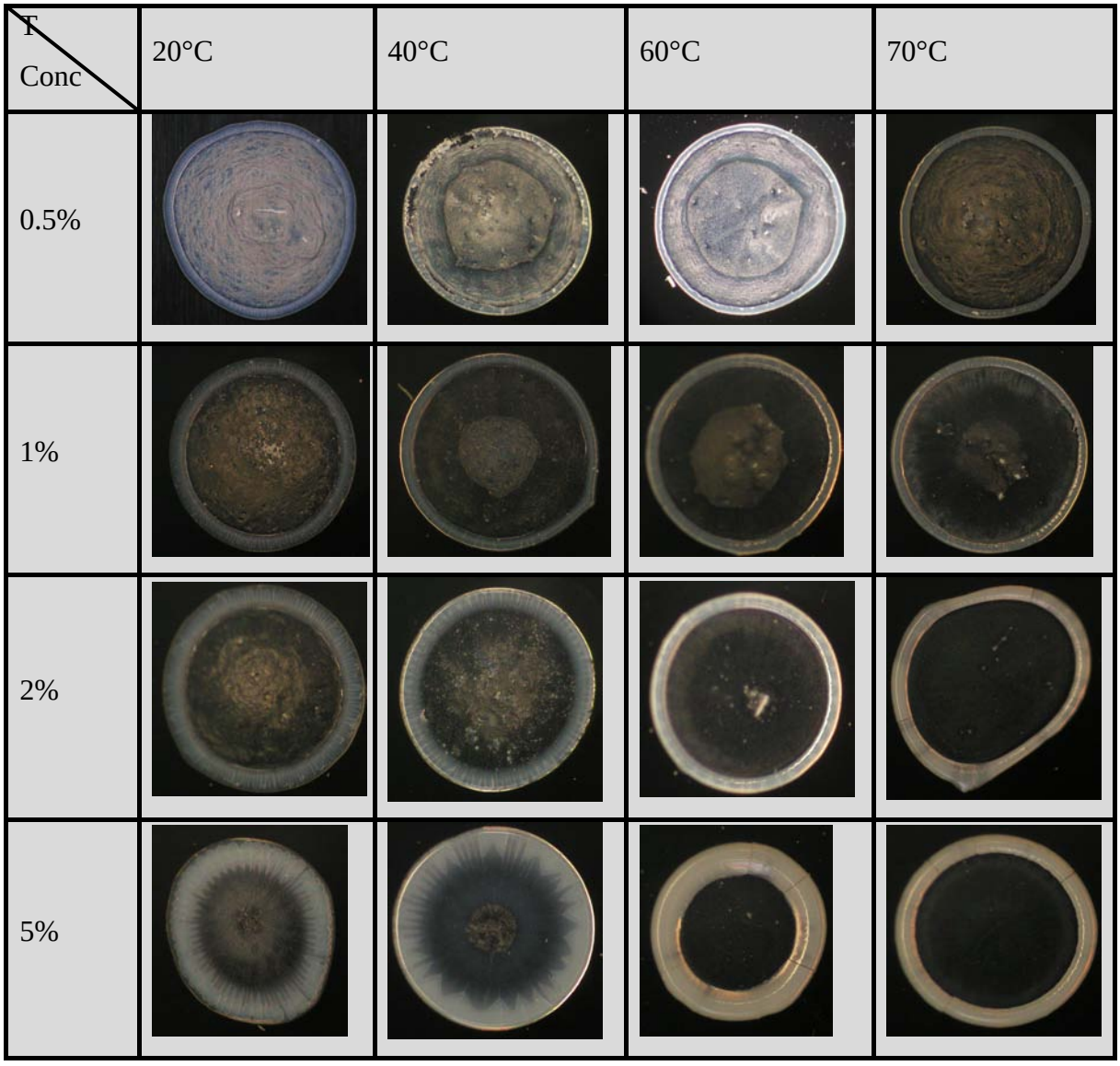

Figure 7.12. Images of nanofluid drop deposits left after the complete evaporation of Al_2O_3-water drops.

An interesting array of deposit formations can be observed. Starting with the most dilute concentration 0.5%, we can see that the deposit pattern leaves a ring of particles around the drop periphery. For all the temperatures tested there also appeared to be a

thin layer of particles covering the base area of the evaporation of the drop. At higher base temperatures an internal ring is observed where there appears to be a lack of particles. This is evident for all the higher substrate temperatures. Increasing the concentration leads to a more distinct ring pattern, increasing the concentration leads to a general increase in the thickness of the contact line ring, this is as would be expected as thee are more particles present in the drop.

Upon close examination of the outer rings, distinct cracking patterns can be seen which appear to have regular dimensions. Increasing the substrate temperature tends to result in more concentrated outer rings, with less particles present in the drop interior. Also, increasing the temperature leads to a general decrease in the dimensions of the observed cracking patterns.

I 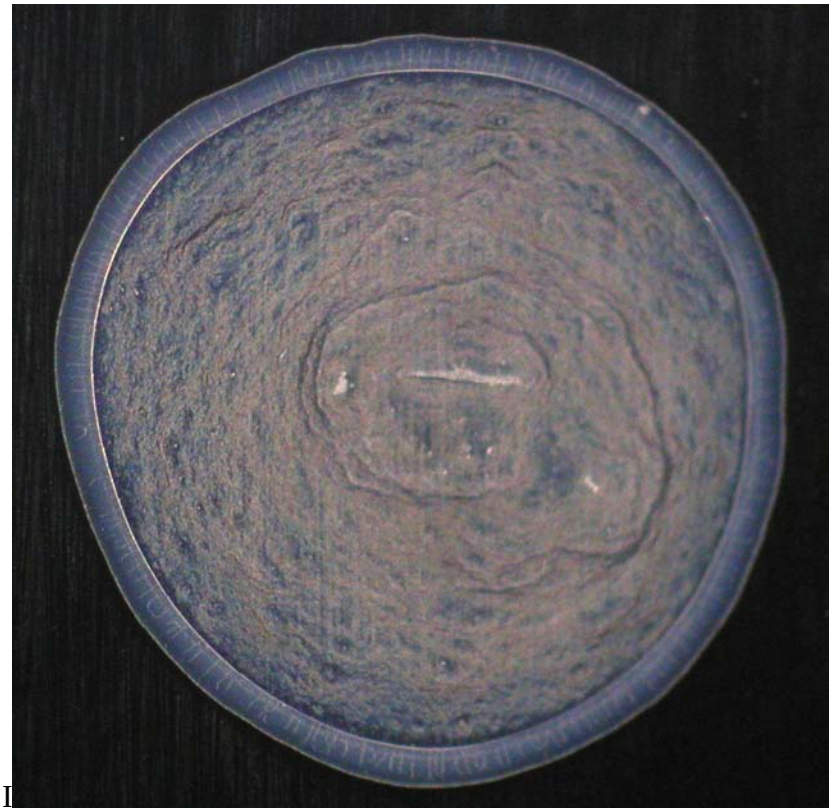

Figure 7.13. Large image depicting the deposit pattern left upon complete evaporation of 0.5% al2O3-Water nanofluid drop on substrate held at 20°C

In Figure 7.14 a larger representation of a drop deposit shown in Figure 7.13 is given. It can be seen that around the periphery of the drop a distinct ring is present, and that

there are regular cracks in the ring which are more or less perpendicular to the contact line. There also appears to be an alignment of the particles present in the interior of the drop, although this is much less pronounced. Figure 7.15 illustrates the evaporative behaviour which was recorded to during the evaporation of the drop which resulted in the deposit shown in Figure 7.14.

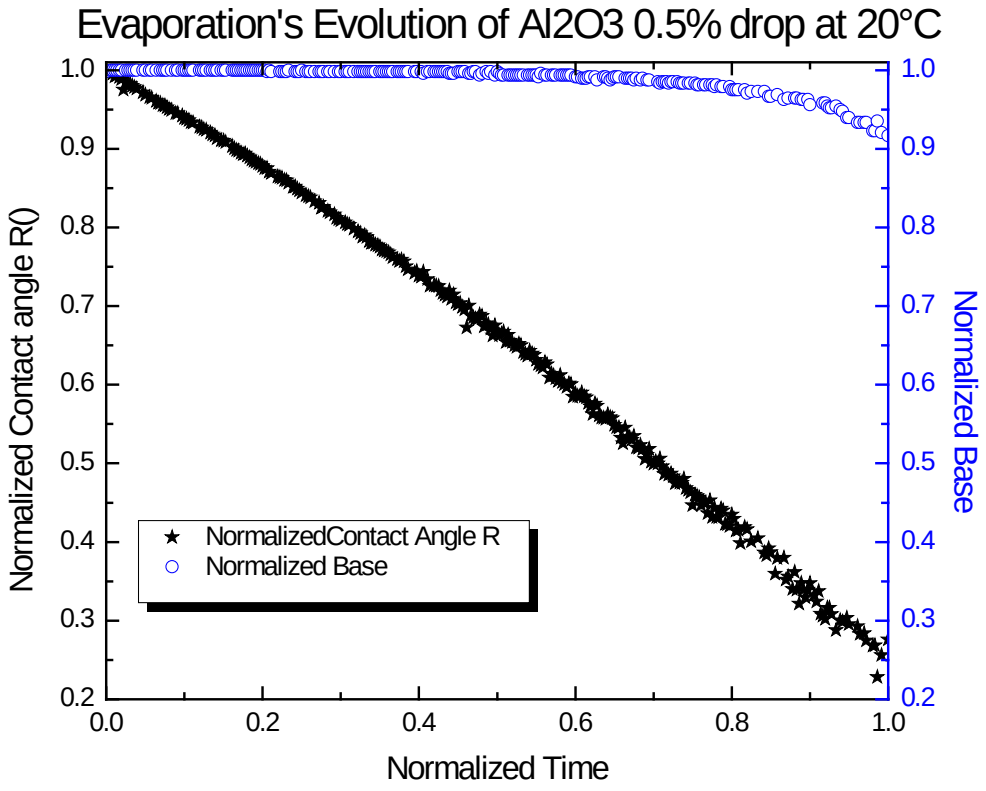

Figure 7.14. Normalised contact angle and base vs. time for the drop depicted in Figure 7.14.

It can be seen that the drop is essentially pinned for a large proportion of the drop lifetime, with an element of slip evidenced later in the evaporative process. A slight shift in the contact angle is observed during the slip stage of evaporation.

Examining the same concentration drop evaporating on a substrate at 60°C, shown in Figure 7.16 we can see some interesting behavioural differences.

Figure 7.15. Large image depicting the deposit pattern left upon complete evaporation of 0.5% al2O3-Water nanofluid drop on substrate held at 60°C

The outer ring appears to be denser, with less cracking visible. It may be that the cracking is thinner and more regular, resulting in less definition in the presented image. Distinct layering can again be observed in the internal base of the deposit with what appears to be small regular layers of particles being formed on the surface. A distinct internal ring is also shown, which is likely the result the final stage of evaporation after the drop has begun to recede. A figure corresponding to the evaporative behaviour is presented in Figure 7.17. We can see from this figure that there is a greater degree of slip shown in the base diameter in time.

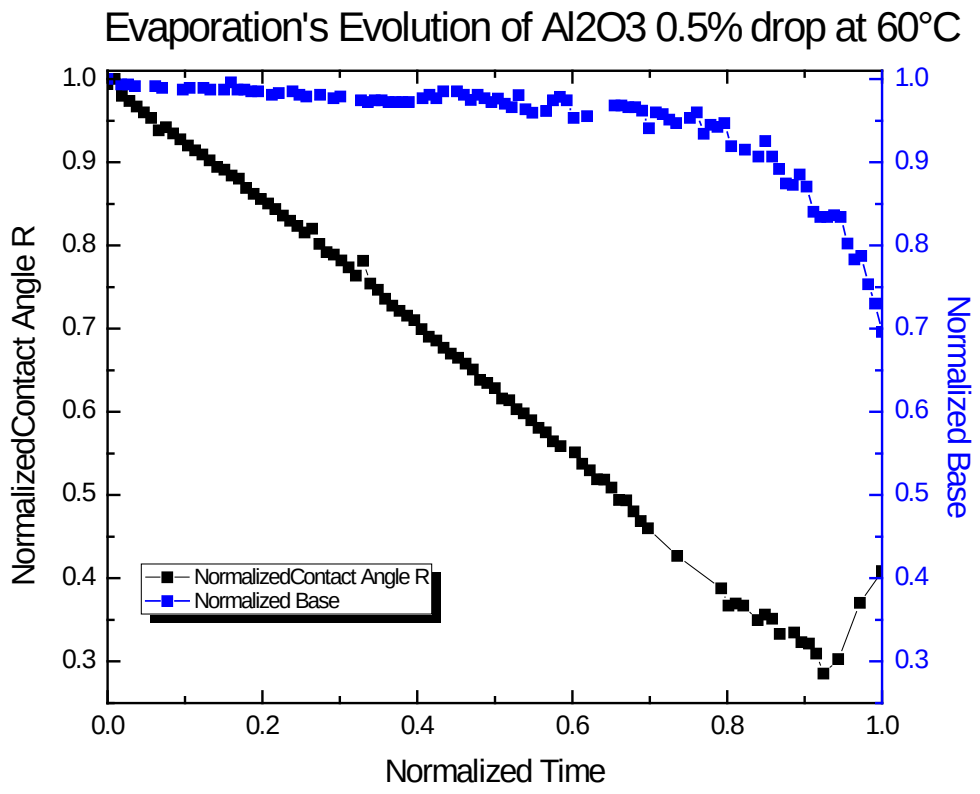

Figure 7.16. Normalised contact angle and base vs. time for the drop depicted in Figure 7.16.

Two more images are going to be presented, this time depicting a higher concentration of 5% Al2O3 particles. The first image is taken from a drop evaporating on a substrate at 20°C. This image clearly shows the regular cracking patterns which are present around the drop periphery. The patterns are reminiscent of cell like patterns, with regular cell sizes. It appears that the concentration of the particles is condensed into spoke like 'tails' which progress from the centre of the drop to the drop periphery. Thin lines of particles can be seen which are aligned perpendicularly to the drop contact line.

Figure 7.17. Large image depicting the deposit pattern left upon complete evaporation of 5% al2O3-Water nanofluid drop on substrate held at 20°C

To provide a direct comparison of the substrate temperature an image depicting the evaporative pattern observed at 40°C is presented in figure 7.19. Compared to the image in figure 7.18, the relative cell size has grown with thick regular cells present. Interestingly very angular saw-toothed patterns are seen on the inner edge of the contact line ring. Again feint thin lines of particles can be seen aligned perpendicular to the drop contact line. There also appears to be areas of the contact line ring where the cell sizes are less than the rest. This may be indicative of an increased area of droplet flow in this specific area.

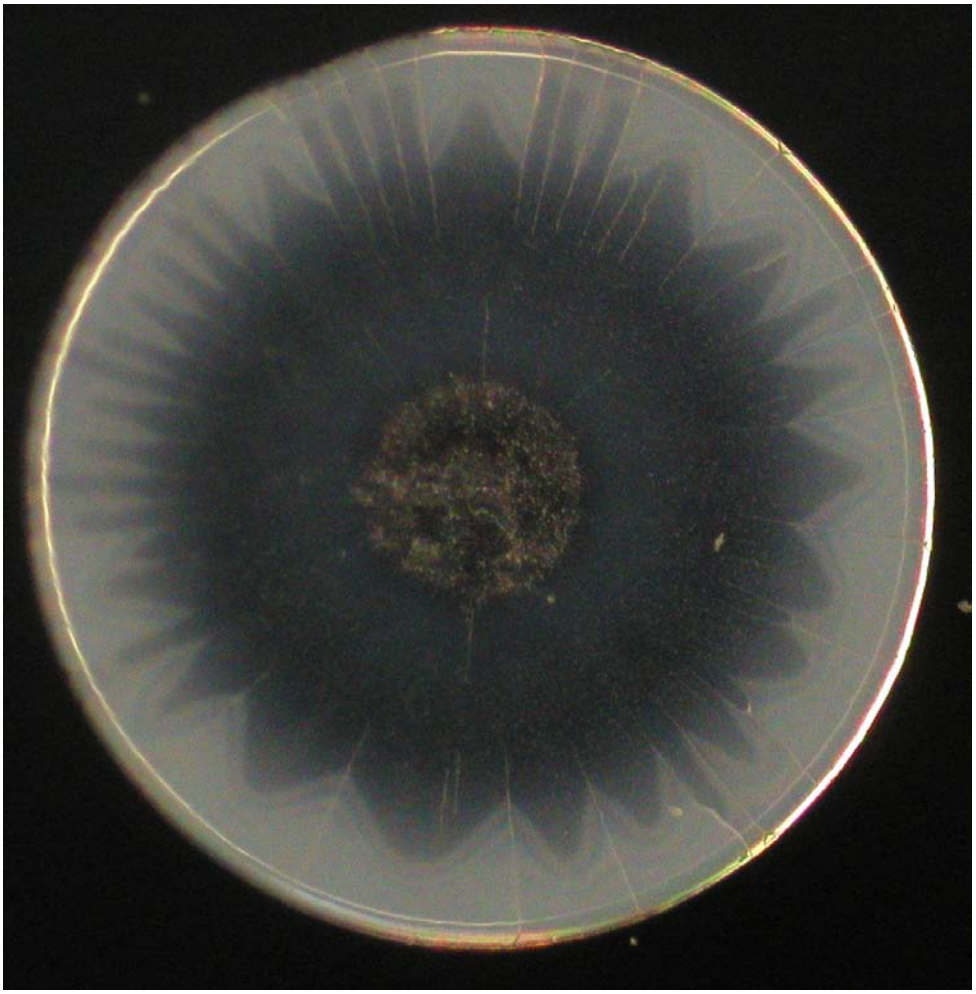

Figure 7.18. Large image depicting the deposit pattern left upon complete evaporation of 5% al2O3-Water nanofluid drop on substrate held at 40°C

At these higher concentrations the drop is essentially pinned for almost all the drop lifetime. Images depicting the normalised base and contact angle vs normalised time are shown in Figures 7.20 and 7.21. There appears to be more scatter present on the contact angle behaviour of these drops. This is probably due to the higher concentrations and resulting deformation of the contact line due to nanoparticle build up.

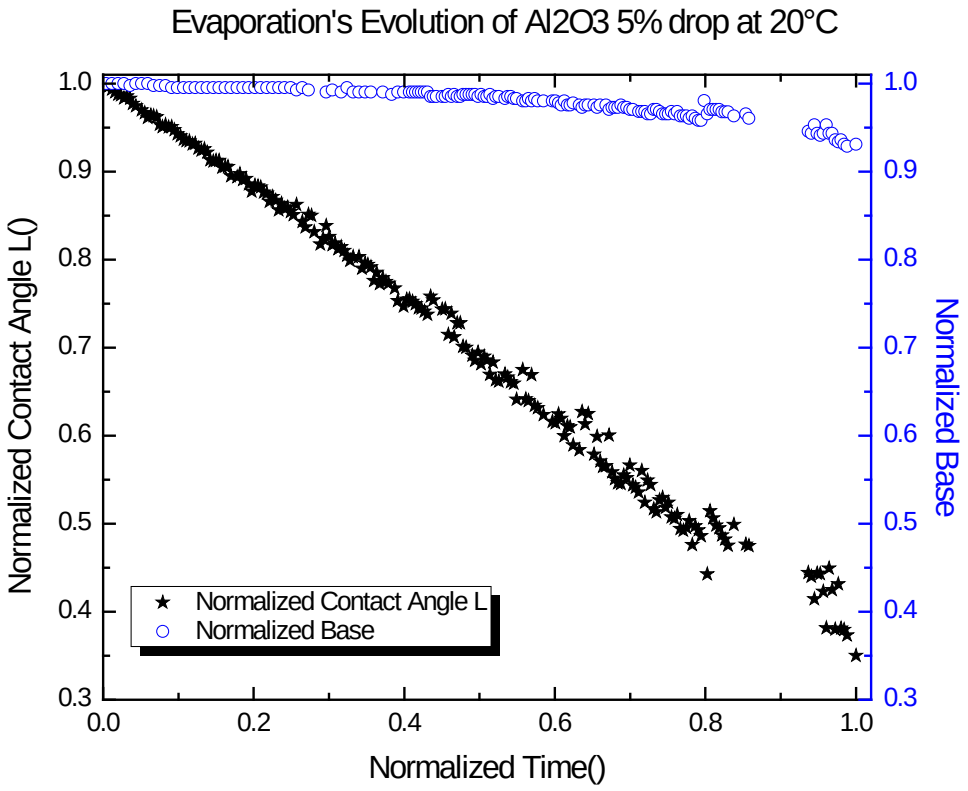

Figure 7.19. Normalised contact angle and base vs. time for the drop depicted in Figure 7.19.

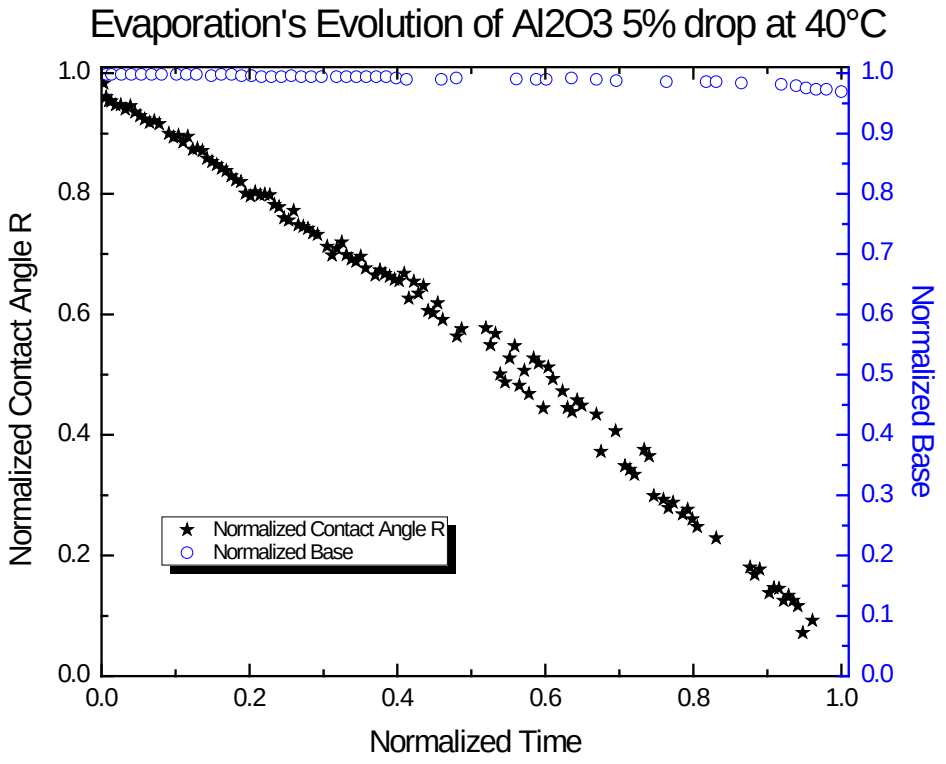

Figure 7.20. Normalised contact angle and base vs. time for the drop depicted in Figure 7.20.

7.4 Discussion

The results obtained in this chapter provide an interesting insight into the evaporative behaviour of sessile drops of nanofluids. The addition of varying concentrations of particles to the bulk fluid results in some interesting phenomena.

Initial tests using a mass balance indicated that particle addition did not seem to appreciably alter the overall evaporation rate for the materials which were tested. The general trend of linearly increasing evaporation rate vs drop radius is well established and is clearly seen in the presented results. In contrast, the atmospheric humidity was shown to alter the observed evaporation rate, with a higher humidity leading to a corresponding decrease in the evaporative process in time. As a result, care was taken to prepare and conduct experiments at consistent evaporation rates. Increasing particle concentration was found to increase the pinning of the drops, this is in agreement with previously published work, and also the tests undertaken on stick slip data in chapter 6. Elements of contact line de-pinning are also observed at lower particle concentrations.

The particle deposits formed upon complete evaporation appear to depend on concentration and substrate temperature to a certain extent. Many distinct features can be observed in these deposits. The results depicted for lower substrate temperatures appear to show a concentrated ring of particles around the drop periphery, with particles present over the bulk of the deposit area. Close inspection of this area indicates that micro-pinning is present, this is characterised by the alignment of particles in very thin lines running approximately parallel to the contact line. At higher substrate temperatures a strong degree of pinning is observed, and consequently thick dense particulate rings are present, with very little particles present in the interior. This can be attributed to an increased rate of evaporation, leading to increased rate of liquid loss at the drop contact line, and consequently an increased flow of liquid (and particles) to the contact line to replenish the evaporated material.

The interesting cellular structures that are observed appear to be regular in nature. The cellular structures were more pronounced in higher particle concentration drops. It is clear that there is a relation between the patterns formed and nanoparticle

concentration. A recent investigation by the university of Edinburgh studied similar nanofluid drops evaporating in an environment where the surrounding temperature was controlled using an oven. The results from this investigation show distinct similarities with the work conducted in this chapter, especially with the formation of the cellular patterns. Typical results are shown in figure 7.20

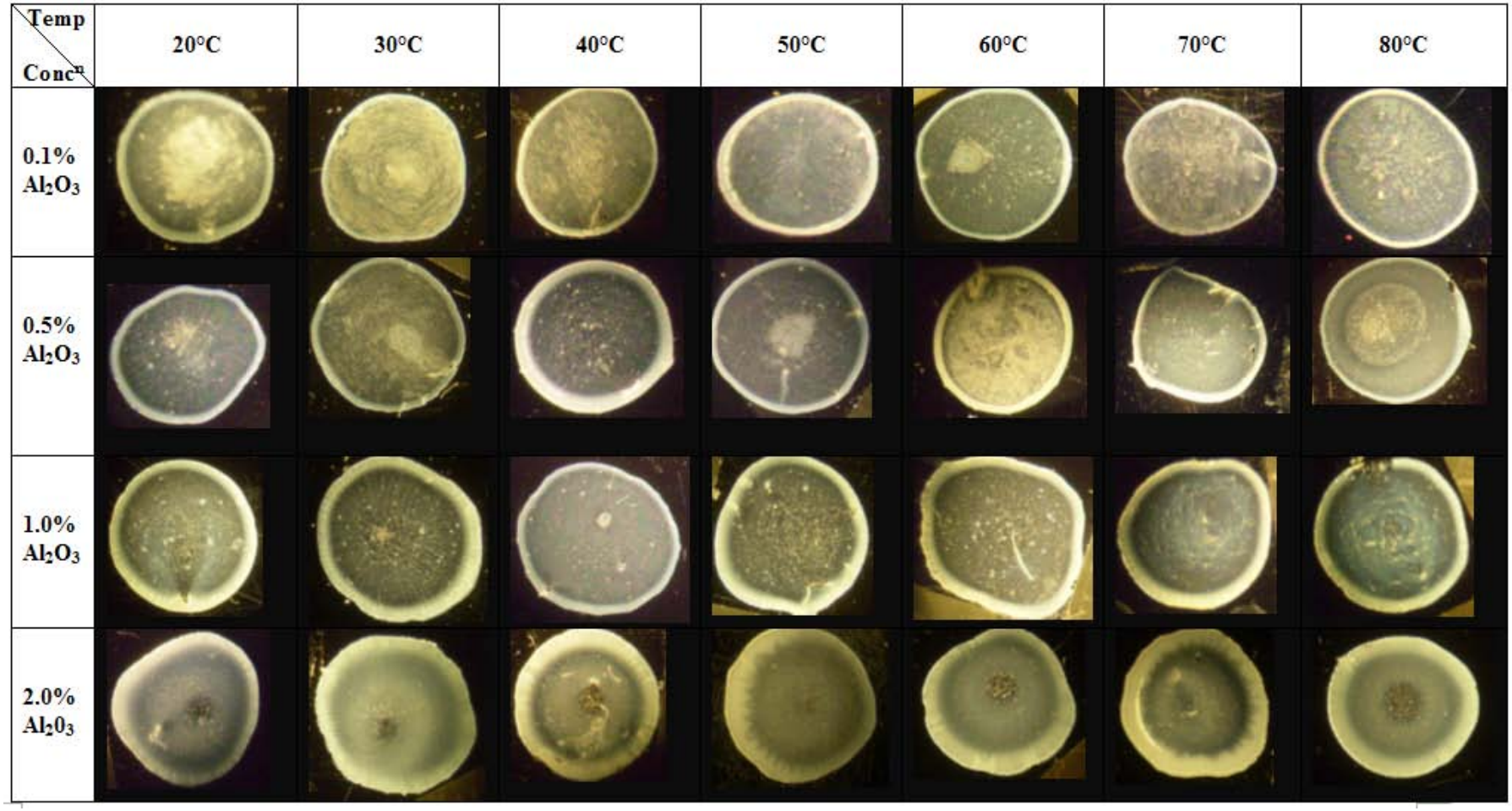

Figure 7.21: Examination of the evaporation of droplets of aluminium oxide based nanofluids of 0. 1%, 0.5%, 1% and 2% concentration and how temperature affected pattern formation.

From the results depicted in Figure 7.20 very similar behaviour to that observed in the earlier tests is shown. The presence of distinct thermal cells is shown, as well as an increase in the outer ring thickness as particle concentration is increased. In these tests there was no way to isolate the surrounding vapour phase, and hence the substrate is also heated during the experimental runs. It would be interesting to observe the evaporative process when just the ambient vapour is heated, however this is problematic to achieve experimentally.

7.5 Conclusions

This investigation focussed primarily on the evaporative behaviour of nanofluids of varying concentrations evaporating on a heated substrate and the resultant particle deposits formed as a result. Results indicate that there is no appreciable change in evaporation rate with increasing particle concentration for the particle concentrations which were tested. In contrast atmospheric humidity was found to alter the evaporation rate. The enhancement shown may be correlated to the increased thermal conductivity of the particles introduced, however at this stage this is merely a possible suggestion and needs much further investigation.

Increasing the particle concentration and substrate temperature is found to lead to greater pinning of the contact line, this is in agreement with the stick slip experiments conducted in chapter 6, and also agrees with previous published work. Increasing the concentration was found to increase the thickness of the contact line deposit, and was found to enhance the presence of interesting patterns. Multiple concentric rings, radial lines, and cellular cracking patterns have all been observed upon complete evaporation. The distinct presence and formation of these patterns appears to be both particle and substrate temperature dependent.

8. Final conclusions and future work

The results obtained in this project provide an interesting insight into the complex behaviour of evaporating drops of both pure fluids, and of fluids containing nanoparticles.

It has been shown that thermal fluctuations are present in the evaporation of volatile sessile drops of methanol, ethanol, and FC 72. The nature of the observed thermal behaviour is liquid dependent, with similar behaviour observed for methanol and ethanol. In these liquids spoke like radial waves are present which rotate around the drop as evaporation progresses. The fluctuations are more numerous and appear to rotate faster in the more volatile methanol drops. In contrast, FC-72 appears to show a different thermal behaviour when studied using IR- thermography. In FC-72, there appears to be cellular thermal fluctuations which emanate from the drop centre and migrate to the drop periphery during evaporation. It was observed that the magnitude of the temperature gradients varied as evaporation progressed. A stability analysis of the observed results was conducted using the normal deformation of the drop surface resulting from a combined Marangoni instability carried by the time dependent regression motion due to evaporation. Trial functions were used to reproduce the patterns observed experimentally. The presence of these interesting fluctuations has not previously been reported, and understanding the physical mechanisms which underpin their appearance is useful for future research on this topic.

In chapters six and seven, the evaporative behaviour of pure liquids and liquids with nanoparticles suspended in the bulk fluid were investigated. In chapter six the behaviour of pure ethanol, and ethanol containing nanoparticles, on three smooth polymeric surfaces of different hydrophobicity was investigated. .It was observed that drop lifetime was a function of intrinsic contact angle. Drops with low initial contact angles were shown to pin to the various substrates which were tested for the bulk of the evaporative lifetime. In contrast drops with larger initial contact angles were more inclined to de-pin leading to a stick slip hysterisis effect during evaporation. As the initial contact angle increases the tendency towards constant contact angle evaporation is increased. A possible consequence of this study is application in cooling mechanisms, where more rapid cooling may be expected from liquids

possessing small contact angles on the solid in question. Alternatively, by inducing wetting hysteresis, or wetting line pinning (*e.g*. by surface roughening or other treatment) the same effect could be obtained. The introduction of nanoparticles in the ethanol drops was found to significantly alter the evaporative behaviour. Pure ethanol leads to evaporation at virtually constant contact angle and with a constantly decreasing contact radius. This system is thus very near to "ideal". However, nano-particle addition leads to "stick-slip" behaviour. This is attributed to the effects of accumulation of nano-particle near the triple line, due to advective flow. Analysis of the "slip" behaviour suggests the existence of hysteretic energy barriers to (de)wetting, which may plausibly be compared with line tension effects. The stick behaviour is, however, not "absolute". Slight "drift", or triple line recession, occurs. Two possible explanations are proposed. One attributes the effect to a local weak, temporary pinning by a sequence of deposited nano-particles. The other invokes the possibility of locally increased liquid viscosity by the (higher) concentration of nano-particles.

The results obtained in chapter seven show that when a colloidal droplet evaporates, the resulting particle deposits exhibit pattern forming properties. The deposit patterns contained various characteristics, such as concentrated particle rings which form at the drop periphery, spoke like particle concentrations which are aligned radially and cellular like cracking patterns indicating complex evaporative behaviour. The appearance of the deposit patterns could be controlled to an extent by altering various factors such as substrate temperature, particle concentration, substrate material and base liquid. Knowledge of how nanofluids behave is important in many areas where two phase processes occur. Increasing the particle concentration and substrate temperature was found to lead to greater pinning of the contact line, this is in agreement with the stick slip experiments conducted in chapter 6, and also agrees with previous published work. Increasing the concentration was found to increase the thickness of the contact line deposit, and was found to enhance the presence of interesting patterns. The distinct presence and formation of these patterns appears to be both particle and substrate temperature dependent.

The results presented in this thesis provide an insight into the various interesting behaviour which occurs in the evaporation of both pure volatile liquids and

nanofluids. In addition, many interesting routes for future research have become apparent as a result of this thesis. Techniques such as PIV may prove useful to gain an underlying understanding of the internal flow phenomena, and this combined with IR measurements may be able to show more conclusively how the thermal behaviour affects the resulting flow and vice versa. Another interesting experiment would be to investigate via IR thermography the nanofluids themselves to see how much the addition of the particles alters the behaviour. There is scope for much further investigation into many aspects of this work, with extending the research into the interfacial phenomena to include more liquids and surfaces, testing more nanofluids and concentrations on the various substrates, and manipulating the deposit patterns via the alteration of various parameters such as substrate temperature all of possible interest.

References.

1. Eastman, J.A., et al., *Anomalously increased effective thermal conductivities of ethylene glycol-based nanofluids containing copper nanoparticles.* Applied Physics Letters, 2001. **78**(6): p. 718-720.
2. You, S.M., J.H. Kim, and K.H. Kim, *Effect of nanoparticles on critical heat flux of water in pool boiling heat transfer.* Applied Physics Letters, 2003. **83**(16): p. 3374-3376.
3. de Gennes, P.G., *Wetting: statics and dynamics.* Reviews of Modern Physics, 1985. **57**(3): p. 827.
4. Birdi, K.S., D.T. Vu, and A. Winter, *A study of the evaporation rates of small water drops placed on a solid surface.* The Journal of Physical Chemistry, 1989. **93**(9): p. 3702-3703.
5. Bourges-Monnier, C. and M.E.R. Shanahan, *Influence of Evaporation on Contact Angle.* Langmuir, 1995. **11**(7): p. 2820-2829.
6. Hu, H. and R.G. Larson, *Analysis of the Microfluid Flow in an Evaporating Sessile Droplet.* Langmuir, 2005. **21**(9): p. 3963-3971.
7. Picknett, R.G. and R. Bexon, *The evaporation of sessile or pendant drops in still air.* Journal of Colloid and Interface Science, 1977. **61**(2): p. 336-350.
8. Wenzel, R.N., *Surface Roughness and Contact Angle.* The Journal of Physical and Colloid Chemistry, 1949. **53**(9): p. 1466-1467.
9. David, S., K. Sefiane, and L. Tadrist, *Experimental investigation of the effect of thermal properties of the substrate in the wetting and evaporation of sessile drops.* Colloids and Surfaces A: Physicochemical and Engineering Aspects, 2007. **298**(1-2): p. 108-114.
10. Deegan, R.D., et al., *Contact line deposits in an evaporating drop.* Physical Review E, 2000. **62**(1): p. 756.
11. Erbil, H.Y., G. McHale, and M.I. Newton, *Drop Evaporation on Solid Surfaces:â€‰ Constant Contact Angle Mode.* Langmuir, 2002. **18**(7): p. 2636-2641.
12. Erbil, H.Y. and R.A. Meric, *Evaporation of Sessile Drops on Polymer Surfaces: Ellipsoidal Cap Geometry.* The Journal of Physical Chemistry B, 1997. **101**(35): p. 6867-6873.
13. Fischer, B.J., *Particle Convection in an Evaporating Colloidal Droplet.* Langmuir, 2001. **18**(1): p. 60-67.
14. Hu, H. and R.G. Larson, *Analysis of the Effects of Marangoni Stresses on the Microflow in an Evaporating Sessile Droplet.* Langmuir, 2005. **21**(9): p. 3972-3980.
15. Panwar, A.K., S.K. Barthwal, and S. Ray, *Effect of evaporation on the contact angle of a sessile drop on solid substrates.* Journal of Adhesion Science and Technology, 2003. **17**: p. 1321-1329.
16. Parisse, F. and C. Allain, *Drying of Colloidal Suspension Droplets:â€‰ Experimental Study and Profile Renormalization.* Langmuir, 1997. **13**(14): p. 3598-3602.
17. Sefiane, K., L. Tadrist, and M. Douglas, *Experimental study of evaporating water-ethanol mixture sessile drop: influence of concentration.* International Journal of Heat and Mass Transfer, 2003. **46**(23): p. 4527-4534.

18. Wachters, L.H.J. and N.A.J. Westerling, *The heat transfer from a hot wall to impinging water drops in the spheroidal state.* Chemical Engineering Science, 1966. **21**(11): p. 1047-1056.
19. Cachile, M., et al., *Evaporating Droplets.* Langmuir, 2002. **18**(21): p. 8070-8078.
20. Dugas, V., J.r.m. Broutin, and E. Souteyrand, *Droplet Evaporation Study Applied to DNA Chip Manufacturing.* Langmuir, 2005. **21**(20): p. 9130-9136.
21. Dunn, G.J., et al., *A mathematical model for the evaporation of a thin sessile liquid droplet: Comparison between experiment and theory.* Colloids and Surfaces A: Physicochemical and Engineering Aspects, 2008. **323**(1-3): p. 50-55.
22. Poulard, C. and et al., *Diffusion-driven evaporation of sessile drops.* Journal of Physics: Condensed Matter, 2005. **17**(49): p. S4213.
23. Widjaja, E. and M.T. Harris, *Particle deposition study during sessile drop evaporation.* AIChE Journal, 2008. **54**(9): p. 2250-2260.
24. Zhang, X., et al., *Evaporation of Sessile Water Droplets on Superhydrophobic Natural Lotus and Biomimetic Polymer Surfaces.* ChemPhysChem, 2006. **7**(10): p. 2067-2070.
25. Rajneesh, B. and et al., *Pattern formation during the evaporation of a colloidal nanoliter drop: a numerical and experimental study.* New Journal of Physics, 2009. **11**(7): p. 075020.
26. Maheshwari, S., et al., *Coupling Between Precipitation and Contact-Line Dynamics: Multiring Stains and Stick-Slip Motion.* Physical Review Letters, 2008. **100**(4): p. 044503.
27. Sommer, A.P., M. Ben-Moshe, and S. Magdassi, *Size-Discriminative Self-Assembly of Nanospheres in Evaporating Drops.* The Journal of Physical Chemistry B, 2003. **108**(1): p. 8-10.
28. Motte, L., F. Billoudet, and M.P. Pileni, *Self-Assembled Monolayer of Nanosized Particles Differing by Their Sizes.* The Journal of Physical Chemistry, 1995. **99**(44): p. 16425-16429.
29. Adachi, E., A.S. Dimitrov, and K. Nagayama, *Stripe Patterns Formed on a Glass Surface during Droplet Evaporation.* Langmuir, 1995. **11**(4): p. 1057-1060.
30. Gonuguntla, M. and A. Sharma, *Polymer Patterns in Evaporating Droplets on Dissolving Substrates.* Langmuir, 2004. **20**(8): p. 3456-3463.
31. Park, J. and J. Moon, *Control of Colloidal Particle Deposit Patterns within Picoliter Droplets Ejected by Ink-Jet Printing.* Langmuir, 2006. **22**(8): p. 3506-3513.
32. Li, Q., et al., *Self-Organization of Carbon Nanotubes in Evaporating Droplets.* The Journal of Physical Chemistry B, 2006. **110**(28): p. 13926-13930.
33. Young, T., *An Essay on the Cohesion of Fluids*. 1805. p. 65-87.
34. Eick, J.D., R.J. Good, and A.W. Neumann, *Thermodynamics of contact angles. II. Rough solid surfaces.* Journal of Colloid and Interface Science, 1975. **53**(2): p. 235-238.
35. Joanny, J.F. and P.G. de Gennes, *A model for contact angle hysteresis.* The Journal of Chemical Physics, 1984. **81**(1): p. 552-562.
36. Shanahan, M.E.R., *Simple Theory of "Stick-Slip" Wetting Hysteresis.* Langmuir, 1995. **11**(3): p. 1041-1043.

37. Cassie, A.B.D. and S. Baxter, *Wettability of porous surfaces.* Transactions of the Faraday Society, 1944. **40**: p. 546-551.
38. Pak, B.C. and Y.I. Cho, *HYDRODYNAMIC AND HEAT TRANSFER STUDY OF DISPERSED FLUIDS WITH SUBMICRON METALLIC OXIDE PARTICLES.* Experimental Heat Transfer, 1998. **11**(2): p. 151 - 170.
39. Morse, H.W., *On Evaporation from the Surface of a Solid Sphere. Preliminary Note.* Proceedings of the American Academy of Arts and Sciences, 1910. **45**(14): p. 363-367.
40. Peiss, C.N., *Evaporation of small water drops maintained at constant volume.* Journal of Applied Physics, 1989. **65**(12): p. 5235-5237.
41. Birdi, K.S. and D.T. Vu, *Wettability and the evaporation rates of fluids from solid surfaces.* Journal of Adhesion Science and Technology, 1993. **7**: p. 485-493.
42. Rowan, S.M., M.I. Newton, and G. McHale, *Evaporation of Microdroplets and the Wetting of Solid Surfaces.* The Journal of Physical Chemistry, 1995. **99**(35): p. 13268-13271.
43. Rowan, S.M., et al., *Evaporation of Microdroplets of Three Alcohols.* The Journal of Physical Chemistry B, 1997. **101**(8): p. 1265-1267.
44. Chandra, S., et al., *Effect of liquid-solid contact angle on droplet evaporation.* Fire Safety Journal, 1996. **27**(2): p. 141-158.
45. Crafton, E.F. and W.Z. Black, *Heat transfer and evaporation rates of small liquid droplets on heated horizontal surfaces.* International Journal of Heat and Mass Transfer, 2004. **47**(6-7): p. 1187-1200.
46. Maxwell, J.C., *Electricity and Magnetism.* 1873.
47. Xie, H., et al., *Dependence of the thermal conductivity of nanoparticle-fluid mixture on the base fluid.* Journal of Materials Science Letters, 2002. **21**(19): p. 1469-1471.
48. Lee, S., et al., *Measuring Thermal Conductivity of Fluids Containing Oxide Nanoparticles.* Journal of Heat Transfer, 1999. **121**(2): p. 280-289.
49. Wang, X., X. Xu, and S.U.S. Choi, *Thermal conductivity of nanoparticle-fluid mixture.* J Thermophys Heat Transfer, 1999. **13**(4): p. 474-480.
50. Kumar Das, S., et al., *Temperature Dependence of Thermal Conductivity Enhancement for Nanofluids.* Journal of Heat Transfer, 2003. **125**(4): p. 567-574.
51. Li, X.F., et al., *Thermal conductivity enhancement dependent pH and chemical surfactant for Cu-H2O nanofluids.* Thermochimica Acta, 2008. **469**(1-2): p. 98-103.
52. Murshed, S.M.S., K.C. Leong, and C. Yang, *Investigations of thermal conductivity and viscosity of nanofluids.* International Journal of Thermal Sciences, 2008. **47**(5): p. 560-568.
53. Garg, J., et al., *Enhanced thermal conductivity and viscosity of copper nanoparticles in ethylene glycol nanofluid.* Journal of Applied Physics, 2008. **103**(7): p. 074301-6.
54. Lee, J.-H., et al., *Effective viscosities and thermal conductivities of aqueous nanofluids containing low volume concentrations of Al2O3 nanoparticles.* International Journal of Heat and Mass Transfer, 2008. **51**(11-12): p. 2651-2656.
55. Wensel, J., et al., *Enhanced thermal conductivity by aggregation in heat transfer nanofluids containing metal oxide nanoparticles and carbon nanotubes.* Applied Physics Letters, 2008. **92**(2): p. 023110-3.

56. Choi, S.U.S., et al., *Anomalous thermal conductivity enhancement in nanotube suspensions.* Applied Physics Letters, 2001. **79**(14): p. 2252-2254.
57. Hwang, Y.J., et al., *Investigation on characteristics of thermal conductivity enhancement of nanofluids.* Current Applied Physics, 2006. **6**(6): p. 1068-1071.
58. Keblinski, P., et al., *Mechanisms of heat flow in suspensions of nano-sized particles (nanofluids).* International Journal of Heat and Mass Transfer, 2002. **45**(4): p. 855-863.
59. Hamilton, R.L.C., O. K., *Thermal conductivity of heterogeneous two-component systems.* I & EC Fundamentals, 1962. **1**: p. 187-191.
60. Einstein, A., *Eine neue Bestimmung der Melkuldimensionen.* Annalen der Physik, 1906. **19**: p. 289-306.
61. Mooney, M., *The Viscosity of a Concentrated Suspension of Spherical Particles.* Journal Of Colloid Science, 1951. **6**: p. 162-170.
62. Simha, R., *A Treatment of the Viscosity of Concentrated Suspensions.* Journal of Applied Physics, 1952. **23**(1020-1024).
63. Frankel, N.A., and Acrivos, A., *On the Viscosity of Concentrated Suspension of Solid Spheres.* Chemical Engineering Science, 1967. **22**: p. 847-853.
64. Eshelby, J.D., *The Determination of the Elastic Field of an Ellipsoidal inclusion, and Related Problems.* Proceedings of Royal Society of London, 1957. **A241**: p. 376-396.
65. Liu, S., and Masliyah, J. H. , *Rheology of Suspensions. In Suspensions: Fundamentals and Applications in the Petroleum Industry, edited by Schramm, L . L.* American Chemical Society Advances In Chemistry Series, 1996. **251**: p. 107-176.
66. Das, S.K., et al., *Temperature Dependence of Thermal Conductivity Enhancement for Nanofluids.* Journal of Heat Transfer, 2003. **125**(4): p. 567.
67. Putra, N., W. Roetzel, and S. Das, *Natural convection of nano-fluids.* Heat and Mass Transfer, 2003. **39**(8): p. 775.
68. Mare, T.S., A. G., Nguyen, C. T., Miriel, J., Roy, G., *Experimental heat transfer and viscosity study of nanofluids: water-Al_2O_3.* Proc. 2nd Int. Conf. Thermal Eng. Theory and Applications,, 2006(Paper No. 93).
69. Nguyen, C.T., et al., *Viscosity data for Al2O3-water nanofluid--hysteresis: is heat transfer enhancement using nanofluids reliable?* International Journal of Thermal Sciences, 2008. **47**(2): p. 103.
70. Wasan, D.T. and A.D. Nikolov, *Spreading of nanofluids on solids.* Nature, 2003. **423**(6936): p. 156.
71. Darsh Wasan, A.N.D.H., *New vistas in dispersion science and engineering.* AIChE Journal, 2003. **49**(3): p. 550-556.
72. Wasan, D., A. Nikolov, and B. Moudgil, *Colloidal dispersions: Structure, stability and geometric confinement.* Powder Technology, 2005. **153**(3): p. 135.
73. Trokhymchuk, A., et al., *A Simple Calculation of Structural and Depletion Forces for Fluids/Suspensions Confined in a Film.* Langmuir, 2001. **17**(16): p. 4940-4947.
74. Chengara, A., et al., *Spreading of nanofluids driven by the structural disjoining pressure gradient.* Journal of Colloid and Interface Science, 2004. **280**(1): p. 192-201.

75. Vafaei, S., Borca-Tasciuc, T., Podowski, M.Z., Purkayastha, A., *Effect of Nanoparticles On Sessile Droplet Contact Angle.* Nanotechnology, 2006. **17**: p. 2523-2527.
76. MacGillivray, J., Sefiane, K., *Investigation of the Viscous Dissipation Near Ther Three-Phase Contact Line Of Wetting Nanofluids.* Edinburgh Uiversity Masters Project, 2007.
77. Maenosono, S., et al., *Growth of a Semiconductor Nanoparticle Ring during the Drying of a Suspension Droplet.* Langmuir, 1999. **15**(4): p. 957-965.
78. Sommer, A.P., M. Ben-Moshe, and S. Magdassi, *Size-Discriminative Self-Assembly of Nanospheres in Evaporating Drops.* J. Phys. Chem. B, 2004. **108**(1): p. 8-10.
79. Prevo, B.G., J.C. Fuller, and O.D. Velev, *Rapid Deposition of Gold Nanoparticle Films with Controlled Thickness and Structure by Convective Assembly.* Chem. Mater., 2005. **17**(1): p. 28-35.
80. Huang, J., Franklin, K., Tao, A.R., Connor, S., Yang, P., *Spontaneous formation of nanoparticle stripe patterns through dewetting.* Nature Materials, 2005. **4**(12): p. 896-900.
81. Chon, C.H., et al., *Effect of Nanoparticle Sizes and Number Densities on the Evaporation and Dryout Characteristics for Strongly Pinned Nanofluid Droplets.* Langmuir, 2006. **23**(6): p. 2953-2960.
82. Bigioni, T.P., Lin, X., Bguyen, T. T., Corwin, E.I., Witten, T.A., Jaeger, H.M., *Kinetically driven self assembly of highly ordered nanoparticle monolayers.* Nature Materials, 2006. **5**(April): p. 265-270.
83. Gordon, M.J. and D. Peyrade, *Separation of colloidal nanoparticles using capillary immersion forces.* Applied Physics Letters, 2006. **89**(5): p. 053112.
84. Smith, M.K. and S.H. Davis, *Instabilities of dynamic thermocapillary liquid layers. Part 1. Convective instabilities*. 1983, Cambridge Journals Online. p. 119-144.
85. Girard, F., et al., *Evaporation and Marangoni Driven Convection in Small Heated Water Droplets.* Langmuir, 2006. **22**(26): p. 11085-11091.
86. Garnier, N. and C. Normand, *Effects of curvature on hydrothermal waves instability of radial thermocapillary flows.* Comptes Rendus de l'Académie des Sciences - Series IV - Physics, 2001. **2**(8): p. 1227-1233.
87. Garnier, N. and A. Chiffaudel, *Two dimensional hydrothermal waves in an extended cylindrical vessel.* The European Physical Journal B - Condensed Matter and Complex Systems, 2001. **19**(1): p. 87-95.
88. Popov, Y.O., *Evaporative deposition patterns: Spatial dimensions of the deposit.* Physical Review E, 2005. **71**(3): p. 036313.
89. Masoud, H. and J.D. Felske, *Analytical solution for Stokes flow inside an evaporating sessile drop: Spherical and cylindrical cap shapes.* Physics of Fluids, 2009. **21**(4): p. 042102-11.
90. Chandrasekhar, S., *Hydrodynamic and hydromagnetic stability*. Related Information: International Series of Monographs on Physics. 1961. Medium: X; Size: Pages: 672.
91. Bostwick, J.B. and P.H. Steen, *Capillary oscillations of a constrained liquid drop.* Physics of Fluids, 2009. **21**(3): p. 032108-10.
92. Cristini, V. and J. Lowengrub, *Three-dimensional crystal growth--I: linear analysis and self-similar evolution.* Journal of Crystal Growth, 2002. **240**(1-2): p. 267-276.

93. Ha, V.-M. and C.-L. Lai, *Onset of Marangoni instability of a two-component evaporating droplet.* International Journal of Heat and Mass Transfer, 2002. **45**(26): p. 5143-5158.
94. Zhang, N., *Surface tension-driven convection flow in evaporating liquid layers.* Surface tension driven flows and applications,, 2006. **Vol. 37/661**: p. 147.
95. Steinchen, A. and K. Sefiane, *Self-organised marangoni motion at evaporating drops or in capillary menisci â€“ thermohydrodynamical model.* Journal of Non-Equilibrium Thermodynamics, 2005. **30**(1): p. 39-51.
96. Barash, L.Y., et al., *Evaporation and fluid dynamics of a sessile drop of capillary size.* Physical Review E, 2009. **79**(4): p. 046301.
97. Blinova, I., V. Gusarov, and I. Popov, *"Almost quasistationary" approximation for the problem of solidification front stability.* Zeitschrift für Angewandte Mathematik und Physik (ZAMP), 2009. **60**(1): p. 178-188.
98. Sefiane, K. and R. Bennacer, *Nanofluids droplets evaporation kinetics and wetting dynamics on rough heated substrates.* Advances in Colloid and Interface Science. **147-148**: p. 263-271.
99. Nguyen, C.T., et al., *Temperature and particle-size dependent viscosity data for water-based nanofluids - Hysteresis phenomenon.* International Journal of Heat and Fluid Flow, 2007. **28**(6): p. 1492-1506.
100. Wang, B., L. Zhou, and X. Peng, *Viscosity, thermal diffusivity and Prandtl number of nanoparticle suspensions*. 2004, Taylor & Francis. p. 922 - 926.
101. Chen, H., et al., *Rheological behaviour of ethylene glycol based titania nanofluids.* Chemical Physics Letters, 2007. **444**(4-6): p. 333-337.
102. Namburu, P.K., et al., *Numerical study of turbulent flow and heat transfer characteristics of nanofluids considering variable properties.* International Journal of Thermal Sciences, 2009. **48**(2): p. 290-302.
103. Abramchuk, S.S. and et al., *Direct observation of DNA molecules in a convection flow of a drying droplet.* EPL (Europhysics Letters), 2001. **55**(2): p. 294.
104. Chung, S.K. and E.H. Trinh, *Containerless protein crystal growth in rotating levitated drops.* Journal of Crystal Growth, 1998. **194**(3-4): p. 384-397.
105. Bhardwaj, R., X, Fang., D, Attinger., *Pattern formation during the evaporation of a colloidal nanoliter drop: a numerical and experimental study.* New Journal of Physics, 2009. **11**: p. 1-34.
106. Truskett, V.N. and K.J. Stebe, *Influence of Surfactants on an Evaporating Drop: Fluorescence Images and Particle Deposition Patterns.* Langmuir, 2003. **19**(20): p. 8271-8279.